Understanding liquid movements in textiles for the development of liquid repellent strategies

Gannian Zhang

Submitted in partial fulfilment of the requirements of the Degree of Doctor of Philosophy

School of Engineering and Materials Science

Queen Mary University of London

London E1 4NS

Statement of originality

I, Gannian Zhang, confirm that the research included within this thesis is my own work or that where it has been carried out in collaboration with, or supported by others, that this is duly acknowledged below and my contribution indicated. Previously published material is also acknowledged below.

I attest that I have exercised reasonable care to ensure that the work is original, and does not to the best of my knowledge break any UK law, infringe any third party's copyright or other Intellectual Property Right, or contain any confidential material.

I accept that the College has the right to use plagiarism detection software to check the electronic version of the thesis.

I confirm that this thesis has not been previously submitted for the award of a degree by this or any other university.

Signature: Gannian Zhang

Date: 20th May, 2018

Details of collaboration and publications:

Publications:

1. Gannian Zhang, Rachna Parwani, Corinne A. Stone, Asa H. Barber*, Lorenzo Botto, 2017. X-ray imaging of transplanar liquid transport mechanisms in single layer textiles. *Langmuir*, *33*(43), pp.12072-12079.
2. Gannian Zhang, Miguel A. Quetzeri-Santiago, Corinne A. Stone, Lorenzo Botto, J. Rafael Castrejón-Pita*, 2018. Droplet impact dynamics on textiles. *Submitted to Soft Matter*

Collaborations:

1. Collaborating with Defence Science and Technology Laboratory (Dstl) of the U.K. on understanding the oil permeation phenomenon observed in their oleophobic textiles.
2. Collaborating with the University of Portsmouth on X-ray imaging of oil spreading through the thickness of a bare cotton textile.
3. Collaborating with Dr. J. Rafael Castrejón-Pita's research team on understanding droplets impact dynamics on textiles via high-speed shadowgraphy.

The above listed collaborations resulted in the three experimental chapters of this thesis.

Abstract

The understanding of the liquid movements in textiles is important to the development of novel liquid repellent strategies based on the manipulation of liquid motion. In this thesis we focus on the two areas that have received little attention: (1) the liquid permeation across the thickness of a single-layer textile following the deposition of a static droplet and (2) the liquid movements following the impact of droplets on a single-layer textile.

In the study of area (1) we report a time-resolved high resolution X-ray imaging of the motion of the liquid-vapour interface in the textile thickness direction. The imaging of the time-dependent position of the interface is made possible by the use of ultra-high viscosity liquids (dynamic viscosity $2.5 \cdot 10^6$ times higher than that of water). Imaging results suggested a three-stage permeation mechanism with each stage being associated with one type of capillary channels in the textile geometry. We also showed that the permeation dynamics cannot be described by the popular Washburn theory.

In the study of area (2) we record the impact of droplets on textiles with high-speed imaging. We showed that the impact on textiles at short timescales involved no droplet shape deformation if the textile's porosity was sufficiently high. We also showed that droplets could be captured by the textiles under some impact conditions. By balancing the dynamic and capillary pressures we showed that the droplet penetration was governed by a threshold pore size and the droplet diameter. Moreover, we identified 5 stages for the liquid spreading on the textile surfaces following the impact. Within the investigated range of impact velocity the surface chemistry of the textiles was unimportant in the determination of liquid repellency.

We also investigated the transplanar liquid permeation across non-wettable textiles following the deposition of droplets. We showed that the permeation was governed by a critical pore size and the weight of the deposited liquid. We discussed the limitation of the Gillespie scaling, developed for the prediction of in-plane spreading area in papers, in the description of the in-plane capillary spreading dynamics in textiles.

Table of Contents

List of figures

1 Thesis introduction

The understanding of the liquid movements in a textile is important to many applications, from the design of liquid-repellent textiles for the protection of skin[1-2] to the development of resin impregnation methodologies[3-4] and the manufacturing of textiles with improved wearability[5]. Classic problems are the prediction of the in-plane spreading area following the deposition of a static droplet[6-7] and the analysis of the liquid wicking rate[8] in the thickness direction of a textile. In this thesis we focus on the following two areas: (1) the liquid spreading from a static droplet in the thickness direction of a textile (termed 'transplanar spreading' or 'transplanar transport') and (2) the liquid movements associated with the impact of a droplet on a textile.

In previous studies[6, 9] the transplanar spreading in a fibrous material has been identified as the first liquid movement following the droplet deposition. Experiments on the transplanar spreading in single layer textiles have so far been limited to the approximate estimation of the liquid absorption rate with the 'demand wettability' method[10]. Moreover, the development of theoretical models has been hindered by the significant uncertainty of the initiation of the transplanar spreading in porous layers. A model by Patnaik et al.[9] assumes that the transplanar spreading in a single-layer textile occurs uniformly under the droplet and the advancing liquid front is planar. Whereas a model by Starov et al.[11] assumes that the advancing liquid front is hemispherical. Moreover, a model by Marmur[12] developed for general thin porous media assumes that the transplanar spreading occurs at the centre of the droplet-medium contact area under the droplet. The lack of experimental data to aid the development of theoretical models has become a major motivation of this research.

The understanding of the impact of a droplet on a textile is important not only to the manufacturing of the liquid repellent textiles, but also to the prediction of stain sizes of impacting blood droplets in forensics science[13]. The impact typically results in the liquid movement on the textile surface ('lateral spreading') and sometimes the liquid penetration through the textile pores ('impact penetration')[14]. The research of the impact dynamics has been limited to the prediction of the critical droplet velocity for the impact penetration[14] and

the estimation of the impact stress[15]. The dynamics regarding the lateral spreading has not yet been investigated. In addition, for a droplet impact at a velocity of the order of 1 m/s the early-stage impact penetration is typically considered to be driven by a so-called 'water hammer pressure'[15] resulted from the assumed temporary liquid compression at the droplet bottom[16-18]. However, the liquid compression has only been experimentally confirmed[19] for the droplet impact on impenetrable solids at a velocity of the order of 10^3 m/s. Scarce experimental data support the direct translation of the 'water hammer' assumption to the droplet impact at a velocity of 1 m/s. Consequently, we are motivated to provide a better understanding on the droplet impact dynamics in this thesis.

The primary goal of this thesis is therefore, the characterisation of (1) the transplanar liquid spreading and (2) the droplet impact dynamics with adequate experimental approaches. For the transplanar spreading in a single layer textile, direct imaging is challenging due to the small timescale of the movement of a low viscosity liquid droplet over the textile thickness of the order of 100 µm. The characterisation of the transplanar spreading has been attempted with delicate instruments[20-21] but a relatively coarse spatial resolution of the order of 100 µm has been achieved without the sacrifice of the temporal resolution. Visualisation of the transplanar liquid movement at such a spatial resolution is impossible. To overcome the addressed issues (in chapter 4) we report a time-resolved X-ray visualisation of the transplanar liquid transport in a single-layer textile at a resolution of the order ~1 µm using ultra-high viscosity silicone fluids having a dynamic viscosity up to 2.5 million times that of water. Our approach enables direct imaging of the transplanar transport due to the slow penetration kinetics of the fluids. We aim to find out the capillary channels in the textile that are responsible for the transplanar liquid transport, discuss the transport dynamics and propose strategies for the manipulation of the transplanar liquid movements.

For the study of the droplet impact dynamics on a textile, especially the early stage impact dynamics associated with the droplet penetration, in chapter 5 we record the impact at a frame rate of $6.4 \cdot 10^4$ fps via high-speed imaging. By analysing the images we aim to develop a model that describes

the universal early stage penetration phenomenon for all porous media. Also we aim to provide experimental data on the ‘lateral spreading’ following the droplet impact for the development of models that describe the liquid movements on the textile surface. Moreover, by analysing the pressures during the droplet impact we develop a model for the prediction of the critical pore size of impact penetration, in the hope to provide guidance for the manufacturing of modern raincoats and umbrellas that resist impacting droplets.

The secondary goal of the thesis is the study of the ‘transplanar static oil droplet permeation’ in an oleophobic textile typically having an apparent contact angle greater than 90°. The permeation contradicts the predicted non-wetting by classical wetting theories. We aim to develop a model for the prediction of such oil permeation in any given oleophobic textiles.

In chapter 6 we provide a summary of the major conclusions from chapter 3, 4 and 5 and propose some interesting research avenues for a more complete understanding on the contact of a droplet and a textile.

2 Review of literature

2.1 Capillary liquid spreading in textiles

Capillary liquid spreading occurs commonly in textiles. Some frequently seen examples of this type of spreading are the sinking of coffee or wine droplets into clothes followed by the formation of visible liquid stains and the absorption of sweat droplets by sportswear during exercises. Precisely, capillary liquid spreading refers to the liquid movements in the capillary channels formed by microscopic textile fibres driven by the surface tension of the liquid. This type of spreading is also called 'capillary sorption' in previous papers[7, 22]. Understanding the spreading dynamics is important to the design of liquid-repellent textiles[1, 23], the improvement of textiles' wearability[24-25] and the development of techniques for resin impregnation[3-4]. Capillary liquid spreading occurs in two stages[6, 12]. Stage 1 is called 'transplanar spreading'[26] referring to the liquid spreading through a textile in the direction of the textile thickness and vertically saturating the textile[6]. Stage 2 is called 'in-plane spreading' referring to the liquid movement in the plane of the textile. Stage 1 may coincide with some in-plane spreading[12]. Both stages have been studied in the literature.

Previous papers have studied the capillary liquid spreading in textiles focusing on the three typically spreading situations illustrated in figure 2-1. Figure 2-1(a) shows the liquid rising in the plane of a textile as a result of the vertical textile dipping in an unlimited liquid reservoir. Figure 2-1(b) shows gradual absorption of a sessile liquid droplet into the interior of a textile. Figure 2-1(c) shows the transplanar liquid spreading in a textile from an unlimited liquid reservoir. Type (c) spreading in liquid-repellent textiles is typically assisted by an external pressure, as indicated by the red arrows. The three spreading situations cover most of the textile-liquid contact in practical capillary liquid spreading cases.

2.1.1 Dynamics of capillary spreading

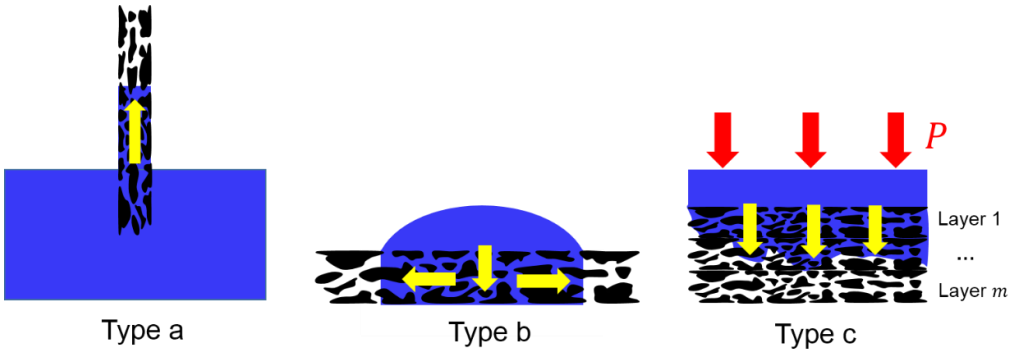

Figure 2-1. Schematics showing the three types of capillary liquid spreading reported in the literature. Type a: 'in-plane' liquid rising in a single-layer textile vertically dipped into an unlimited liquid reservoir. Type b: spreading of a droplet in a single-layer textile. Type c: transplanar spreading driven by an external pressure gradient in a multi-layer textile. m denotes the number of textile layers. The yellow arrows indicate the capillary spreading directions.

Type a: in-plane liquid rising from an unlimited liquid reservoir

The spreading dynamics for type (a) is studied through the time evolution of the height y of the rising liquid front (averaged over the textile width) with respect to the liquid surface in the reservoir. If the largest pores of a textile are filled with gels, the liquid would only rise in the textile yarns and y would initially vary linearly with $t^{1/2}$ before the surface tension of the liquid is balanced by the weight of the absorbed liquid in the textile[8]. In contrast, if the largest pores are empty, the liquid would spread not only in the yarns but also gradually fill the largest pores. The spreading dynamics in this case is determined by the sizes and the depths of the pores and the friction that the liquid encounters while passing through the channels that connect the pores[8]. Consequently, y does not conform to $y{\sim}t^{1/2}$.

For type (a) the $y{\sim}t^{1/2}$ scaling also describes the liquid rising in other single-layer porous media than textiles accurately if such large voids as the largest textile pores are absent. For example, $y{\sim}t^{1/2}$ describes the rising of potassium chloride and sodium eosine solutions in blotting papers and thin

layers of Penn loam soil, respectively[27]. Subsequently $y \sim t^{1/2}$ has been cross-checked for general fibrous assemblies by Peek et al[28], then has been proven valid by the dipping of napkins into coffee and towels into black ink[29] and recently proven correct by the more refined measurements of the rising of several organic liquids in paper strips[30]. Based on so much experimental data reported in the literature, for type (a) the $y \sim t^{1/2}$ scaling can be considered true for general porous media regardless of the liquid type or the microscopic architecture of a porous medium.

The empirical scaling $y \sim t^{1/2}$ received theoretical support from Gillespie's theory on the liquid rising in general porous media dipped into unlimited reservoirs[30]. In brief, combining Darcy's law with the equation of continuity from Ref.[31] Gillespie deduced $y^2 \sim \frac{\sigma k_0}{r \mu C_0} t$, where r is the averaged pore size of the porous medium under consideration, μ is the liquid dynamic viscosity, σ is the liquid surface tension, k_0 is the permeability of the porous medium when all the pores of the medium are carrying the liquid and C_0 is the liquid concentration in the porous medium corresponding to k_0. The scaling $y^2 \sim \frac{\sigma k_0}{r \mu C_0} t$ was supported by the experimental data from dipping paper strips into unlimited reservoirs containing organic fluids[30].

The Gillespie scaling $y^2 \sim \frac{\sigma k_0}{r \mu C_0} t$ should not be regarded as the Washburn equation from Ref. [32], although both the Gillespie scaling and the Washburn equation indicate that y varies linearly with $t^{1/2}$. The Gillespie scaling is derived through the application of Darcy's law onto a porous medium having a non-uniform flow rate[30]. The non-uniform flow rate is due to the pore size scale separation in the porous medium, typically resulting in a wetted region saturated by the liquid and another unsaturated wetted region extending ahead of the saturated one. This contrasts with the uniform flow rate assumed in the Washburn theory.

Type b: Capillary liquid spreading of a sessile droplet

Type b refers to the capillary liquid spreading of a limited liquid quantity in a single-layer textile focusing on both in-plane and transplanar spreading. In the

case of transplanar spreading, researchers have found that the absorbed liquid volume V by a single-layer textile varies linearly with $t^{1/2}$ [33-34] through the deposition of droplets having sizes from 5 μl to 40 μl. Interestingly, only for polyvinyl alcohol (PVA) V varies linearly with t [34]. Until now no explanation has been made on this exception of PVA, emphasising the complexity of the spreading dynamics. For the in-plane liquid spreading in a variety of single-layer textiles, experimental data have shown that the area A of the wetted region varies linearly with $t^{1/3}$ [7]. However the scaling $A \sim t^{1/3}$ does not hold if the liquid diffuses into the textile fibres[8]. The liquid diffusion causes the fibres to swell so that the inter-fibre distance is significantly changed, slowing the progression of the in-plane spreading. Moreover, the in-plane spreading could also be slowed by the sudden significant increase of the radius of the capillary path[35]. Also 'corners' of a capillary path or high curvature points on the wall of a capillary path would slow the in-plane spreading via liquid pinning or other complex interactions[35].

The scaling $V \sim t^{1/2}$ for the type b spreading has not yet received strong theoretical support. A relevant study[36] on liquid penetration in a single capillary tube with a uniform cross section shows that $V \sim t^{1/2}$ is correct only when the capillary tube surface wettability $\theta_Y \leq 60°$, θ_Y is the Young's contact angle. The conclusions from Ref. [36] could only be translated to a single-layer textile if the transplanar capillary path of that textile has an insignificant perturbation of the cross sectional radius R_c and the droplet size V_0 is significantly greater than the capillary path size, that is $\frac{V_0}{\pi {R_c}^3} \gg 1$. No research so far has reported the transplanar spreading dynamics for $\frac{V_0}{\pi {R_c}^3} \sim 1$.

The scaling $A \sim t^{1/3}$ as reported in Ref.7 for the in-plane spreading in a textile can be derived from the Gillespie theory[6]. We will come to the derivation in section 2.1.3.

Type c: transplanar liquid spreading from unlimited reservoirs

Type c refers to the liquid spreading in the thickness direction of the textile following the deposition of a textile (single or multi-layered) horizontally under

(or above) an unlimited liquid reservoir. *Type c* is termed 'transplanar liquid uptake' in Ref. 10 and 'transplanar wicking' in Ref. 24 and [37]. If the textile shows good repellency to the liquid, the transplanar spreading would be assisted by an applied pressure on the material[10, 20, 35] in the direction indicated by the red arrows in figure 2-1.

In the case of single-layer textiles, previous studies has mainly focused on the time evolution of the penetrated liquid mass M. By recording the weight loss of the liquid source with a microbalance, scientists have found that M varies linearly with t before reaching a constant value[10, 24, 37]. So far the $M \sim t$ scaling is well agreed on in the literature.

In the case of multi-layer textiles, previous research have mainly analysed the liquid content in each textile layer as a function of time. Using Nuclear Magnetic Resonance (NMR), Bencsik et al.[20] could show the oil concentration for each textile layer as a function of time. However, no effort on interpreting the transplanar penetration rate was made. The main problem of Ref. 20 is the inconsistency of the estimated oil concentration for a given textile layer at a chosen time. The inconsistency implied low sensitivity of NMR to the oil used in their experiments, making the measurements of the oil volume fraction unreliable. Birrfelder et al.[24] studied the transplanar spreading through a two-layer knitted textile using X-ray radiography and presented the liquid front position in the thickness of the textile. The research suggested two mechanisms of the transplanar spreading: for transplanar spreading from one surface of a layer to its opposite surface, the liquid is transported via intra-yarn interstices, whereas for transplanar spreading between adjacent layers, the liquid is transported via large inter-yarn pores. However, no modelling of the spreading process was attempted. Rossi et al.[38] studied water transplanar penetration in a three-layer textile and quantified the volume distribution for each layer at a large timescale. No attempt to investigate the transplanar spreading mechanisms was made. Similarly, Weder et al.[21] also quantified the water distribution in a four-layer woven textile but did not care about the spreading mechanisms. The inability to characterise the transplanar liquid spreading in just one layer of the multilayer textiles is due to the fact that the

spatial resolution achieved in Ref. 21 and [38] was 70 μm/pixel, being of the same order of the textile layer thickness.

2.1.2 Transplanar liquid spreading in single-layer textiles

The understanding of the transplanar liquid spreading in a single-layer textile is crucial to the development of liquid repelling strategies for the textile. Previous relevant studies, as summarised in *type b* of section 2.1.1, have merely focused on the liquid absorption rate of a single-layer textile. No attempt has been made to characterise the transplanar liquid front motion or to study the transplanar spreading dynamics.

In the past two models[11-12, 39] were proposed for the description of the liquid front motion in the thickness of a porous medium. Yet the models did not reach an agreement on the initiation of the transplanar liquid motion. More importantly, no data was obtained to support either of the models.

The Marmur model: Figure 2-2 illustrates a five-stage penetration mechanism proposed by Marmur[12] for the spreading of a sessile droplet in a porous medium. When the droplet contacts the medium surface, the droplet does not penetrate immediately into the medium but remains on the surface,

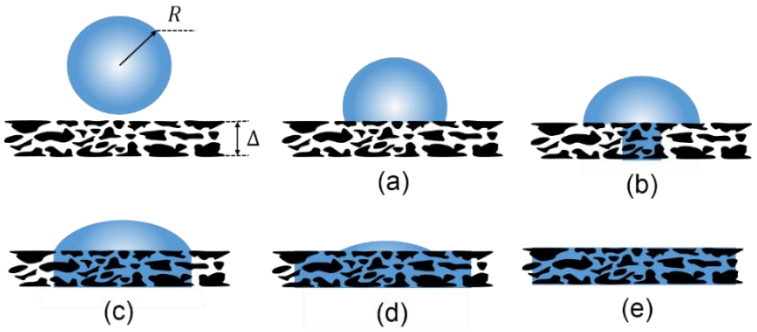

Figure 2-2. Mechanism of liquid penetration into a thin ($\Delta \ll R$) porous medium by Marmur[12]. (a). Droplet temporarily sits on the surface of the porous medium. (b). Liquid vertically penetrates the medium from the centre of the contact area. (c). The penetrated volume radially expands in the medium as the drop continually being absorbed. (d). Triple line on the surface of the medium shrinks inwards as the penetration progresses. (e). Complete penetration.

as shown in *stage a*. *Stage b* shows that the transplanar liquid spreading initiates from the centre of the droplet-medium contact area and the liquid volume remaining on the medium surface laterally distorts. *Stage c*, *d* and *e* mainly describe the lateral droplet spreading that occurs in the plane of the porous medium. The transplanar spreading is completed before entering *stage c*. By analysing the surface free energy throughout the transplanar spreading, Marmur[12] found that due to the small pore radii of the porous medium, only the driving force corresponding to the centre of the droplet-medium contact area was sufficient to trigger the transplanar spreading.

The Starov model: As illustrated in figure 2-3(b), Starov et al. [39] argued that the transplanar liquid spreading is initiated uniformly under the droplet and the advancing liquid front is planar. When the transplanar spreading is completed, the droplet would spread laterally in the plane of the porous medium as illustrated in figure 2-2(c) – (e). Moreover, Starov et al.[39] think that the transplanar spreading should complete immediately after the droplet is brought to the surface of the porous medium. For a porous medium whose thickness Δ is much smaller than the radius of a droplet R, the timescale t_Δ for the transplanar spreading of the droplet scales as $t_\Delta \sim \frac{\Delta^2 \mu}{k_p P_c}$ [39], where k_p is the permeability of the porous medium in the thickness direction and P_c is the capillary pressure. Starov et al.[39] have shown that $k_p P_c$ is of the order of 10^{-4} for a porous medium whose pore size is of the order of 10 μm. Therefore for the spreading of a droplet of a low viscosity liquid ($\mu < 10$ Pa·s) through a

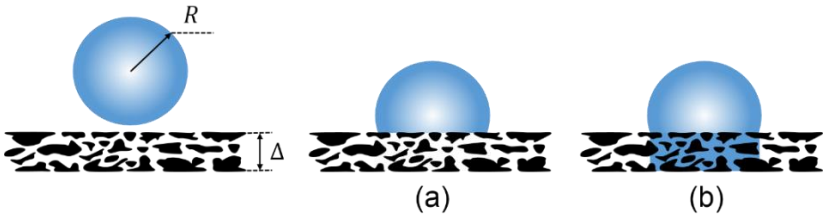

Figure 2-3. Same as figure 2-2 by Starov et al.[41] (a). Droplet is deposited on the surface of a porous medium at $t = 0$s. (b). Droplet immediately saturates the medium under the contact area at t_Δ (t_Δ of the order 10^{-4} s). The rest of the penetration stages are same as figure 2-2(c), (d) and (e).

porous medium whose thickness Δ is of the order of 100 μm, t_{Δ}~10^{-4} s. Therefore it is reasonable to assume 'immediate' transplanar spreading.

The Starov model for thick porous media: For a porous medium having $\Delta \gg R$, Starov et al.[11] think that the transplanar liquid spreading occurs uniformly under the droplet and the advancing liquid front is hemispherical, as illustrated in figure 2-4(a). Through their parametric study they found that the radius of the droplet base $L(t)$ and the radius of the wetted region in the

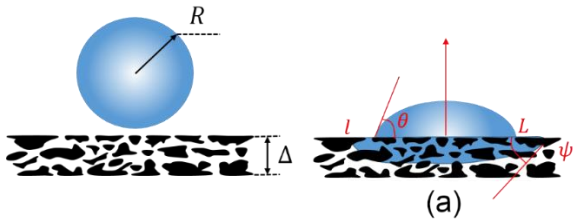

Figure 2-4. Mechanism of liquid penetration in thick ($\Delta \gg R$) porous media by Starov et al.[11] (a). The wetted region inside the porous medium as modelled by spherical cap. $L(t)$: radius of the drop base. $l(t)$: radius of the wetted circle of the wetted region inside the porous medium. $\theta(t)$: dynamic contact angle on the surface of the medium. $\psi(t)$: effective contact angle inside the porous medium.

porous medium $l(t)$ are both functions of the pore size and the porosity of the medium. Whereas $\theta(t)$ is only dependent on the surface wettability of the medium, and for all the experimental liquids, the time evolution of $\theta(t)$ was asymptotically the same.

Transplanar liquid spreading in other thin porous media than single-layer textiles

Experimental data on the transplanar liquid spreading in a single-layer textile are unavailable from the literature. Some data are available for other thin porous media than textiles. Bayramli and Powell[40] studied the dynamics of liquid gradually wicking normal to the axis of a bundle of regularly spaced parallel fibres. The bundle of fibres is geometrically similar to a textile yarn. The normal liquid wicking depth h was examined from the cross sectional view

of the bundle and was found to be $h \sim t^{1/2}$. Karppinen et al.[41] studied the dynamics of transplanar liquid spreading in paper by measuring the light reflection from the surface opposite to the one that the liquid droplet is placed on. Their results showed a monotonically decreasing light reflection curve as a function of time. The curves are asymptotically similar for all the liquids examined. Importantly, the curves showed no change of light intensity for in the first 0.05 s, meaning that transplanar spreading did not occur immediately. However neither did they explain this phenomenon nor did they provide a microscopic visualisation on how the liquid spread through the paper. Hyväluoma et al.[42] did a simulation on transplanar liquid spreading through a single-layer paper having a thickness much greater than the droplet radius. They found that if the paper is continually supplied with liquid from an unlimited reservoir, the transplanar liquid spreading depth h will conform to $h \sim t^{1/2}$. Whereas for a drop spreading through the paper, they found h will be much slower than $t^{1/2}$ but did not attempt to identify the new scaling.

Fundamental difference between a textile and a general porous medium

Table 2-1. Capillary pores of papers and textiles and their typical sizes

		Pore radius (μm)	Thickness (μm)
Paper	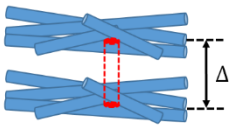	≤0.5	100
Textile	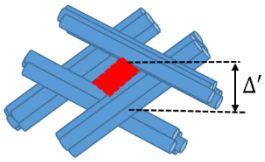	100	300

We must translate the experimental data of transplanar spreading in other thin porous media to single-layer textiles, with a good understanding on how different those media are from the textiles. The carbon fibre bundles in Ref. [43] are geometrically similar to the textile yarns containing straight fibres. Because if the fibres are helical, the fibres would entangle with one another forming complex internal yarn architectures. In this case, the yarns are no longer similar to the carbon fibre bundles in Ref. [43]. Moreover, some data of transplanar spreading are obtained from papers (Ref.[41] and [42]). A paper is

characterised by a separation of scales between the largest void in the porous structure and its thickness. While such separation of scale is not ensured in textiles. The issue of scale separation also relates to the distinction between single and multi-layer textiles. A thick multi-layer textile is considered a bulk, three-dimensional porous medium and the long-time capillary wicking behaviour for transplanar spreading in such a medium is expected to follow continuum theories. Whereas for single-layer textile, the time that liquid takes to spread through may be insufficient for asymptotic behaviours to be established.

2.1.3 Theories of capillary liquid spreading in thin porous media

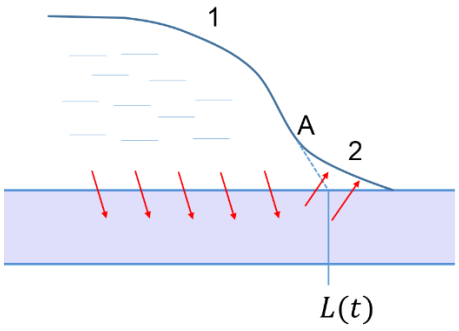

Figure 2-5. Schematic of theory by Starov et al.[46] on droplet spreading of a porous medium pre-saturated by the same liquid. Point A separates the inner region 2 and outer region 1. The red arrows indicate the liquid motions in region 1 and 2. $L(t)$ is the "macroscopic droplet base" length and is defined in the figure.

The Starov theory: this theory describes the time evolution of the radius $L(t)$ of the droplet-medium contact area, while the medium is saturated by the same liquid[44]. When the droplet is gently placed on the porous medium, the development of $L(t)$ will be driven by the liquid-solid interfacial tension and the mechanism of the development will involve two types of liquid movements: in the outer region 1, the liquid moves from the droplet to the saturated medium; whereas in the inner region 2, the liquid moves from the medium to the droplet. Starov et al.[44] have shown that $L(t)$ conforms to $L(t) = R(1 + \frac{t}{\tau_{cap}})^{0.1}$, where τ_{cap} is the timescale of the capillary spreading process and $\tau_{cap} \sim R^{10}$, and R is

the droplet radius. For sufficiently small droplets, $L(t)$ conforms to an approximate scaling of $L(t) \sim t^{0.1}$.

When the droplet is placed on the medium by a pipette, the development of $L(t)$ will initially be driven by inertia[44]. Because the droplet will inevitably travel at a velocity to the medium when dispensed by the pipette. Joanny[45] has found that for the initial inertia-driven spreading, $L(t)_{inertia} = (\frac{2\sigma}{\rho R})^{1/2} t$, where ρ is the liquid density at room temperature.

The Washburn theory: The Washburn theory has been initially developed for the characterisation of the dynamics of the liquid rising in a capillary tube, and has later been used for the estimation of water and oil movements in soil, for the prediction of the liquid impregnation in wood, and for the determination of the porosity and density of a porous medium[32]. Assuming steady flow passing through a regular cylindrical shaped tube with radius R_c, neglecting the slipping coefficient of the tube wall, we have the surface tension that drives the liquid to proceed:

$$F_{cap} = 2\pi R_c \sigma \cos\theta_Y \tag{2.1}$$

Where θ_Y is the Young's contact angle. The retarding force that cripples the capillary action comes from the viscosity of the liquid,

$$F_{Ret} = P\pi {R_c}^2 \tag{2.2}$$

Where P, the pressure gradient, can be obtained through Poiseuille's law $\frac{dV}{dt} = P\frac{\pi {R_c}^4}{8\mu x}$,

$$P = \frac{8\mu x}{\pi {R_c}^4}\frac{dV}{dt} = \frac{8\mu x}{\pi {R_c}^4}\left(\pi {R_c}^2 \frac{dx}{dt}\right) \tag{2.3}$$

Where $\frac{dV}{dt}$ is the rate of flow, μ is the dynamic liquid viscosity, x is the liquid front displacement. So the retarding force becomes:

$$F_{Ret} = 8\eta x\pi \frac{dx}{dt} \tag{2.4}$$

The mass of the liquid in the tube is $\pi {R_c}^2 x\rho$. Using Newton's second law of motion:

$$\pi {R_c}^2 x\rho \frac{d^2x}{dt^2} = 2\pi R_c \sigma \cos\theta_Y - 8\mu x\pi \frac{dx}{dt} \tag{2.5}$$

Washburn[32] and Rideal[46] have solved the equation:

$$t = \frac{2\mu}{\sigma R_c \cos\theta_Y} x^2 - \frac{\rho {R_c}^2}{8\mu} \log x + \frac{\rho^2 {R_c}^5}{512\mu^3 x^2} + \cdots \tag{2.6}$$

For sufficiently small R_c, we have the conventional form of the Washburn equation:

$$x^2 = \frac{\sigma R_c \cos\theta_Y}{2\mu} t \tag{2.7}$$

The Washburn equation has an important assumption: the liquid flow passing through the tube must have constant flow rate. Practically this assumption holds if an unlimited liquid reservoir continually supplies the porous medium with liquid, as illustrated in figure.2c of Ref. [47].

Equivalent capillary: an important application of the Washburn theory is the prediction of the total volume of liquid V_{total} that penetrates into a porous medium using $V_{total} = \pi \sum {R_c}^2 x$. However the determination of multiple R_c for the porous medium is problematic because of complex medium structure. Washburn clearly did not address this issue in Ref.[32]. Marmur[48] introduced the "equivalent capillary concept": the porous medium is modelled as an equivalent cylindrical capillary with a radius R_{eq}. The kinetics of liquid penetration in the equivalent capillary is assumed to be the same as that in the porous medium under consideration[48]. Assuming that the porous medium has porosity ε, cross sectional area A_{cross}, area of solid per unit volume S. For liquid penetrating through this porous medium, applying Darcy's law:

$$A_{cross} \frac{dx}{dt} = A_{cross} \frac{kP}{\mu x} \tag{2.8}$$

Where $P = \frac{F_{cap}}{A\varepsilon}$, where F_{cap} is the surface tension force that drives the liquid to proceed. $F_{cap} = S(1-\varepsilon)\sigma\cos\theta_Y$, k is the permeability of the medium. According to Kozeny-Carman equation[49],

$$k = \varsigma\frac{\varepsilon^3}{S^2(1-\varepsilon)^2} \tag{2.9}$$

Where ς is a constant dependent on the pore geometry of the medium, having a typical value 1/2; Hence,

$$x^2 = D't \tag{2.10}$$

Where $D' = \frac{2\varsigma\varepsilon\sigma\cos\theta_Y}{S(1-\epsilon)\mu}$. Comparing D' to $\frac{\sigma R_c\cos\theta_Y}{2\mu}$ of equation (2.7), we have the equivalent capillary radius:

$$R_{eq} = \frac{4\varsigma\varepsilon}{S(1-\varepsilon)} \tag{2.11}$$

In addition, Marmur[48] found that if the total weight of the liquid that penetrated into the porous medium is non-negligible, $R_{eq} \approx \frac{2(2\varsigma)^{1/3}\varepsilon}{S(1-\varepsilon)}$.

Radial capillary: Marmur[50] has developed the following equation for the in-plane droplet spreading dynamics:

$$y\left(\ln\frac{y}{y_0}\right)dy = \left(1-\frac{1}{2y\cos\theta}\right)d\tau_p \tag{2.12}$$

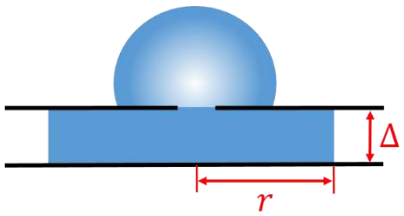

Figure 2-6. Schematic of the radial capillary model. The porous medium is represented by two parallel plates separating by a distance Δ. Liquid penetrates into the medium from the hole in the upper plate and radially wets the medium. The radius of the wetted area is r.

Where $y = \frac{r}{\Delta}$, $\tau_p = \frac{\sigma|\cos\theta_Y|}{6\mu\Delta}t$ and $y_0 = \frac{R}{\Delta}$, R is the radius of droplet. For thin porous media, $2y\cos\theta_Y$>>1, the solution to the equation is $y^2\left(\ln\frac{y}{y_0} - \frac{1}{2}\right) + \frac{{y_0}^2}{2} = 2\tau_p$, implying a weak $r^2 \sim t$ scaling. Experimental data[50] have shown that the scaling $r^2 \sim t$ is only for moderate θ_Y ($0 \leq \theta_Y \leq 60°$). Moreover, Ashari et al.[51] have shown that the scaling $r^2 \sim t$ describes the in-plane liquid spreading in fibrous media with randomly oriented fibres. For fibrous media having fibres aligned parallel to one another, the in-plane spreading would only occur in the anisotropic orientation of the fibres.

The Gillespie model: Gillespie has developed a model to describe the dynamics of in-plane liquid "creeping", after the transplanar spreading is completed. Assume the spreading is one-dimensional, when the "creeping" of liquid has reached the equilibrium state, the total volume in the porous medium is:

$$V_{total} = \omega h \int_0^{L_{max}} C\, dL \tag{2.13}$$

Where C is the liquid concentration measured in unit volume of the liquid per unit void volume of the porous medium; ω, h and L_{max} are the width, thickness of the medium, and the maximum in-plane spreading length respectively. By combining Muskat's equation of continuity[31] and Darcy's law, Gillespie has obtained:

$$\frac{\partial C}{\partial t} = M'\left(\frac{\partial k_1}{\partial L}\right) \tag{2.14}$$

Where M' is a constant depending on the properties of the porous medium and the liquid; k_1 is the permeability of the medium corresponding to the liquid concentration C. Wyckoff[52] has confirmed with experimental data that k_1 and C follow the relation:

$$\frac{k_1}{k_0} = \left(\frac{C}{C_0}\right)^3 \tag{2.15}$$

Where C_0 is the liquid concentration when every pore of the porous medium is filled with the liquid, and k_0 is the corresponding permeability of the medium. Solving the above three equations gives the Gillespie's scaling:

$$L\left(L^2 - {L_0}^2\right) = Nt \tag{2.16}$$

Where N is a constant depending on the properties of the liquid and the medium. The validity of this scaling is dependent on whether Darcy's law holds or not. Experimental data[53] have shown that the Gillespie scaling is only valid for Reynolds number<1.

The Kissa model: Re-writing Gillespie's scaling (two-dimensional form)[6]: $R^2\left[R^4 - {R_0}^4\right] = N't$ (N' is a constant), let A be the area of the wetted region in the porous medium, we have the following scaling:

$$A \sim (\frac{\sigma}{\mu})^{1/3} {V_{total}}^{2/3} t^{1/3} \tag{2.17}$$

Experimental data by Kissa[7] for the in-plane spreading of n-alkanes in varying fabrics, conformed closely to the $A \sim t^{1/3}$ scaling. In addition, Kissa[7] pointed out that the Gillespie theory holds only when the fibres of the fabrics are impermeable to the liquid. If swelling or any form of destruction to the fibres occurs in the spreading process, A will become unpredictable.

2.2 Impact driven liquid spreading

The impact of droplets on solid surfaces is common in nature, such as the commonly seen raindrop impact on tree leaves. The impact dynamics are crucial to industrial and domestic applications, such as the design of self-cleaning[54-55]surfaces, ice-repelling[56-57] surfaces, and the manufacturing of smart[58] and protective[1] clothing. The impact typically results in four characteristic phenomena: droplet spreading and receding[59], bouncing and splashing[60-62]. All the phenomena have been thoroughly investigated on smooth and rough solid surfaces. Recently the investigation has been extended onto complex micro-architectured surfaces, and symmetric drop splitting[63-64] and pancake bouncing[65] have been reported. However, little attention has been paid to the droplet impact on textiles. Previous studies have

only focused on the qualitative comparing of stain patterns of impacting blood droplets on textiles with different weaves[13], or the estimation of the impact stress based on the modified Joukowsky equation[15]. The impact dynamics on textiles have remained poorly understood from both the theoretical and the experimental side.

2.2.1 Initial contact of a droplet and a solid

Defining 'initial contact' (or 'collision'): Figure 2-7 illustrates 'initial collision' using the frequently seen two-dimensional schematic diagram[17, 66] for liquid impact analysis: an axisymmetric liquid droplet (diameter of D) moves at a constant velocity of U_i in the negative y direction and impacts a rigid, impermeable solid at $y = 0$, which is oriented normal to the impact velocity vector. Due to the slight compressibility of the droplet, a portion of the droplet would be compressed at the bottom (the blue region of figure 2-7) whereas the rest of the droplet would remain undisturbed. The compression generates a high pressure field[16]. The collision stage ends at $t = 3DU_i/4a^2$ [67] when the pressure is assuaged by lateral jetting[17, 68] at the triple line (point 'e' of figure 2-7), where a is the acoustic velocity. And the pressure rapidly drops to a stagnant pressure of incompressible fluid $(\frac{1}{2})\rho {U_i}^2$.

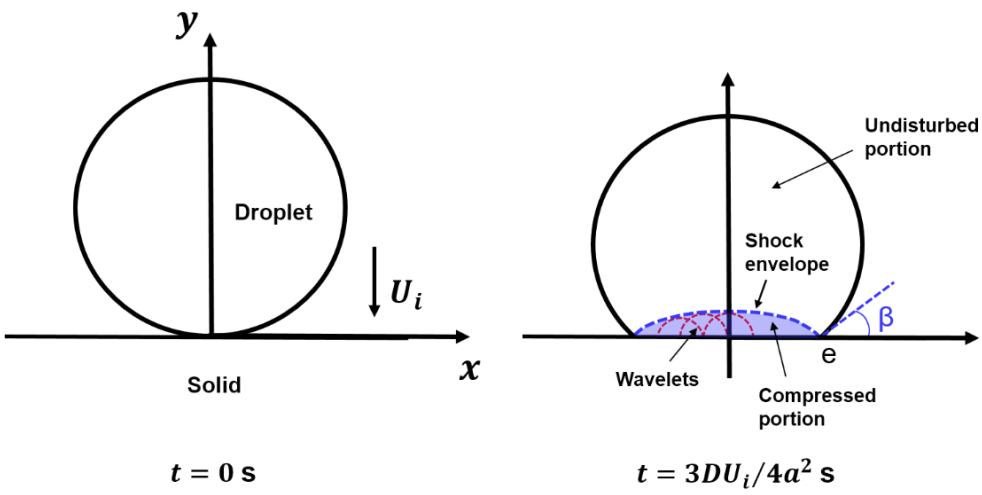

Figure 2-7. Initial contact of a droplet with an impermeable solid surface. The left and right image show the beginning and the end of collision respectively. The compression of liquid is shown as the blue region. $3DU_i/4a^2$ is the duration of collision.

Collision pressure: If the droplet is completely arrested by the solid, the pressure over the area of the compressed region[69], known as 'water-hammer' $\overline{P_{WH}}$, is generally estimated using the one-dimensional Joukowsky equation[15]:

$$\overline{P_{WH}} \approx \rho a U_i \tag{2.18}$$

Where ρ is the liquid density. The derivation of $\overline{P_{WH}}$ is based on simple momentum considerations and is explained thoroughly in Ref. [70]. In brief, for a liquid flow moving at U_i in a pipe, of which the cross sectional area is A, the interruption of the flow also results in the interruption of the sound waves propagating along with the flow. Using the momentum principle on the interruption of sound waves, we have: $\overline{P_{WH}} A t = \rho U_i t A a$, therefore $\overline{P_{WH}} \approx \rho a U_i$.

However, Heymann[19] has argued that for droplet collision, $\overline{P_{WH}} \approx \rho a U_i$ only vigorously estimates the uniform water-hammer before the contact angle β reaches a critical value $\beta_{critical}$. After $\beta_{critical}$, $\overline{P_{WH}}$ becomes a non-uniform pressure field with the pressure at the edge of the field rapidly increasing to the maximum value of $P_{max} \approx 3\rho a' U_i$ for $0.03 \leq \frac{U_i}{a'} \leq 0.3$ for water, where a' is the actual acoustic velocity in the droplet, and the pressure at the centre of the field being significantly smaller[19]. Because above $\beta_{critical}$, **(a)** a' is in fact: $a' = a_0(1 + k\frac{U_i}{a_0})$, where a_0 is the acoustic velocity in the droplet, k is the shock velocity coefficient (for water $k = 2.0$ and for sodium $k = 1.24$)[19]; **(b)** the impact area is no longer constant throughout the initial collision, but changes from a small initial dot-like area to a radially expanding plane. This research has not provided information on the pressure distribution within the triple line for $\beta > \beta_{max}$, though previous studies[16] have shown a non-uniform distribution.

Several historical papers[15, 71-72] have also attempted to analyse the water hammer. Savic and Boult[71] have neglected the compressibility of liquid and consequently predicted infinite impact pressure for the initial collision. Their discussion, therefore, is unhelpful in understanding the compressibility dominant initial collision. Engel[15] has found that the geometric characteristics of a liquid mass affects greatly the propagation of the acoustic shock wave generated by the compression of liquid. This has culminated the following equation:

$$P_{WH} = \frac{\alpha}{2}\rho a U_i \tag{2.19}$$

Where α is a geometric pre-factor for the liquid mass and theoretically $\alpha = 0.4$ for spherical droplet. A later experimental paper[72] has found $\alpha \approx 0.41$ for water and mercury droplets impacting solids. However, it must be pointed out that Engel's equation is not intended to represent the P_{max} for $\beta > \beta_{max}$[19], but for some reason it has been misused as P_{max} in studying droplet impacting porous media[73-74] (this will be discussed later), giving false impression on smaller P_{WH} for a round droplet than for a liquid column, whereas the opposite of which, as proven by Heymann[19], is really true. Moreover, Engel's arguments have assumed that the layer of the droplet volume that first encounters the solid surface will instantaneously form a thin cylindrical liquid layer at the bottom of the droplet, implying that the lateral liquid jetting from the impact region begins immediately. This assumption is not shared with most of the researchers studying the water-hammer[17, 19].

Acoustic limit: Combining the liquid compression with simple geometric arguments, Lesser[17] has stated that during the initial collision, the triple line (such as the contact point 'e' of figure 2-7) moves supersonically and laterally so that the expanding front of the shock wave generated by the impact remains within the droplet-solid contact area, and as a result, no lateral jetting could be seen. In brief, the triple line velocity could be estimated as $U_e = U_i/\tan\beta$. Indeed for $U_i \ll a$, the initial small β, the triple line moves at $U_e \geq a$, and this relationship is termed 'acoustic limit'[17].

Shock envelope: The shock envelope, as illustrated by a blue dash in figure 2-8, is a curved border separating the compressed and undisturbed liquid portion via Huyghens principle[17] in the initial collision. Theoretically it is really constructed as the envelope of individual wavelets (red dash curves) emitted by the expanding triple line (point 'e')[17]. For the following analysis, it is beneficial to assume that the droplet is static, whereas the solid surface moves in the positive y direction at δU_i. Assume at an infinitely small time Δt, the droplet first encounters with the solid surface. The position of e is $x(\Delta t)$ and

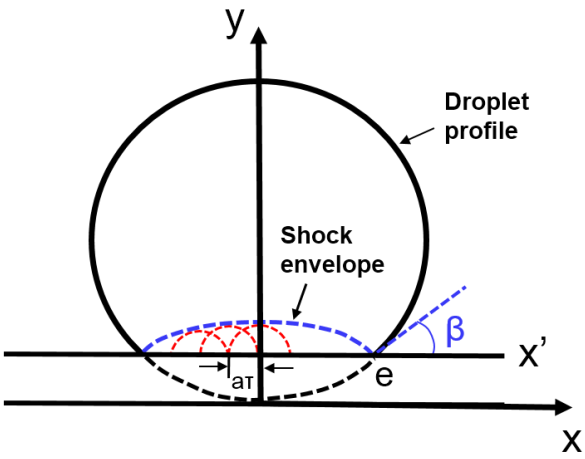

Figure 2-8. Schematic diagram for the comprehension of the 'shock envelope'

the centre of the wavelet is $(x(\Delta t), U_i\Delta t)$, thus the equation of the wavelets cross section in the xy plane at time t is:

$$[x - x(\Delta t)]^2 + (y - U_i\Delta t)^2 = [a(t - \Delta t)]^2 \tag{2.20}$$

From the above equation, Lesser[17] has obtained the coordinates of the expanding wavelets at time t:

$$x(t) = x(\Delta t) + [a(t - \Delta t)]^2 \tag{2.21}$$

$$y(t) = [a^2(t - \Delta t)^2 - [x - x(\Delta t)]^2]^{1/2} + U_i\Delta t \tag{2.22}$$

Previously only one experimental paper[68] has provided supporting data for the 'shock envelope' theory, using large droplets ($D = 11$ mm) of gelatine-water mixture to impact metals at $U_i = 150$ m/s (We is the Weber number $\sim 10^6$). With such a high U_i, the timescale for collision has been extended to $3DU_i/4a^2 \cong 1$ μs. This timescale has made the collision observable with the finest temporal resolution of high-speed imaging reported. Additionally, their images showed roughly 1 μs delay between the end of collision and the lateral jetting but no explanation on the delay was offered.

It must be mentioned that, all the discussion above focuses on U_i at least on the order of 10 m/s and D much greater than the capillary length. It is therefore reasonable to question whether the 'initial collision' theory is valid for relatively

small droplets (D~1 mm) striking a solid surface at U_i~1 m/s ($10 < We < 100$). In some recent papers, researchers have measured the force of an impacting droplet using a piezoelectric quartz sensor[75] and have estimated the impact pressure via simulations[16]. P_{max} is about $2\rho(U_i)^2$ (order of 1 kPa), much smaller than the water-hammer (order of 1MPa) proposed in the initial collision. A possible cause of this disagreement is the temporal resolution limit of experimental apparatus. For example, the timescale for the water-hammer to exist, in the case of the impact of tiny droplets, is of the order of 1 ns (having D~1 m/s, U_i~1 m/s and $a \approx 1{,}500$ m/s, $3DU_i/4a^2 \approx 1$ ns). Whereas a piezoelectric quartz sensor typically could only achieve a temporal resolution of 50 μs[75].

2.2.2 Maximum spreading diameter

Maximum spreading diameter, denoted by D_{max}, refers to the diameter of the maximum droplet-solid contact area following the impact. D_{max} is closely relevant to the coverage efficiency of pesticide and paint sprays, and the quality of inkjet printing, therefore has received much attention. It is commonly presented in the dimensionless form as $\beta_{max} = \frac{D_{max}}{D}$, where β_{max} is the maximum spreading ratio, and D is the droplet diameter before impact.

Let us first review some theoretical approach of predicting D_{max} (or β_{max}) for a given droplet impact. Assume the impact surface is completely wettable by the incoming droplet, balancing the initial kinetic energy of the impacting droplet ($\rho D^3 {U_i}^2$) and the energy dissipation by viscosity $\eta(\frac{U_i}{h}){D_{max}}^3$, h is the thickness of the droplet at D_{max} and η is the dynamic viscosity, together with volume conservation ($h{D_{max}}^2 \sim D^3$), researchers[60, 76] have obtained a scaling of $\beta_{max} \sim Re^{1/5}$, where Re is the Reynolds number $Re = \rho D U_i/2\eta$. If the impact surface is super-repellent towards the droplet, because of the high contact angle, the viscosity dissipation is minimised, the kinetic energy is purely transferred into surface energy ($\sigma {D_{max}}^2$) as proposed by Richard et al.[77], this yields $\beta_{max} \sim We^{1/2}$. Moreover, if a surface is between those two extreme cases and has moderate repellency, combining volume conservation and the 'reinforced gravity field' concept, Clanet et al.[78] has found a new scaling of

$\beta_{max} \sim We^{1/4}$. Viewing the theories collectively, we may safely conclude that the surface wettability seems to determine the dynamics of inertia-driven spreading following the impact.

On the experimental side, many data[79-82], relating to the impact of droplets on different surfaces, have suggested that $We = 200$ is the threshold for the surface wettability to determine β_{max}. Below the threshold, higher surface wettability results in lower β_{max}, and above the threshold, β_{max} weakly conforms to an empirical scaling of $\beta_{max} \sim We^{1/5}$ [81].

For $We \leq 200$, experimentalists have found that the power-law of the pattern $\beta_{max} = We^{\omega}$ describes the impact of droplets on almost all types of solid substrates, ranging from smooth impermeable solids to porous unconsolidated powder[66, 78, 83-86], with $0.2 \leq \omega \leq 0.5$. Recently, by impacting droplets on pre-wetted powder beds, Marston et al.[87] have found that α is affected by the liquid concentration of a porous medium. Their research has implied that the relative humidity plays a non-negligible role in the determination of the maximum spreading.

2.2.3 Receding and bouncing of droplet

Between D_{max} and droplet receding, there is a short transition period for the contact angle with respect to the impact surface to switch from the advancing to the receding angle. And during this period the triple line velocity U_e remains 0 m/s[88]. When the droplet enters the receding stage, the flattened volume on the impact surface is pulled back by the surface tension. A typical receding outcome for liquid-repellent surfaces is droplet bouncing, referring to the droplet leaving the impact surface and temporarily ascending in the direction opposite to the impact velocity vector. Both receding and bouncing (particularly bouncing) have received much attention due to the relevance in the design of self-cleaning and ice-repellent surfaces.

Bouncing can be either partial or full, as summarised in figure 3 of Ref. [89]. The two situations are separated by a threshold receding angle of 100° for the impermeable substrates[90]. In full bouncing, recent experimentalists[65] have visualised 'pancake' and 'recoiling-bouncing'[61] on micro-architectured[65, 91]

surfaces, following some slight adjustment of the micro-post architecture. Tapered micro-posts cause the droplet to leave the impact surface in a pancake-shaped topology. Because the liquid menisci in the interstices of such micro-posts are subjected to an increasing deceleration as they move deeper into the interstices during the impact, the deceleration could initiate bouncing before the droplet reaches the maximum spreading diameter. On the other hand, straight micro-posts cause the droplet to bounce conventionally because the menisci are subjected to a constant deceleration.

Partial bouncing is full bouncing jeopardised by the invasion of droplet volume into the surface roughness due to the roughness protrusion[92], and is characterised by the sticking of a fraction of the volume to the impact surface. Partial bouncing occurs commonly on micro-patterned surfaces, when the impact pressure surpasses a threshold $P_{imp} \sim f(f_s, r^{-1})$, where r is the width of the micro-texture, f_s is the solid fraction of wetted area[92], respectively. Recent experimental data[74] have shown diverse partial bouncing depending on the surface roughness features, ranging from impinging-bouncing due to the droplet volume pinning in the roughness, to the more rarely observed inverse jetting and bouncing with entrapped air bubbles.

It has been found recently that the reduction of the contact time t_c between droplet and solid prior to bouncing is important to ice repulsion at low temperatures[56-57]. By altering the surface topological features, researchers have reduced t_c by 30-40% compared to that for surfaces with unaltered features[63-64, 93]. Moreover, the bouncing mechanisms on surfaces with altered topology are similar in terms of the splitting of the droplet volume into several small portions followed by the rapid recoiling and bouncing of the individual portions. For example, on super-hydrophobic smooth surfaces, the incorporation of ridges of 100 μm height would result in a butterfly wing-shaped volume splitting followed by a rapid recoiling of the splitted volumes along the ridges[63]. Whereas the incorporation of micro-wires would result in the generation of satellite droplets after the impact[93]. Moreover, the impact of droplets on super-hydrophobic cylindrical surfaces can cause symmetrical

splitting in the direction along and normal to the curvature of the surface. This symmetrical but anisotropic splitting also reduces the contact time.

2.2.4 Splashing of droplet

Splashing mechanisms of the impact of droplets on liquids: droplet splashing is typically divided into two categories based on the medium that the impact occurs on: splashing on liquids and on solids. In the case of splashing on liquids, for droplets landing on liquid tanks[94] or pre-existed liquid films[95], the droplets would typically form a crown-shaped topology (figure 1 of Ref.[61]) and the rim of the crown would propagate outward radially. The 'splashing' in this cases is the generation of secondary droplets from the crown rim and is referred to as 'corona splash'. The crown radial position r_c has been found to vary linearly with $t^{1/2}$ [94]. Moreover, the scaling becomes $r_c \sim t^{1/5}$ for the splashing of sprayed droplets[96]. The reason for this weaker dependence of r_c on time is the interaction of crowns produced by neighbouring impacting droplets[96]. If no interaction exists, it has been found that the crown height h_c varies linearly with r_c at a rate $\frac{dh_c}{dr_c} = 0.57$ [94]. In addition, the crown wall thickness has been found to be $0.2D$ and remains constant throughout[97].

In contrast to the observed 'corona splash' for $We < 1000$ [91], recently Thoroddsen et al.[98] have identified a 'slingshot' splashing mechanism for the impact of droplets at an ultra-high $We \cong 2000$. In brief, when a droplet strikes a liquid film, from the 'neck' that connects the two liquid masses, a submicron ejecta sheet is generated. Driven by air pressure, the ejecta sheet bends down towards the liquid surface. Once the ejecta sheet touches the liquid surface, it ruptures and breaks into secondary droplets.

Splashing mechanisms of the impact of droplets on solids: for the splashing on solids, typically at the end of the initial collision stage (section 2.2.1), an axisymmetric liquid film would expand radially outward over the surface. The liquid film may become unstable as the expansion progresses, leading to regular azimuthal undulations[99], the growth of which would result in the formation of 'liquid fingers' from the leading cusp of the liquid film. As the liquid fingers keep extending, secondary droplets would pinch off and this

phenomenon is termed 'prompt splash'[100]. Moreover, 'corona splash' on solids has also been reported[100-101] and the mechanisms are similar to those for splashing on liquids.

Splashing reduction: in many practical cases, such as the spraying of pesticide on plants, 'splashing on solid' (corona and prompt splash) must be minimised for the maximum spray efficiency and the minimum water or soil pollution. Recent study[101] has shown that splashing could be effectively reduced by the reduction of the ambient air pressure P_{air}. In brief, splashing occurs when the shock in air, caused by fast azimuthal drop spreading on the surface having a scaling $\mathrm{E}_G \sim P_{air} a U_e$, overcomes the stress that keeps the liquid film in contact with the solid $\mathrm{E}_L \sim \sigma/\sqrt{U_L t}$ (σ the surface tension, U_L is the kinematic velocity of the liquid)[101]. The ratio of $\mathrm{E}_G/\mathrm{E}_L$ is proportional to the ambient pressure, concluding that the reduction of splashing can be achieved by the reduction of the air pressure. However, some researchers[74] have reported the same type of splashing for impact at $We \leq 150$ on carbon nanofibre substrates for $14.7 \leq P_{air} \leq 101.3$ kPa. Instead of changing P_{air}, they have found that the reduction of the local roughness irregularity of a surface significantly reduces or even eliminates splashing.

In drop-based printing techniques and maintaining sterile medical environment[102], splashing must be eliminated. Splashing is reduced or eliminated by soft substrates, because the early-time deformation absorbs the kinetic energy of the ejecta sheet and prevents the liquid sheet from rupturing into secondary droplets[103]. The deformation occurs when the pressure peak of the impact $p_k \sim R U_i/(t - t_i)$ (t_i is the time before the drop is slowed by air cushioning effect), overcomes the Young's modulus E of the substrate. In addition, splashing can be reduced by the utilisation of surfactants in the liquid[104]. Short-chain surfactants are highly mobile so that they form densely packed molecular layers at the liquid-air interface before the splashing commences. Splashing can also be reduced by the pinning of liquid[105]. When a pair of drops containing polyelectrolytes with opposite charges impacting each other, the polyelectrolyte molecules attract one another and stick to the surface defects for the splashing prevention[105].

2.2.5 Droplet impact on porous media

Critical velocity of penetration: in the case of the impact of droplets on hydrophobic meshes, much work[14, 73] has qualitatively characterised the three impact regimes, namely 'no penetration', 'protrusion' and 'complete penetration'. Through the balance of the dynamic impact pressure $P_d \sim \rho U_c^2$ and the capillary pressure $P_c \sim \sigma\Gamma/A$, where A and Γ are the area and the perimeter of mesh pore, respectively, the critical 'impact-penetration' velocity U_c that separates 'no penetration' and 'complete penetration' has been found to scale as $(\sigma\Gamma/A)^{1/2}$ [14]. 'Protrusion' is a unique transition where a portion of the droplet protrudes the mesh pores temporarily, even when $P_d < P_c$. Because at the initial moment of 'protrusion', the resisting force was only the vertical component of the capillary force and is much smaller than the $\sigma\Gamma$ considered in the above pressure balance[106]. Interestingly, for super-hydrophobic meshes, except for the 'impact-penetration', droplet penetration also occurs at a 'recede-penetration' velocity of $U_r \sim (\sigma\Gamma/A)^{1/3}$ [14] during the droplet receding. The 'recede-penetration' occurs more likely than the 'impact-penetration' as it is less dependent on $P_c \sim \sigma\Gamma/A$. The reason is that the timescale for the 'recede-penetration' $\sim(\rho D^3/\sigma)^{1/2}$ is smaller than for the 'impact-penetration' D/U_i, while the momentum of impact is the same, due to the negligible friction dissipation. This discovery implies that the improvement of the surface chemistry alone does not make the liquid repellency of the mesh better.

Effect of mesh thickness on U_c: U_c has been found to increase by 50% when the depth of pore increased by an order of magnitude, due to the greater viscous dissipation the droplet encounters in a deeper pore[106]. In an extreme case, if the depth of the pore becomes much greater than the opening thereof, every pore becomes a capillary tube and a new penetration situation can be identified, where most of the droplet volume goes into the pores and forms liquid 'slugs'[107]. The critical velocity U_s for the slug formation is obtained through the balance of the capillary pressure at the bottom of the slug with the impact pressure and the inner Laplace pressure at the slug top[107].

Impact on single-holed solids: experimental data on the impact of droplets on single-pored solids, such as metal sieves[103] and capillary tubes[107], are available. The typical finding is the critical velocity obtained from pressure balance for the droplet penetration. Although the droplet penetration in these single-holed solids may be similar to that in meshes or textiles, the simultaneous lateral droplet spreading on these solids solely occurs on the non-porous portion of the solid. Whereas for meshes, due to the high porosity, the lateral spreading would occur on the porous portion of the solid. Some data[108] are available on the impact of water droplets on a single-pored substrate submerged in an oil bath. Since the oil is attached to the wall of the pore, surface wettability has no effect on the penetration dynamics but the opening of the pore from rounded to sharp-edged determines the dynamics. However it is practically difficult to completely eliminate the effect of surface wettability when the impact experiments are conducted in air.

Generation of satellite droplets: in the case of complete penetration, liquid jets form and extend from the opposite surface of the mesh. Previous experimental data[106] have shown that the maximum length L of the jet before rupturing into secondary droplets scales as $L{\sim}U_i\sqrt{\frac{\rho {d_{mesh}}^3}{\sigma}}$, where d_{mesh} is the mesh pore size. The number of the secondary droplets generated per jet has been estimated as $n \approx (L/\pi d_{mesh}) + 1$ [106].

Droplet bouncing on mesh: conventional 'recoil-bouncing'[109] and more rarely observed 'pancake bouncing'[14, 110] (refer to section 2.2.3 for the definition of pancake bouncing) have been reported on super-hydrophobic meshes. Meshes having an oval shaped yarn cross section, can provide increasing deceleration, as the liquid menisci move deeper into the pore. Moreover, the pancake bouncing was not observed on hydrophobic meshes, possibly because of the severe liquid 'protrusion' after the impact.

Impact pressure: It has been reported that at $t \approx D/8v$, the impact force onto the substrate reaches its peak[75]. And the resultant pressure, on impermeable substrates, reaches approximately $2\rho v^2$, higher than the commonly considered P_d by a factor of 4[16]. In some recent papers on the

impact of droplets on non-wettable microtextured surfaces[111], microgirds[112] and meshes[18], researchers have introduced a 'water hammer' P_{WH} for the reference of the peak pressure. Essentially P_{WH} is generated due to the temporary volume confinement at the bottom of the droplet at the moment of impact, and is assuaged by the droplet lateral motion and the vertical crossing through the voids of the substrate[111] (section 2.2.1). For non-wettable meshes, P_{WH} has been found to scale as $k\rho U_i{}^2$, with k increasing inversely with d_{mesh} from 1 to 4[18].

Maximum spreading diameter on mesh: A notable scaling $D_{max} = D \cdot We^{1/4}$, initially found for the impact of droplets on impermeable substrates[78] (section 2.2.2), has recently been confirmed for the description of the experimental data for the impact on non-wettable meshes reasonably well, if the solid fraction ϕ of the mesh is no smaller than 70%[110]. For meshes with $\phi < 70\%$, due to the severe leaking of the droplet volume, especially at relatively high We ($30 < We < 100$), D_{max} no longer conforms to the scaling.

2.3 Surface chemistry: perfluorination

Perfluorinated polymers are important to many applications, from the production of catalysts and reagents for organic synthesis[113-114], to the control of the synthesis of peptides and proteins[115], and particularly, to the

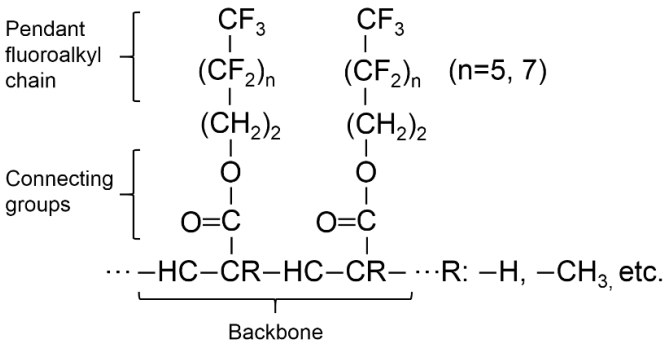

Figure 2-9. Schematic diagram of the structure of a perfluorinated polymer, the polymer structure typically consists of pendant fluoroalkyl chains, connecting groups and backbone. $n = 5$ and 7 show the most commonly used perfluorinated polymers for coating.

development of super-hydrophobic or superoleophobic materials[116-117]. The outstanding liquid repellency is benefited from the low surface energy $1.5<\sigma<27.0$ mN/m[118-122] of the pendant fluoroalkyl chains[123] (abbreviated as 'F-chains' in the following text) and the flexibility of the backbone[124], as illustrated in figure 2-9. This section reviews a series of parameters that affect or determine the liquid repellency.

2.3.1 Crystallisation of the 'F-chains'

The super-repellency toward liquids is achieved by not only the low surface energy, but also the low contact angle hysteresis (CAH) of a perfluorinated polymer. Low CAH emphasises the easiness of liquid shedding of a material when tilted and is achieved by the homogeneous 'crystallisation' of the 'F-chains'.

'Crystallisation' in this context refers to the parallel alignment of the F-chains in a fashion that is normal to the backbone[125]. The well-aligned F-chains form a firm, smooth and well-organised polymer outermost surface. Crystallisation is affected greatly by the cooling rate at the end of the synthesis process[126]. Historically 'water quenching' and air annealing', representing high and low cooling rates respectively, were used and compared. 'Water quenching' typically leads to poor crystallisation because this method provides insufficient time for the F-chains to align[127], and consequently resulting in high CAH[122, 127]. Moreover, the $-CF_3$ groups at the end of the F-chains (figure 2-9) are re-arranged towards the bulk polymer due to the strong repulsion of the polarised water molecules, leading to poor 'electrical screening' effect[127]. This makes crystallisation much weaker and consequently results in high CAH. On the other hand, experimental data[128] have shown that the slow 'air annealing' results in good crystallisation and consequently gives small CAHs.

2.3.2 Effect of F-chain length on polymer properties

For air annealed polymers, the length of the F-chains, mainly determined by the number n of figure 2-9, greatly affects the quality of crystallisation. It has been found that CAH would decrease by a factor of 2 when n increases from 5 to 7[118]. For n=7, the F-chain crystallisation is the best, as implicated by

circumstantial Differential Scanning Calorimetry (DSC) analysis[118]. Subsequently it has been observed using Wide Angle X-ray Diffraction (WAXD) that long F-chains are favoured for the formation of a smooth and flat outermost polymer surface for the achievement of small CAH[118].

For $n \leq 5$, due to the 'internal plasticisation', caused by the bulkiness of the $-(CF_2)_n-$ groups, the F-chains would be too unstable to align for the crystallisation[129]. This 'internal plasticisation' has small effect on the crystallisation for $n \geq 7$ and completely no effect for an $n \geq 17$ [130]. More recently, it has been found that for $n \leq 5$, crystallisation only occurs when the –R group is α–CH_3[131], or $-CH_3$ [122-123]. Because α-CH_3 and $-CH_3$ are bulky and they provide enough van der Waals repulsion for the restriction of the mobility of the F-chains, polymers with α-CH_3 and $-CH_3$ typically offer a good crystallisation.

2.3.3 Surface energy σ of perfluorinated coatings

It has been found that the surface energy σ would be affected by the carbon atom in the 'F-chain' that makes up the outermost polymer surface layer. Pittman and Ludwig [128] investigated the wettability of PFAs (poly(perfluoro acrylate)) in both monolayer acid form and acrylate film form. They found that for PFAs where primary carbon atoms (e.g. $-CF_3$, $-CH_3$, etc.) make up the surface layer, the more densely packed $-CF_3$ layer from longer fluoroalkyl side chains would offer a lower surface energy. Interestingly, PFAC10 ($n = 9$) film with $-CF_2H$ end group offered the same surface energy as the PFAC10 monolayer acid with the same end group. Furthermore, monolayer acid with $-CF_3$ end group showed lower surface energy than acrylate film with the same end group. This feature was thought to be a result of the poor fluoroalkyl side chain alignment and surface exposure of polymer backbone for the films [121, 128]. On the other hand, for PFAs where secondary carbon atoms (e.g. –CFH-, $-CH_2-$, etc.) make up the surface layer, longer side chains do not offer lower surface energy. Instead, the resultant surface energy depends on the conformation arrangements of the fluoroalkyl groups and the resultant packing. Stone et al [132] also found that when the primary carbon atoms formed the surface layer, the surface energy of PFAC10 was estimated to be

approximately 6mJ/m^2 and this value was much lower than the surface energy of the same polymer having the surface layer formed by the secondary carbon atoms, as reported by Pittman and Ludwig [128].

Additionally, it has been found that in an 'F-chain', the carbon atoms appeared to be in different planes[133]. This feature is in contrast to the structure of a hydrocarbon chain, where all the carbon atoms are in the same plane for the formation of a zigzag configuration[134]. The multi-plane configuration of the F-chain has been explained with the hypothesis of the chain bond rotation for the increase of the distance between the fluorine atoms[133]. Geometrically, there is a satisfactory configuration where a rotation could bring one fluorine atom equidistant from the other two on the next-but-one carbon atom[133-134]. But the satisfactory configuration has never been observed and no attempt was made to explain the non-equidistant feature.

2.3.4 Surface roughness introduced by perfluorinated coatings

For the understanding on the super liquid repellency of the perfluorinated polymers, while many explanations have been made from the chemistry perspective (section 2.3.1 and 2.3.2), some work has focused on the roughness of the pure perfluorinated polymer films and the role that the roughness plays in the surface wettability. Bellanger et al.[117] have found that for $n \geq 7$, perfluorinated polymer films have relatively significant roughness varying from 1$\sim$10 μm). Their experimental data[117] have shown that the static contact angle on the films increases with the surface roughness. Using Scanning Electron Microscopy (SEM), Jiang et al.[135] have confirmed that the surfaces of the perfluorinated polymer films are rough. Similarly, their data have shown increasing oleophobicity with the roughness[135].

However, some researchers have argued that when $n \geq 7$, the surfaces of perfluorinated polymer films should be completely flat. Using Atomic Force Microscopy (AFM), Katsuragawa et al.[127] and Graham et al.[124] have found that the roughness is in the range of 0.7 – 1.8 nm for $n \geq 7$. Moreover, Graham et al.[124] have occasionally seen the roughness for $n = 7$ is merely 0.5 nm, possibly due to the extremely smooth drop of temperature during the air

annealing process. These authors have argued that the sub-nanoscopic roughness should have no effect on the liquid repellency.

A systematic study on the change of the surface energy caused by the substitution of F with H and Cl was conducted by Pittman[121]. They found that the substitution of one F atom on a secondary carbon with Cl would result in a surprising increase of 12.5 mN/m for the surface energy. Whereas the substitution of such F atoms with H atoms would only result in a minor increase of 3.5 mN/m. In contrast, the substitution of one F atom on a primary C with Cl resulted in minor increase of 4.8 mN/m for the surface energy. However the surface energy does not increase linearly with the percentage content of the fluorine atoms in a particular polymer. They emphasised that the surface energy was not necessarily dependent on the fluorine content but on the arrangement of the fluorine atoms in a particular polymer.

Pittman et al.[121] also studied the effect of chain length on the surface energy of a particular fluoro-polymer. The chain length referred to in their study was not the number of the perfluorinated carbon atoms but the total number of the carbon atoms in a side chain. Their data showed that long fluoro-carbon side chain would always offer a significantly lower surface energy of ~ 10 mN/m, no matter for PFAs, PFMAs or even polymers having a large connecting group. In contrast, a short fluoro-carbon side chain would offer a considerably greater surface energy of ~ 15 mN/m. They concluded that a short fluoro-carbon chain meant an overall high hydrocarbon content which would result in an increased wettability.

For a given fluoropolymer having a fixed y number, the σ_c was reported to be a function of time by Stone et al.[132]. Interestingly the surface energy appeared to increase with time and the increase rate was reversely proportional to the fluoroalkyl chain length [132]. For $n \geq 7$ only minor increase of surface energy was measured. Whereas for $n < 7$, the surface energy became about twice as the original value after merely 30 minutes. This decrease of surface energy was thought to be caused by the penetration of the surfaces by the liquids utilised for the contact angle measurements by Graham et al.[124].

2.3.5 Toxicity of perfluorinated coatings

Perfluorinated polymers, specifically perfluoroalkyl and poly(perfluoroalkyl) substances, will release perfluoroalkyl acid and perfluoroalkylsulfonate, i.e., perfluorooctanoic acid (PFOA) and perfluorooctanesulfonate (PFOS) through oxidation[135]. These released substances are bioaccumulative and non-degradable therefore hazardous to all creatures[136-137]. A notable work by Kannan[138] has provided a summary of the released toxic compounds in the perfluoroalkyl family and the toxicity mechanisms of the compounds after entering our biological system, making the usage of the perfluorinated polymers a controversial topic.

The toxicity potential of the perfluoroalkyl polymers is highly dependent on the length of the fluoroalkyl side chains. Recent papers[139-140] have reported that the toxicity greatly decreases when n (defined in figure 2-9) is below 5. But for $n < 5$, as mentioned in section 2.3.2, the crystallisation of the 'F-chains' becomes poor, resulting in poor repellency performance. Until today, we could not find a solution for the balance of the toxicity and the repellency from the literature.

3 Liquid permeation of a static droplet in an oleophobic textile

3.1 Introduction

Oleophobic textiles have received attention due to the importance in the design of protective clothing[1], domestic apparel and in many other engineering fields[141-144]. Fluorinated coatings typically having a low surface energy of the order of 10 J/m^2 are crucial to the manufacture of oleophobic textiles. To ensure the oleophobicity or superoleophobicity of the produced textiles, the application of fluorinated coatings is often accompanied by the deposition of micro- or nano-particles during the manufacturing process[142, 145]. A recent study on the design of oleophobic nano-fibre mats has shown possibility in the achievement of oleophobicity for a fibrous medium using only a fluorinated coating known as 1H,1H,2H,2H perfluorodecyl acrylate (PFAC8)[146]. This study opens a simpler path toward the production of oleophobic textiles.

In this chapter we report that PFAC8 textiles occasionally fail to repel droplets with low surface tension and allow the formation of liquid-wetted regions on the opposite surface through transplanar liquid permeation. For the development of the permeation mechanism, we attempt to show the permeation process using the bottom view of a textile. For the prediction of the liquid permeation for a given PFAC8 textile, we develop an equation for the critical pore size of permeation by considering the pressures that act on the liquid meniscus in a textile pore.

3.2 Material and methods

3.2.1 Fluid and textiles

The working fluid (referred to as 'oil') is a non-volatile polydimethylsiloxane (assay of purity≈99.5 %, Sigma-Aldrich, UK) with a dynamic viscosity of $\mu \approx 1$ Pa·s and a surface tension of $\sigma \approx 20$ mN/m at the room temperature of $T \approx 20$ °C.

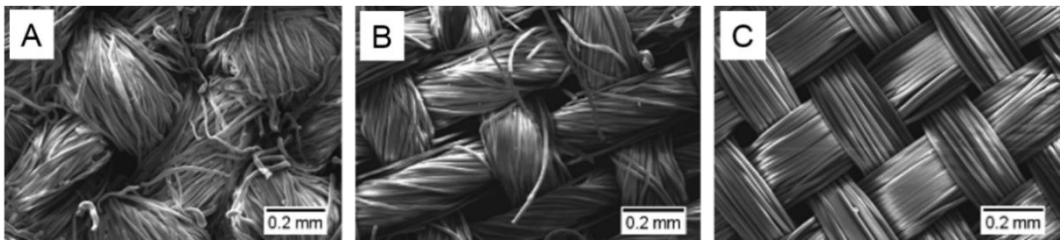

Figure 3-1. SEM images of three woven textiles: A pure cotton; B polycotton (cotton wt% ≈ 33%); C pure polyester.

The experiments of the in-plane oil spreading were carried out in uncoated cotton (figure 3-1A), polycotton (figure 3-1B) and polyester (figure 3-1C) textiles. These textiles have similar woven structures but slightly different surface roughness characteristics, pore shapes and yarn structures.

The experiments of the transplanar oil permeation were carried out in fluorinated polycotton and nylon textiles. The largest pore sizes of the nylon textiles are in the range of 100 – 600 μm.

3.2.2 Measurement of in-plane spreading radius

For the interpretation of the in-plane oil spreading dynamics, the time evolution of the in-plane spreading radius $R(t)$ was recorded with an optical microscope (Dinolite AM4515ZT, UK) placed several centimetres above the textile plane. The wetted region in the textile surface is rendered evident using the brightness and contrast tool of ImageJ. $R(t)$ was directly measured from the segmented images.

For polycotton and polyester textiles the in-plane spreading progressed more quickly in one direction than in other directions[6]. In this case $R(t)$ was estimated as:

$$R(t) \approx \sqrt[3]{R_{min}(R_{max})^2} \tag{3.1}$$

Where R_{max} and R_{min} are the largest and the smallest spreading radius. Here we only study the in-plane spreading dynamics for $R_{max} \leq 1.1R_{min}$ [6].

We point out that the estimated $R(t)$ by equation (3.1) does not reflect accurately the spreading radius in all directions. However, since R_{max} is by no

means much larger than R_{min} ($1.1R_{min} < R_{max} < 2R_{min}$ in this study), $R(t)$ by equation (3.1) could be accepted as a relatively accurate representation of the real spreading radius in any direction.

3.2.3 Pressure-driven oil permeation across PFAC8 textile

Figure 3-2 illustrates the experimental setup for the study of the transplanar oil permeation across PFAC8 nylon textiles. Textile samples were fixed by clamps at both ends and a plastic tube was placed on the sample. The oil was injected into the tube at a rate of 1 ml/h. The driving pressure P of the transplanar permeation was determined by the oil column height $h(t)$ and $P = \rho g h(t)$. The use of 1 ml/h injection rate is for the minimisation of the kinetic energy that was added to the oil column.

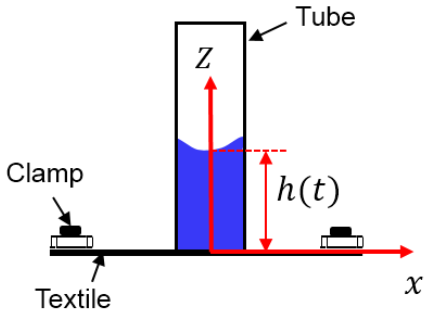

Figure 3-2. Experimental setup for the measurement of the permeation pressure in PFAC8 textiles. The tube is placed perpendicular to the textile plane. The blue region in the tube indicates 'oil'.

3.3 Results and discussion

3.3.1 Characterisation of PFAC8 textile oil repellency

The oil repellency of the PFAC8 textile was evaluated through droplet deposition on the front textile surface. Figure 3-3 (a) – (d) shows that the deposited oil droplets having in-plane radii in the range of 1.34 – 2.29 mm stayed on the front textile surface in a spherical cap configuration. (e) – (h) showed the back textile surfaces corresponding to (a) – (d) respectively 72 hours after the droplet deposition and no wetted region could be observed. Therefore, our PFAC8 textiles have stable oil repellency to static droplets.

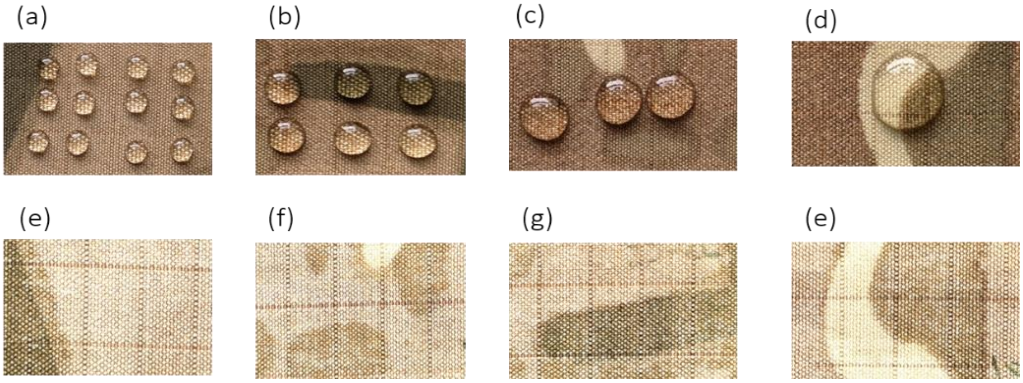

Figure 3-3. (a) – (d) oil droplets having various diameters on the front surface of a PFAC8 textile. (e) – (h) the back surface of the textile, showing no wetted oil stain, corresponding to (a) – (d), respectively. Radii of the droplets are (a) $R = 1.34$ mm, (b) $R = 1.44$ mm, (c) $R = 1.81$ mm, (d) $R = 2.29$ mm. (e) – (h) were taken 72 hrs after the droplet deposition.

Previous research on PFAC8 coated similar fibrous materials[1, 146] reported the pinning of oil droplets on the material surfaces. Here we showed in figure 3-4 that an oil droplet could also be pinned to the textile surface. Figure 3-4(d) showed the oil permeation in the interior of a textile yarn near the receding triple line. The permeated oil volume extended outward from the triple line forming a 'root'-like wetting configuration.

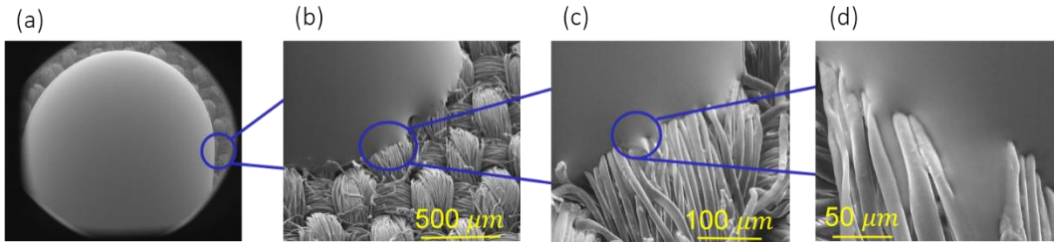

Figure 3-4. Environmental SEM images showing the oil pinning on a PFAC8 textile surface. The images were taken after the SEM sample stage was tilted 43°.

3.3.2 Defect-induced transplanar oil permeation

A local structural 'defect' was created by means of piercing a needle (diameter~2 mm) through a fixed PFAC8 textile, as shown in figure 3-5(a). The size of the defect, as shown in figure 3-5(b) and (c), was larger than the original

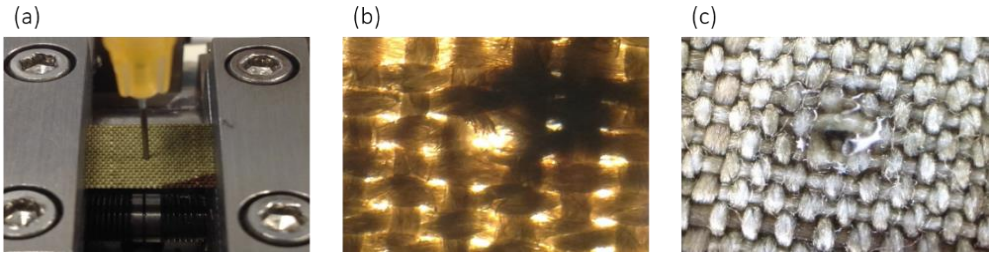

Figure 3-5. Oil permeation in a PFAC8 textile pierced with a large pore (diameter of the order ~2 mm) by a needle.

textile pore size. The shape of the defect approximated a sphere with a diameter of approximately 1.7 mm. When an oil droplet (diameter~2 mm) was placed on the defect, the permeation through the defect was characterised by the formation of the small wetted region on the back surface (figure 3-5(c)).

The pore size of a PFAC8 textile can be increased one-dimensionally by stretching. To stretch the textile we fixed a PFAC8 textile at both ends using clamps and moved the clamps in opposite directions. The stretching force was $F = 10 \pm 0.5$ N and the force caused about 5% increase of the pore size. For the study of the oil permeation rate we placed a $V_0 \approx 20$ µl oil droplet on the stretched textile. We recorded the time evolution of the droplet base length $a(t)$ and the droplet height $b(t)$. If the oil droplet is assumed to be a spherical cap, the droplet volume (unit: m^3) can be estimated as:

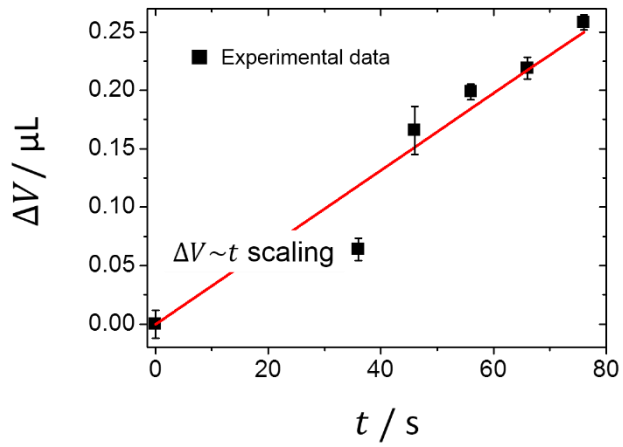

Figure 3-6. Permeated oil volume V as a function of time t. The error bar shows the standard deviation of 5 measurements.

$$V(t) = \frac{1}{6}\pi b(t)[(3a(t)^2 + b(t)^2] \quad (3.2)$$

With equation (3.2) we estimated the permeated droplet volume as $\Delta V \approx V_0 - [V(t) \cdot 10^9]$ (unit: μl) and showed the experimental data of ΔV at successive times in figure 3-6. Previous research[10] showed that the ΔV in multi-layer textiles and knitted textiles conforms to the scaling $\Delta V \sim t$. Our data showed that ΔV for single-layer woven oleophobic textiles also conforms to $\Delta V \sim t$.

3.3.3 Pressure-driven transplanar oil permeation

The permeation of an oil droplet in a 'defectless' PFAC8 textile can be initiated by an external pressure. Figure 3-7 shows a 'confined' oil droplet between two PFAC8 textiles having a pore size of about 500 μm. When the textile-to-textile distance was reduced to that of (d), oil stains appeared on the back textile surfaces. The pressure that induced the oil permeation in figure 3-7(d) is calculated as:

$$\Delta P = \frac{2\sigma}{R_c} \quad (5.3)$$

R_c is the characteristic radius of curvature and is estimated as:

$$\frac{2}{R_c} = \frac{1}{R_l} + \frac{1}{R_r} \quad (5.4)$$

R_l and R_r are the left and right curvatures of the droplet in figure 3-7(d), and $R_l \approx R_r$. Given $R_l \sim 10^{-3}$ m, $\sigma \approx 20$ mN/m, $\Delta P \sim 40$ Pa.

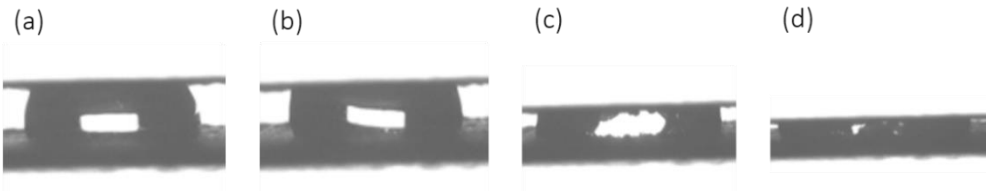

Figure 3-7. Droplet confinement method for the oil permeation. The droplet radius *R=1.5* mm corresponding to the dark grey curved part. Upper thin line indicates a PFAC8 textile and the bottom area shows another PFAC8 textile fixed on a glass slide. The white rectangular indicates the light reflection.

The oil permeation in PFAC8 textiles was observed from both the side and the bottom view for the interpretation of the permeation initiation mechanisms.

Figure 3-8(a) shows the overall picture of the permeation process in the side view. The droplet passed through the textile pores without much lateral

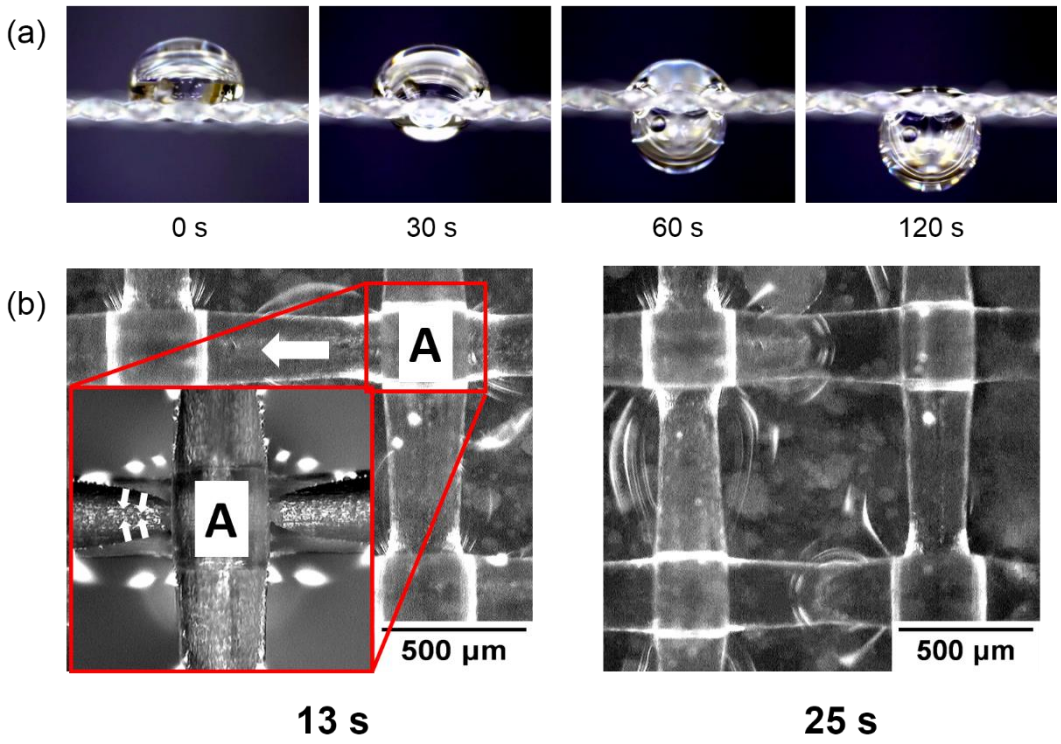

Figure 3-8. Front (a) and bottom (b) views of an oil droplet (*R*=1.34 mm) permeation through a PFAC8 nylon textile at successive times. Bottom views (b) show mechanisms of the initiation of permeation. The white arrows indicate the directions of liquid motion.

spreading on the textile surface. At $t \approx 120$ s most of the droplet volume was transported to the textile back surface.

The permeation mechanisms can be interpreted from the bottom view shown in figure 3-8 (b). The letter A indicates a junction of a horizontal and a vertical textile yarn. In the early stage of the permeation ($t \approx 13$ s), the back surface of the horizontal yarn of the junction A was invaded by the oil from the adjacent two pores and the oil movement is indicated by the small white arrows. Once the two invading oil fronts merged into a continuous oil front, the oil front moved from the junction A to an adjacent junction in the direction indicated by the large white arrow. The oil movement was evidently shown in the image for $t \approx 25$ s.

Observations at other junctions showed the same permeation mechanisms. Importantly, at every junction the permeation was always initiated at the back surface of the yarn whose front surface was in direct contact of the oil. We believe that the permeation mechanisms are universal for textiles with different pore sizes.

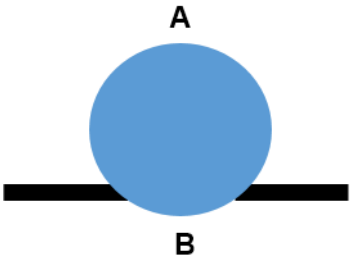

Figure 3-9. Simplified illustration of liquid on the surface of a PFAC8 textile, focusing on a textile pore.

3.3.4 Critical permeation pore size

Figure 3-9 illustrates a simplified view of an oil droplet on a PFAC8 textile focusing on the region of a textile pore. At the droplet bottom B the droplet weight applied a pressure P of the order $\sim\rho g h_{max}$, h_{max} is the droplet height from the droplet top A to the bottom B. The droplet was also subjected to a capillary pressure P_c of the order $\sim\frac{\sigma}{d_m}$, d_m is the pore size. Therefore, we obtain:

$$k_b P \approx P_c \tag{5.5}$$

at the onset of the permeation and k_b is a scaling constant for the permeation. Because $P_c \sim \frac{\sigma}{d_m}$, the critical permeation pore size obtained from equation (5.5) is:

$$d_m = \frac{\sigma}{k_b} P^{-1} \tag{5.6}$$

Figure 3-10 shows the observed permeation outcomes for liquid having different h_{max} on textiles having varying pore sizes. The symbol colours and shapes indicated the permeation outcomes and the pore sizes respectively. Equation (5.6) (the red curve) seemed to describe relatively well the boundary

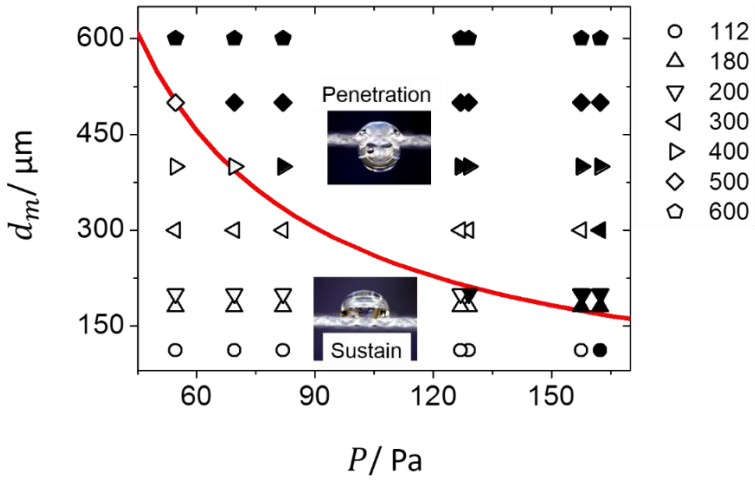

Figure 3-10. Phase diagram for the prediction of droplet permeation in PFAC8 textiles. The red line shows the best fitting to our data with $k_b \approx 0.49$. The symbol shapes indicate the textile pore size. The empty symbols indicate the liquid sustaining and the full black symbols indicate the liquid penetration as demonstrated in the insets.

between 'permeation' and 'sustain', with k_b ≈0.49 determined when d_m and σ are in the standard units.

Figure 3-10 also showed a few false predictions for (d_m, P)=(112 μm, 160 Pa), (300 μm, 130 Pa), (300 μm, 135 Pa) and (300 μm, 155 Pa). These prediction errors were likely due to the local irregularity of the textile geometry. For example, the textile pore sizes under the oil volume may fluctuate about the averaged d_m in equation (5.6). The pore size irregularity might be caused by the poor control of the textile weaving or the repetitive manual manipulation of the textile samples during the experiments.

In section 3.3.2 we observed oil permeation from droplets (diameter≈2.68 mm) at the created defect having a size of 1.7 mm. Because $\rho \approx 890$ kg/m^3, $D \approx 2.68$ mm, the permeation driving pressure $P \approx 23.4$ Pa. Therefore, the critical permeation pore size by equation (5.6) was $d_m \approx 1.7$ mm. This predicted pore size matched our experimentally created size well.

In chapter 5 a penetration criterion will be developed for droplet impact, demonstrating the differences between capillary and impact penetration.

3.3.5 Permeation and in-plane spreading in PFAC6 textiles

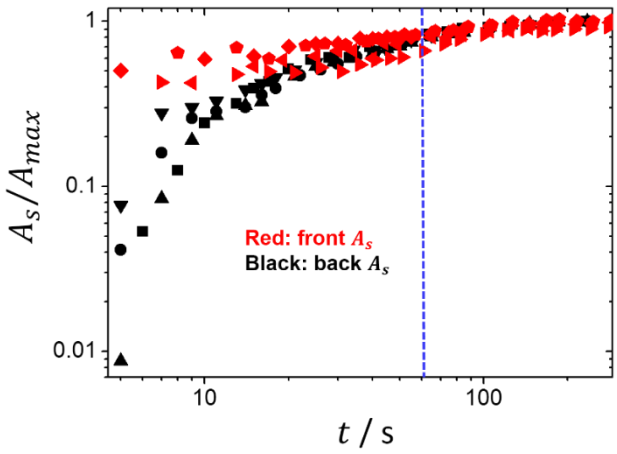

Figure 3-11. Dimensionless spreading area as a function of time for front (red symbols) and back textile surface (black symbols) on a log-log scale. Oil droplet is deposited on the textile front surface. A_{max} is the equilibrium spreading area.

PFAC6, a by-product from the synthesis of PFAC8, has a surface energy as low as that of PFAC8[125]. However, oil droplets on PFAC6 textiles would spread in the textile plane and permeate through the textile thickness. Figure 3-11 shows the time evolution of the in-plane spreading areas A_s on the front and back surfaces of PFAC6 cotton, polyester and polycotton textiles, following the oil deposition on the front surfaces. For all the textiles the front $A_s - t$ curves collapsed well and indicated a monotonic increase for $t \leq 100$ s. for $t > 100$ s the front curves became a horizontal asymptote and the spreading reached the equilibrium.

The back $A_s - t$ curves, however, showed a completely different spreading dynamics. In the initial stage for $t < 2$ s, the back curves showed $\frac{A_{s-back}}{A_{max}} \approx 0$, indicating that the back surfaces remained unwetted shortly after the oil deposition. The rapid increase of A_s for $2 \leq t \leq 60$ s should be interpreted as due to the oil permeation across the textile thickness. For $t > 60$ s the back curves collapsed well on the front curves, showing a uniform spreading dynamics after the permeation. We could interpret that the oil permeation was completed at $t \approx 60$ s for our PFAC6 textiles.

3.3.6 In-plane oil spreading in bare (uncoated) textiles

We are interested in the in-plane oil spreading dynamics for different textiles. The time evolution of the spreading area for cotton (dark green), polycotton (light green) and polyester (silver) textiles is qualitatively shown in figure 3-12A and the measurements of the spreading areas are shown in figure 3-12B. Only the spreading kinetics for the cotton textile conformed to the scaling of $A{\sim}t^{1/3}$, whereas for the other textiles the spreading kinetics could not be described by a single power-law. Our observations contradicted the popular belief[6-7] that the spreading kinetics for all fibrous materials conforms to $A{\sim}t^{1/3}$. We believe that the deviation of the spreading kinetics for the polycotton and polyester textiles from the scaling of $A{\sim}t^{1/3}$ is due to the anisotropy of the in-plane spreading.

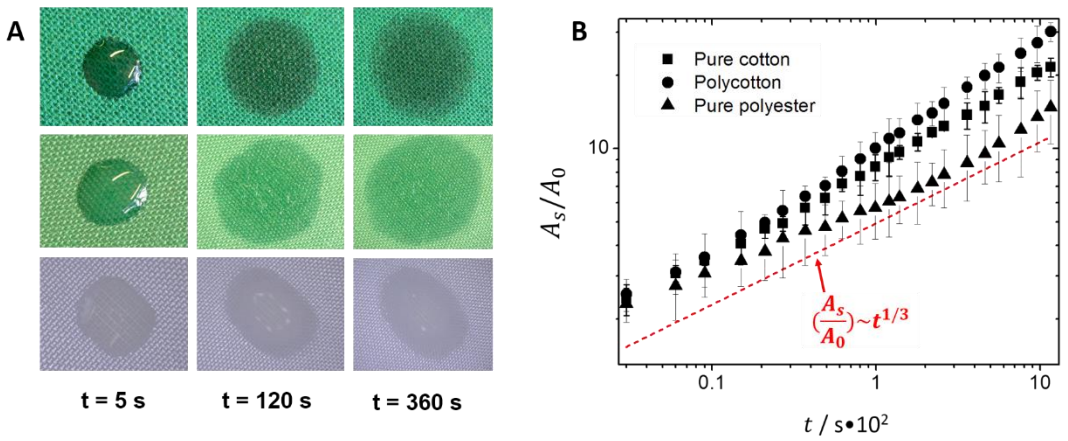

Figure 3-12. A: optical images of the in-plane spreading for a cotton (1st row), a polycotton (25 wt% cotton and 75 wt% polyester, 2nd row) and a polyester textile (3rd row). B: dimensionless time evolution of in-plane spreading area. Gillespie scaling, $\frac{A_s}{A_0}{\sim}t^{\frac{1}{3}}$ is indicated by the red dot line.

The deviation here may also be caused by the prediction 'inconsistency' from the scaling model. As discussed in chapter 2, $A{\sim}t^{1/3}$ was derived from the Gillespie equation[6] $\frac{\partial C}{\partial t} = -\frac{\beta}{r}\frac{\partial C^3}{\partial r}$ and the equation of continuity from Ref.[53] based on the droplet volume conservation and subjecting to the boundary condition of:

$$C = C_0, \text{ at } r = 0 \text{ and } t = 0$$

$$C = 0, \text{ at } r = R \text{ for all } t$$

R is the radius of the spreading area, C is the liquid concentration of the porous medium under consideration, C_0 is the maximum liquid concentration of the porous medium. The time dependence of R was unfortunately neglected in the boundary condition[147]. The negligence of the time dependence of R would cause inaccuracy in the spreading prediction particularly for textiles with low surface roughness, where the in-plane spreading will not be hindered severely by the out-of-plane fibres.

3.3.7 Droplet impact effect on in-plane spreading

The deposition of droplets in our experiments typically requires the utilisation of a pipette. The released droplets from the pipette will inevitably grant a velocity v. We are interested in the effect of this v on the in-plane spreading on a relatively large timescale.

Oil droplets (about 15 µl) were released from different heights h to achieve different v. Based on the assumption of a complete energy transfer from the potential energy ($\sim mgh$) to the kinetic energy ($\sim \frac{1}{2}mv^2$), v is estimated as $v \approx \sqrt{2gh}$. For $0.2 \leq h \leq 0.5$ m, we have $0.5 < v < 1$ m/s.

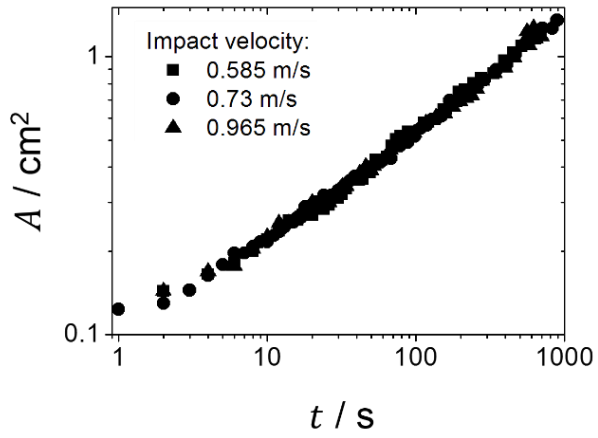

Figure 3-13. Effect of droplet impact on in-plane spreading at large timescales

The time evolution of the in-plane spreading area A for $0.5 < v < 1$ m/s collapsed well on a single line in log-log, indicating the same in-plane kinetics, as shown in figure 3-13. For the investigated time $1 < t < 10^3$ s, the in-plane

spreading is the liquid propagation in the textile interior is only driven by capillarity following even the drop impact. In chapter 5 we will observe the drop impact at a much more superior temporal resolution for $t \ll 1$ s for the understanding on the role of inertia.

3.4 Conclusions

Transplanar permeation of oil droplets across PFAC8 textiles was investigated with a series of experiments. The oil permeation was mainly a gravity-driven process. For a PFAC8 textile, the critical permeation pore size $d_m \sim \frac{\sigma}{P}$ was obtained by the balance of the pressure P from the liquid weight and the capillary pressure. The simple model of $d_m \sim \frac{\sigma}{P}$ can aid the design of textiles repellent to any static liquid droplets.

The initiation of the oil permeation in defectless PFAC8 textiles starts at the yarn 'junctions' from the back surface of the yarn that is in direct contact with the liquid. After wetting the back yarn surface near the junction, the oil propagates along the selfsame yarn and moves to an adjacent junction as shown in figure 3-8.

The in-plane spreading kinetics for uncoated textiles does not conform to the well-known Gillespie scaling of $A \sim t^{1/3}$ in the case of anisotropic spreading. The deviation of the kinetics may also due to the negligence of the time dependence of the spreading radius in the boundary conditions of the Gillespie's theory. For isotropic in-plane spreading in cotton textiles, the spreading kinetics conformed rather well to the Gillespie scaling, as shown in figure 4-12.

4 X-ray imaging of the transplanar liquid spreading in single-layer textiles

4.1 Introduction

The movements of a liquid in a single-layer textile are important to protective clothing[23, 148] and wearability improvement[5, 24]. The movements are the liquid spreading in the plane of the textile and the liquid permeation (or penetration) in the transplanar direction of the textile. When a droplet is deposited onto a textile surface, the spreading of the liquid from the droplet typically progresses in stages[149-151]. In stage 1 the liquid spreads through the textile and vertically saturates the textile thickness. In stage 2 the liquid mainly propagates along the textile plane in the interior of the textile. In the literature, stage 2 has been well understood[149, 151-152] whereas stage 1 has received little attention. Previous research on the transplanar liquid spreading in a single-layer textile have only been carried out to measure the transplanar spreading liquid volume as a function of time[33-34]. No attempt on the visualisation of the transplanar spreading process has been made. Therefore in this chapter we provide a time-resolved advancing liquid front position in the textile thickness (of the order ~ 100 μm) using an ultra-high viscosity liquid and the X-ray imaging approach. From the imaging data we interpret the mechanisms of transplanar spreading while attempting to associate the spreading mechanisms with the multi-scale textile geometric features. By plotting the liquid front position as a function of time, we discuss the dynamics of transplanar liquid spreading. Finally, we compare the dynamics with the classical Washburn theory and emphasise the unique transplanar textile geometric features for the development of theoretical models.

4.2 Material and methods

We study droplets of silicone fluid spreading through single-layer woven cotton textiles. The woven structure is produced by aligning textile yarns at right angles to one another. Fibres of the yarns are cotton and polyester mixed at a ratio of 19:1 (95 wt. % cotton). The textile thickness is approximately 300 μm. Imaging low viscosity liquids spreading through such a thickness requires

time resolution smaller than 0.1 s[153], making the direct visualisation of the spreading process challenging. To overcome the time resolution limits, we use viscous silicone fluids (100% polydimethylsiloxane, abbreviated as 'PDMS'), $\mu_1 \approx 97$ Pa·s (Sigma-Aldrich) and $\mu_2 \approx 2.4 \cdot 10^3$ Pa·s (Clearco Products) to slow the spreading kinetics to enable 3-dimensional (3D) X-ray imaging. Both of the fluids are non-volatile at room temperature. The liquid-vapour interfacial tension for both fluids is $\sigma \approx 19 - 21$ mN/m. In addition, PDMS fluid displays shear thinning behaviour at sufficiently large values of the shear rate[154]. In our case, because of the relatively small shear rate values characteristic of flow within the textile (we estimate $\dot{\gamma} \approx 1 - 10$ s^{-1}), non-Newtonian effects are neglected in the analysis. To simplify the identification of the silicone fluid type in the discussion, we will refer to the fluids as 'μ_1 fluid' and 'μ_2 fluid', respectively.

4.2.1 X-ray computed micro-tomography (XCT)

An X-ray microscope consists of an-X-ray source (tube), a rotation stage and an X-ray detector, as shown in figure 4-1A. The components are aligned

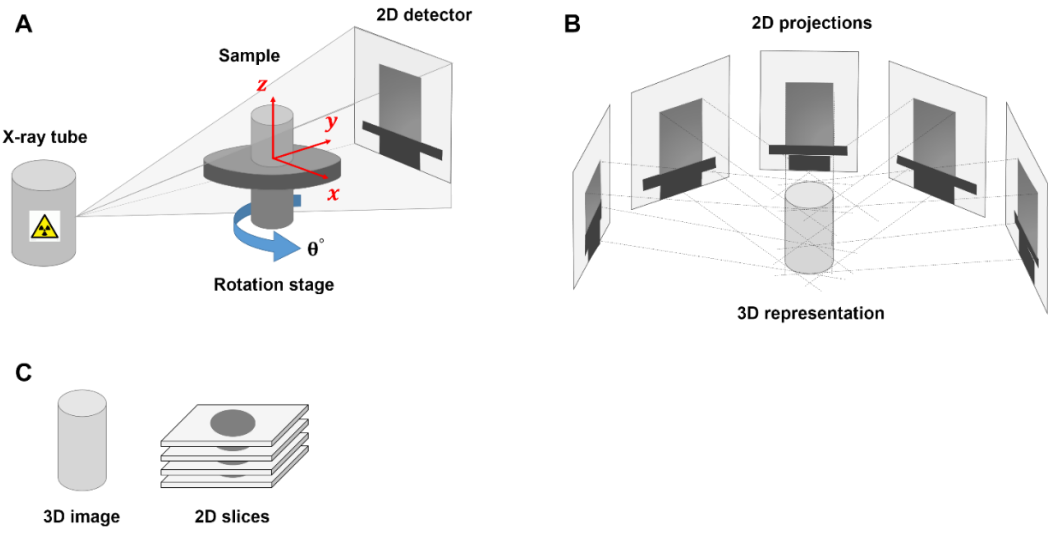

Figure 4-1. A: schematic diagram of the X-ray computed micro-tomography (XCT) apparatus and its co-ordinate system. B: digital reconstruction of 3D representation using the collected 2D projections. C: two main forms of presenting the 3D representation, left in its 3D form, right in 2D slices form. All is not drawn to scale.

on the y axis. The textile sample is mounted on the rotation stage and the stage rotates at a pre-set increment of $\Delta\theta°$ throughout a 360° rotation. While the stage is rotating, a set of 2D projections of the original sample are taken at different angles, as illustrated in figure 4-1B. These 2D projections are the raw output of the tomogram and are digitally reconstructed to form a 3D representation of the original sample, using the algorithms implemented in the manufacture's software. Then the reconstructed 3D representation is viewed in a virtual environment in a variety of ways, typically being viewed in its 3D form or 2D image slices, as illustrated in figure 4-1C, depending on the research purposes.

We used a 520 Versa X-ray microscope, from Carl Zeiss, USA, for the spreading studies. To prepare the samples, we cut the cotton textile into 5×5 mm^2 sections then vertically mounted them separately on standard XCT bins using adhesive. The vertical mounting of the samples allows us to disregard the gravitational effect during the spreading process. Subsequently we clamped the bin to the rotation stage. The textile sample is in the plane $x = 0$ and its interior structure is in the positive x direction (see the co-ordinate system in figure 4-1). μ_2 fluid was carefully manipulated using needles to form droplets (diameter~500 μm) and the droplets were transferred on to the surface of the textile sample.

To image the samples, we set the number of projections to 601, across a 360° sample rotation, to achieve a 2.6 μm isotropic voxel size. Each projection was collected using a 0.5 s exposure time. The obtained 2D projections were reconstructed to a 3D volume using a filtered back projection algorithm implemented in the manufacture's software. A standard Shepp-Logan filter, Gaussian filter (strength of 0.5), and beam hardening correction (strength of 0.05) were applied to the projections. The imaging conditions allowed the shortest imaging time while maintaining a microscopic spatial resolution. Determined by the pre-set number of projections, the scanning duration was 25 ± 4 minutes. So the 70 minute spread-through time would allow us to collect three tomography scans.

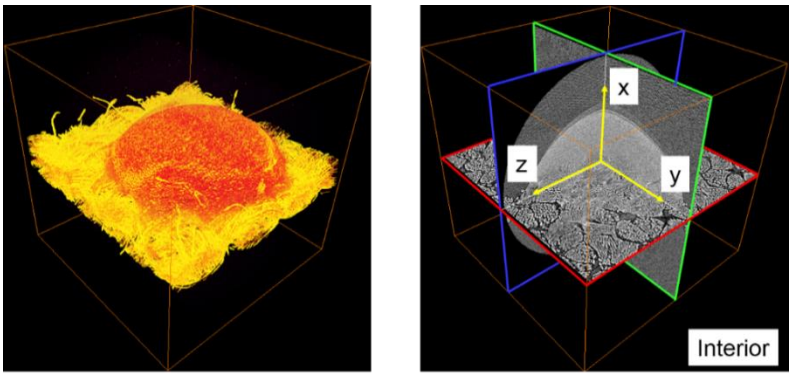

Figure 4-2. Left image: 3D XCT reconstruction of a droplet of μ_2 fluid on the surface of a cotton textile. Right image: the interior view of the left image.

We chose to view the reconstructed 3D representation in both 3D and 2D slice forms. An example 3D representation of an oil droplet sitting on our textile surface is shown in the left image of figure 4-2. Using the MRT mode, we are able to access the interior of the 3D representation via xz, xy and yz slices (see the right image of figure 4-2). In this chapter, we use the xz slices to show the local oil distribution in the textile thickness. To render the liquid distribution in the textile evident, we segmented the slices into liquid and textile (including background) phases using a machine learning-based segmentation tool (Weka, 3.9.0, ImageJ, U.S. National Institutes of Health, Bethesda, MD). By colouring the liquid, air and textile phase red, green and purple respectively, we are able to clearly visualise the time-evolved liquid distribution in the textile in the segmented slices. Additionally, the liquid phase is shown in black while the textile and air phases are shown in white for effective contrast when only the liquid phase needs to be presented. A Weka learning scheme, which is implemented in ImageJ, is used to classify the pixels of an xz image into textile, air or liquid[155]. Briefly, the Weka learning scheme applies filters, such as edge detectors (Laplacian and Sobel, Gabor, etc.) texture filters (minimum, maximum, median, entropy, etc.) and noise reduction filters (Gaussian, Kuwahara, Lipschitz, etc.) to an xz image to generate filtered images. The filtered images represent different image features and form an 'image pipeline'. Pixel samples were manually labelled in the original image and subsequently the labels applied to the corresponding pixels from the images in the pipeline. The pixel values were given ranges for the liquid, air and textile phase, which

were used as training sets to make classifiers. The application of the classifiers to the xz slices would classify the pixels automatically and present the liquid, air and textile phase in colours.

4.2.2 X-ray radiography

Radiography is used to view the interior of an object from only one angle. Using the same procedures in section 4.2.1, we mounted the textile sample on a bin and fixed the bin to the sample stage. Radiography images are obtained via X-ray bean transmission along the y axis and through the sample to the detector as indicated in figure 4-1, and they offer a superimposed view of all the xz planes along the y axis. Radiography enables real-time imaging of the liquid front motion within the textile. For our spreading studies, pixel size, number of projections, exposure time, and waiting time between projections were 1.296 μm, 1200, 4 s and 1 s, respectively.

The shift of the X-ray intensity profiles at successive times shows the displacement of the spatially averaged advancing liquid front in the textile in the x direction. To compute the displacement, intensity threshold values 115, 120, 122, 125, and 126 were selected. For each threshold value, the displacement Δx_L is calculated using: $\Delta x_L = x_t - x_0$, where x_t is the coordinate of the advancing liquid front at t and x_0 is the initial coordinate of the liquid front at $t = 0$ s.

4.3 Results and discussion

4.3.1 Textile structure

Figure 4-3 illustrates the main geometric features of our textile. The textile is characterised by an ordered multi-scale structure. The basic component is yarn (diameter ~ 100 μm), which are formed by bundles of fibres (~ 5 μm) twisted about yarn's central axis. The textile is formed by disposing yarns in a mesh-like arrangement. In the following discussion, we denote the smallest pores of the textile as 'inter-fibre interstices' and the largest pores thereof (linear dimension ~ 100 μm) as 'inter-yarn pores'.

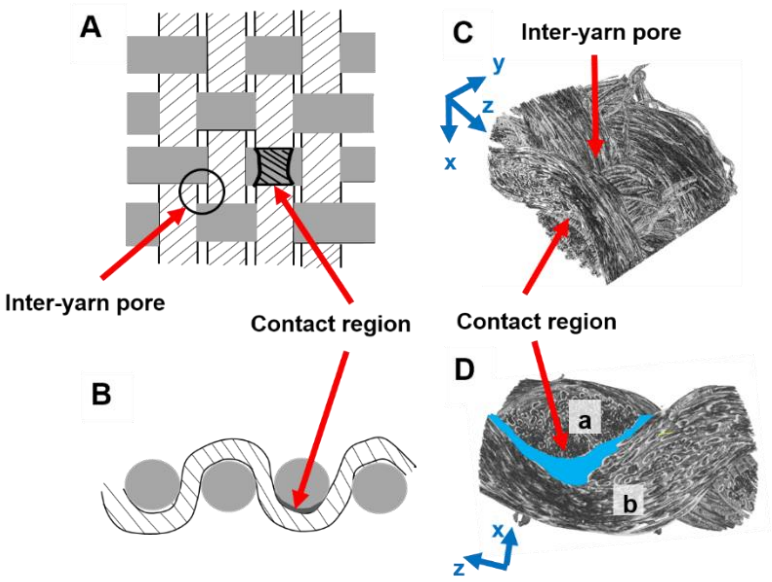

Figure 4-3. Schematics (A, B) and XCT images (C, D) illustrating the structure of the textile

The central line of any z-yarn (a yarn parallel to the z axis) in the xz view is approximately sinusoidal (figure 4-3B and 4-3C). Typically a z-yarn first passes below (or above) a y-yarn and passes above (or below) the next y-yarn (figure 4-3B). This arrangement yields a saddle-shaped contact region, whose projection on the yz plane is indicated in figure 4-3A by a dark dashed region. Because of the irregular surface of the yarn, the contact region has a finite maximum thickness of roughly 10 μm (which in turn is of the order of the fibre diameter). The inter-fibre interstices have a typical diameter of about 3 μm. This is smaller than the fibre diameter. We have examined the diameters of the capillary pores and of the fibres in the XCT images by averaging over 15 fibres for each reported diameter value.

4.3.2 Mechanism of transplanar liquid spreading

Figure 4-4 shows front (yz) and side (xz) views of the droplet outside the textile. The droplet spreads laterally in the yz plane while simultaneously penetrating in the x direction. The motion of the air-liquid-solid contact line is relatively slow, and is hindered by the large out-of-plane roughness of the textile (which results from the wavy shape of the yarns) and by the fibres that extend out of plane. Some out-of-plane fibres pierced the droplet. The fibres

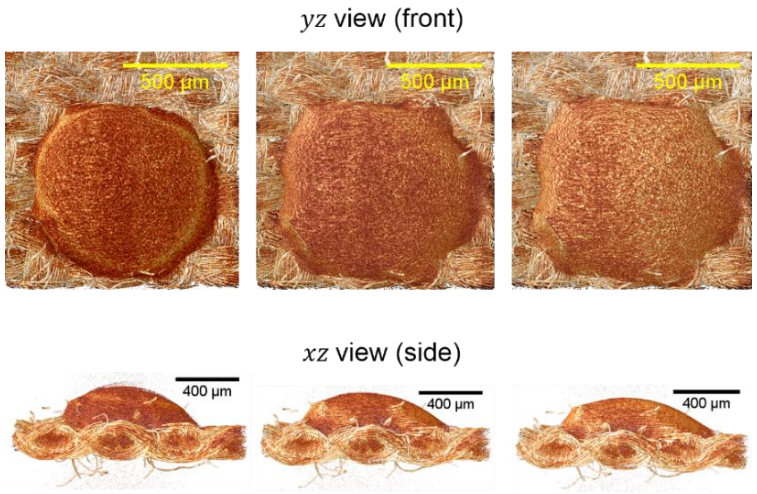

Figure 4-4. Time evolution of the topological change of a droplet of μ_2 fluid on the surface of the textile in XCT images. Both rows from left to right: $t = 25$ min, $t = 45$ min and $t = 70$ min, respectively.

constitute unavoidable structural features that are due to the rupture of fibre bundles. The rupture is a result of either the weaving process or the repeated manual handling of the textile sample. The front view in figure 4-4 shows that the droplet shape projected on to the yz plane is approximately circular at $t = 25$ min. At later times the projection of the contact line on to the yz plane tends to be polygonal. The feature is likely a result of the triple line conforming to the regular microstructure of the textile, as suggested by studies of droplet spreading on micro-fabricated surfaces formed by regular arrays of pillars[156].

Figure 4-5 shows side (xz) views of the μ_2 fluid within the textile, focusing on the inter-yarn pore region. To render the distribution of the liquid evident, Weka segmentation (section 4.2.1) was used to associate colours to the liquid, air and solid phases. At $t = 25$ minutes, the inter-yarn pore is filled with liquid for $\frac{3}{4}$ of its depth. In the remaining 45 minutes, the motion of the liquid-air interface in the inter-yarn pore region is negligible. The dynamics for $t < 25$ min is not accessible due to the experimental requirement of 25 minutes to complete one tomography scan. If the largest pores were modelled as circular channels of uniform cross-sectional radius R and depth h, capillary penetration would require a time $T \sim \frac{2h^2}{R}\frac{\mu}{\sigma cos\theta_Y}$ of the order of a few minutes. For example, $T \approx$

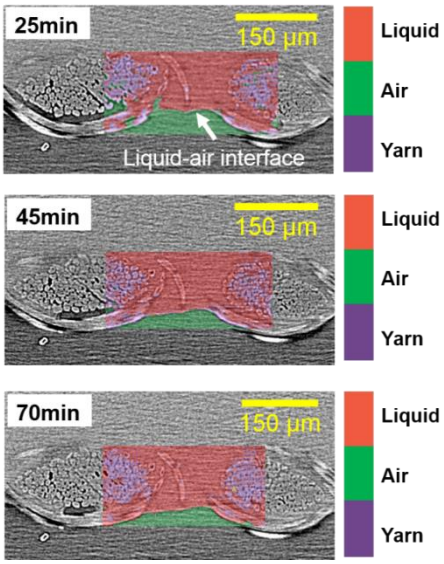

Figure 4-5. Time evolution of μ_2 fluid distribution in an inter-yarn pore of the textile shown in xz view.

5 minutes, assuming $h \approx 250$ μm, $R \approx 50$ μm, $\mu_2 \approx 2.4 \cdot 10^3$ Pa·s, $cos\theta_Y \approx 1$, $\sigma \approx 20$ mN/m. The slow motion of the liquid-vapour interface in figure 4-5 could be due to the presence of a capillary channel having a complex geometry.

Figure 4-6 shows the detail of a contact region between two different yarns. After filling the inter-yarn pores, the liquid appears to slowly creep in the relatively wide channel offered by the contact region. Because each contact region is inter-connected by several inter-yarn pores, the liquid is transported into each contact region from several inter-yarn pores simultaneously. Examination of other images show that the filling behaviour illustrated in figure 4-6 occurs frequently.

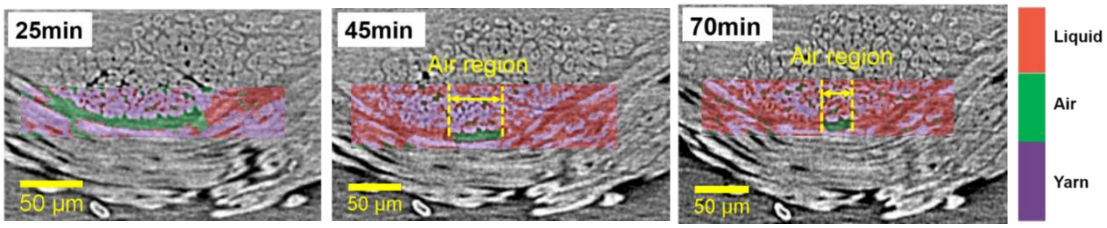

Figure 4-6. Time evolution of μ_2 fluid filling a contact region of the textile in xz view.

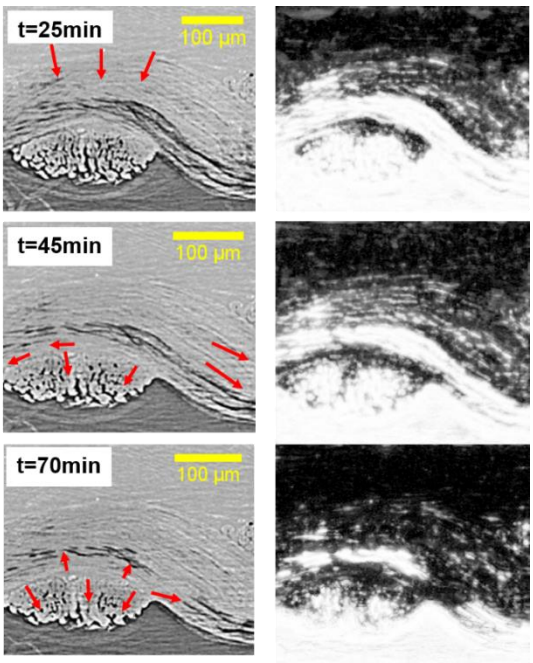

Figure 4-7. Left: Time evolution of μ_2 fluid distribution in the neighbourhood of a contact region in xz view. Arrows indicate the approximate direction of the liquid flow. Right: corresponding segmented images, only showing the liquid in dark colour.

The contact region is a relatively low-permeability path through which the liquid from the pores reaches the interior of the yarns. The side (xz) view in figure 4-7 shows two yarns, one parallel and one perpendicular to the page. The top portion of the yarn parallel to the page is in contact with the droplet. Most of the yarn perpendicular to the page appears to be dry. At $t = 25$ min, the contact region is only partially filled with liquid. As time progresses, the contact region is progressively being replenished with liquid. From the contact region, the liquid is then transported into the interior of the yarns. Liquid is also transported directly from the drop to the interior of the yarns. The reduction in the extent of the dry regions within each yarn is particularly evident in the segmented images of figure 4-7 (right column).

Considered collectively, Figures 4-5, 4-6 and 4-7 suggest a multi-stage transport mechanism, as illustrated in figure 4-8. In the first stage of liquid penetration, which we term pore penetration, the liquid is transported through the relatively large inter-yarn pores. During the pore penetration stage, some

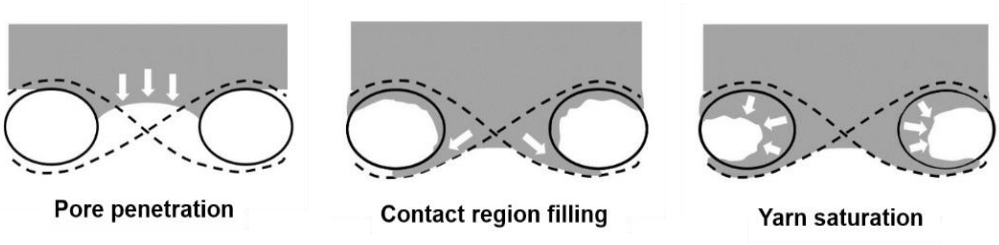

Figure 4-8. Three-stage mechanism of liquid spreading through a single-layer textile

liquid also penetrates in the yarns that are directly in contact with the droplet. In the second stage (contact region filling) the liquid is transported mostly in the direction parallel to the plane of the textile through the channels corresponding to the regions of contact between the yarns. In the third stage (yarn saturation) the liquid slowly wicks towards the interior of the yarns flowing from the contact region and from the interior surfaces of the inter-yarn pores. In the case of the yarns that are in contact with the drop, the liquid originating from the contact region meets the liquid from the droplet until the yarn becomes fully saturated.

4.3.3 2D liquid distribution in the textile thickness

While the liquid distribution is three-dimensional, information about the volume-averaged saturation distribution is often useful. Theoretical analyses

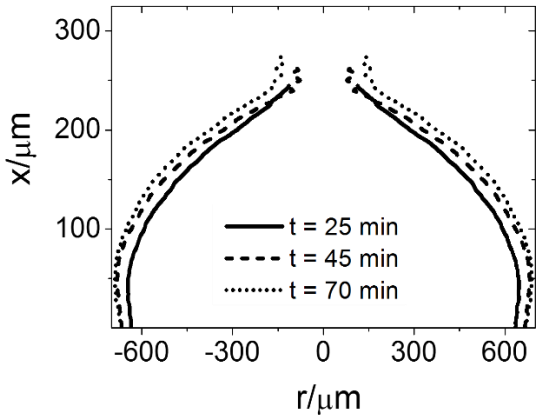

Figure 4-9. Radius of the wetted region as a function of the x co-ordinates, for μ_2 fluid.

typically describe continuum volume-averaged fields. The theoretical model of Patnaik et al[150], for example, assumes that transverse penetration occurs uniformly under the droplet, and that the liquid front is planar. In contrast, the model of Starov et al.[157] assumes that the advancing liquid front in the material has a hemispherical shape with an increasing radius. Figure 4-9 shows the shape of the region saturated with liquid as an $r - x$ curve. For any given value of x, r is calculated as $r = \sqrt{\frac{A(x)}{\pi}}$, where $A(x)$ is the area of the wetted region at x. The shape reported in figure 4-9 is thus the high-saturation distribution averaged over the azimuthal angle. To calculate $A(x)$ we applied trainable Weka Segmentation to every yz slice and computed the area of the liquid region.

The shape of the azimuthally-averaged high-saturation region in figure 4-9 resembles half an hour-glass. The high-saturation region below the droplet is approximately hemispherical. The back of the textile is connected with the hemispherical region through a neck of initial radius ≈ 100 μm. As time proceeds, the radius of the neck increases, and the boundary of the hemispherical region shifts towards the back surface. In the region of minimal slope of the $x - r$ curve, corresponding to $r \approx 350$ μm, the displacement of the boundary between $t = 25$ minutes and $t = 45$ minutes is larger than between $t = 45$ minutes and $t = 70$ minutes, suggesting a slowing down of the average rate of liquid penetration.

4.3.4 2D kinetics of transplanar liquid spreading

The time evolution of the liquid distribution in a textile shown in xz views of figure 4-10 provides a qualitative understanding on the transplanar permeation process. We saw that the curved droplet profile on the upper surface of the textile gradually flattened over time and eventually disappeared due to the sinking of the droplet into the textile. We noticed that the lower surface of the textile became darker and blurrier gradually. The blurriness implied that a portion of the droplet slowly reached the lower surface and started wetting it.

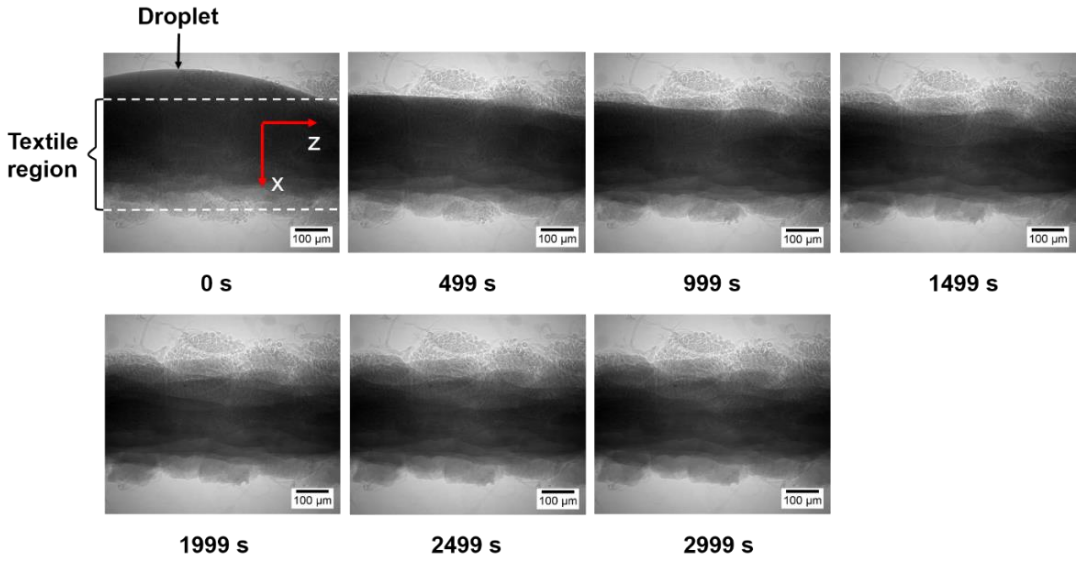

Figure 4-10. Radiography image sequences showing the liquid front movement in the x direction towards the interior of the textile for μ_1 fluid. The textile is in the region between the two white dash lines, the red arrows indicate the x and z axes, the y axis is pointing perpendicularly into the page.

In contrast, in the middle portion of the textile region, we were unable to see significant visual difference among the presented images.

To understand the process of the droplet spreading through the textile, in figure 4-11A, we plotted the X-ray intensity I as a function of the x coordinates for all the images of figure 4-10. We noticed that all the curves in figure 4-11A conformed to a slightly distorted "U" shape. This "U" shape is due to the fact that in the 'textile and liquid' region large portions of the X-ray photons are absorbed by the materials, consequently the intensity I dropped to a "valley".

It has been well known that I follows the relationship: $I = I_0 \exp(-\mu_m \rho y)$, where I_0 is the initial X-ray intensity before the X-ray beam penetrates the sample, μ_m is the mass absorption coefficient and is proportional to the concentration of liquid, ρ is the liquid density and y is the distance that the X-ray beam penetrates in the material. The intensity I therefore inversely correlated to the concentration of liquid. For any given value of x the corresponding X-ray intensity characterises the area-averaged liquid concentration distribution in the corresponding yz plane. The high liquid

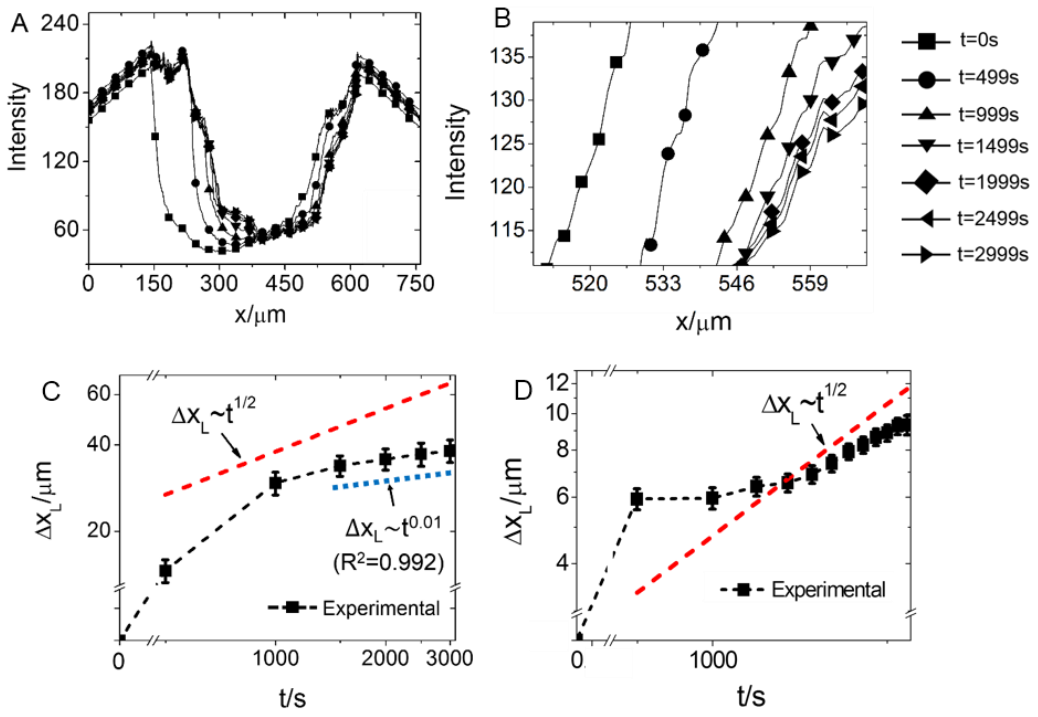

Figure 4-11. A: X-ray intensity curves as a function of the x co-ordinates for successive times, for μ_1 fluid. B: Zoom in the region $511 \leq x \leq 567$ of A. C: Log-log plot of the liquid front displacement in the x direction as a function of time, for μ_1 fluid. D: Same as C for μ_2 fluid.

saturation region within the textile corresponds to the range from $x \approx 400$ μm to 700 μm roughly. The range $150 < x < 400$ μm approximately corresponds to the portion of the droplet outside the textile. The area-averaged position of the liquid-vapour interface corresponds to the region of largest intensity gradient near the back of the textiles and an enlarged view of this region is provided in figure 4-11B.

We measure the motion of the high-gradient region corresponding to the liquid meniscus by calculating the shift in the x direction of the intensity profiles (see Materials and Methods section). The shift Δx_L of the average x co-ordinate of the liquid-vapour interface with respect to the front initial position is plotted in log-log scale against time for μ_1 fluid in figure 4-11C and for μ_2 fluid in figure 4-11D, respectively. The data in figure 4-11C and 4-11D characterise the one-dimensional kinetics when the liquid-air interface is close to the back of the textile. The instants immediately following the deposition of the drop

were inaccessible owing to the time needed to place the sample in the X-ray chamber and to reach a stable X-ray source intensity.

For both the smaller and larger viscosity liquids, a single scaling does not fit the experimental data. For example, for μ_1 fluid, the slope of the $\Delta x_L - t$ curve is smaller than 0.5 (the value predicted by the Lucas-Washburn law) for $t > 1000$ s roughly. A fit to the data for the largest times gives $\Delta x_L \sim t^{0.01}$. However this asymptotic rate of $\Delta x_L \sim t^{0.01}$ will not describe the experimental data for μ_2 fluid. The quantitative differences between the two viscosities might be due to differences in observation window. Assuming that the penetration rate is inversely proportional to the viscosity, the features corresponding to $t = 1000$ s in figure 4-11C would correspond to $t = 24700$ s in figure 4-11D, while our observation window for μ_2 fluid extends only to $t = 6000$ s.

A single scaling would be expected if: i) entrance effects associated with the small length of the capillary channels did not alter the dynamics of the liquid penetration process and ii) the liquid transport was governed by a single transport law for any value of t. Continuum theories for liquid transport in porous media, such as the Lucas-Washburn theory[32] or variations of it[158-159], are derived under the assumption that the porous medium can be modelled as a collection of parallel channels having length $L \gg R$, where R is the average pore radius. By contrast, in our case, even the largest pores, that control the initial motion of the liquid have an aspect ratio close to 1.

Staples and Shaffer[160] examined the law of propagation of a liquid meniscus in a capillary tube of sinusoidal cross section. They proved that if the length of the capillary tube is much larger than the wavelength of the sinusoid, the predicted liquid meniscus position fluctuates around the curve predicted by the Lucas-Washburn law. This behaviour can be understood by considering the speed of propagation dL/dt of a meniscus in a circular channel of non-uniform cross sectional radius $R(z)$[160]:

$$\frac{dL}{dt} = \frac{1}{4}\frac{\sigma}{\mu}\frac{cos\theta}{[R(L)]^3}\frac{1}{I(L)} \tag{4.1}$$

where

$$I(L) = \int_0^L \frac{dz}{[R(z)]^4} \tag{4.2}$$

For $R = const.$, integration of equation (4.1) gives $L^2 = \frac{1}{2}\frac{\sigma}{\mu} cos\theta Rt$, which is the Lucas-Washburn equation. For a small sinusoidal perturbation to a constant radius channel, $R = R_0[1 - \varepsilon\, sin(\lambda z)]$ with $\varepsilon \ll 1$, equation (4.2) becomes:

$$I = \frac{L}{R_0^4} + 4\frac{\varepsilon}{R_0^4}\int_0^L sin\lambda z\, dz \tag{4.3}$$

For $L \gg \lambda$, the integral of the sine function has zero average, and the Lucas-Washburn law is recovered in a time-averaged sense. However, for $L \sim \lambda$, the solution of equation (4.1) gives a marked non-linear variation from the Lucas-Washburn law, whose features depend on the actual geometry of the pore[160]. This simple model illustrates that applying results for thick multi-layer textiles to single-layer textiles can give qualitatively and quantitatively incorrect results, and could explain the non-linear behaviour seen in figure 4-11C and 4-11D.

An important aspect that we believe could explain the slowdown observed in figure 4-11C and 4-11D is the change in dominant direction of liquid propagation as time progresses. Using the terminology introduced in the discussion of figure 4-7, in the pore filling stage the liquid is transported mainly in the x direction. However, in the contact region filling and yarn saturation stages the fluid is mostly transported in the lateral (in-plane) direction, contributing little to the x component of the average fluid velocity.

4.3.5 Measurements of $\theta_{Y\text{-}Micro}$ for textiles

When a static liquid droplet is deposited on the surface of a fibrous medium, the apparent contact angle θ_m indicates the wettability of medium. Using the meta-stable Cassie-Baxter equation[143, 146], one can predict the θ_m:

$$\cos\theta_m = \frac{R_f(\pi - \theta_Y)}{d_i + R_f}\cos\theta_Y + \frac{R_f}{d_i + R_f}\sin\theta_Y - 1 \tag{4.4}$$

In equation (4.4), R_f is the typical fibre radius, θ_Y is the intrinsic contact angle, $2d_i$ is the distance between adjacent fibres. The measurement of θ_Y is important to the correct prediction of equation (4.4).

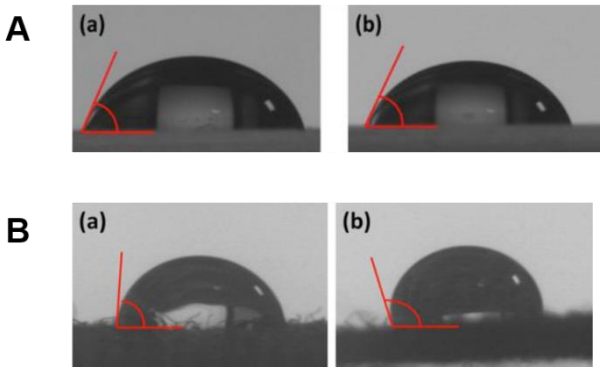

Figure 4-12. A. Droplet of silicone fluid (15 µl) placed on PFAC6 (a) and PFAC8 (b) glass slides, respectively. B: Same droplet on PFAC6 (a) and PFAC8 (b) textiles.

The classical wetting theory[161] defines θ_Y as the Young's contact angle. When a static droplet is placed on a flat surface made of the same material as the fibrous medium, at thermodynamic equilibrium θ_Y is the angle of the vector of the liquid-vapour interfacial tension with respect to the vector of the liquid-solid interfacial tension. On two flat surfaces made of the PFAC6 (figure 4-12A (a)) and PFAC8 (figure 4-12A (b)) polymers respectively, a silicone fluid droplet at equilibrium shows almost the same θ_Y. If the PFAC6 and PFAC8 polymers are applied to two identical textiles, according to equation (4.4), those textiles should have the same wettability. However, our observations shown in figure 4-12B showed different wettability for the PFAC6 and PFAC8 textiles.

A recent paper[146] on the prediction of θ_m for PFAC8 electrospun nano-fibre mats has re-defined the classical θ_Y. Figure 4-13C shows a silicone oil droplet attached to a nano-fibre of an electrospun fibre mat. θ_Y is the angle of the vector of the liquid-vapour interfacial tension with respect to the vector of the liquid-solid interfacial tension. According to the new definition, the $\theta_{Y-Micro}$ in our case should be the Young's contact angle of a droplet attached to a textile fibre.

For the measurement of the new $\theta_{Y-Micro}$, we used a low viscosity silicone fluid ($\mu \approx 5 \cdot 10^{-3}$ Pa·s). Using a regular spray gun, we sprayed micro-droplets of the fluid into the air. Driven by gravity the micro-droplets would land gently on the PFAC6 and PFAC8 textiles. After attaching the droplets, the PFAC6 and PFAC8 textiles are fixed to separate sample stages for tomography scans. The settings of the scans and the 3D reconstruction are written in section 4.2.1.

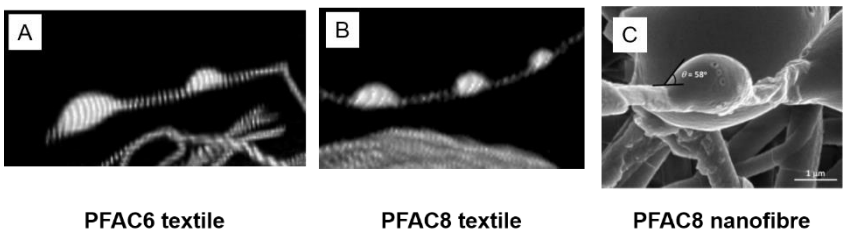

Figure 4-13. A. $\theta_{Y-micro}$ for PFAC6 textile. B. $\theta_{Y-micro}$ for PFAC8 textile. C. θ_{Y-Nano} for electrospun nanofibre. Image C is taken from Ref. 149.

Figure 4-13A and B show the attached micro-droplets on a PFAC6 and a PFAC8 textile fibre respectively. The sizes of the micro-droplets are non-uniform. For any micro-droplet examined a large portion of the droplet volume always appears on one side of the textile fibre. Occasionally a micro-droplet may surround a textile fiber, such as the largest droplet in figure 4-13A. The surrounding configuration is likely due to the effect of gravity on relatively large micro-droplets.

The measurements of $\theta_{Y-Micro}$ for the micro-droplets with different sizes are presented in figure 4-14. $\theta_{Y-Micro}$ is not significantly affected by the micro-droplet size. The average $\theta_{Y-Micro}$ for our PFAC6 and PFAC8 textiles are 50°±4° and 58°±5°, respectively.

For our textiles, R_f~4 μm, d_i~4 μm, $\theta_{Y-PFAC6} \approx 50°$ and $\theta_{Y-PFAC8} \approx 58°$. Using equation (4.4) we obtain θ_{m-C6}~80° for the PFAC6 textiles and θ_{m-C8}~92° for the PFAC8 textiles. The predicted θ_m here are in agreement with the observed textile wettability in figure 4-12B.

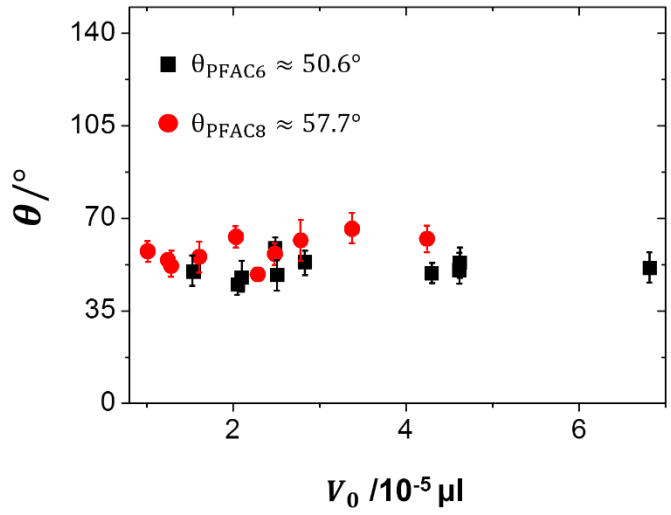

Figure 4-14. Young's contact angle measured by X-ray tomography on PFAC6 and PFAC8 textile fibres.

Figure 4-15 shows the prediction of θ_m as a function of the inter-fibre distance d_i, for the PFAC6 and the PFAC8 textile (R_f~4 µm, $\theta_{Y-PFAC6} \approx 50°$ and $\theta_{Y-PFAC8} \approx 58°$). A decrease of 1 µm for d_i could result in a decrease of 20° for θ_m for both textiles. This figure emphasises the importance of the textile yarn geometry to the textile wettability.

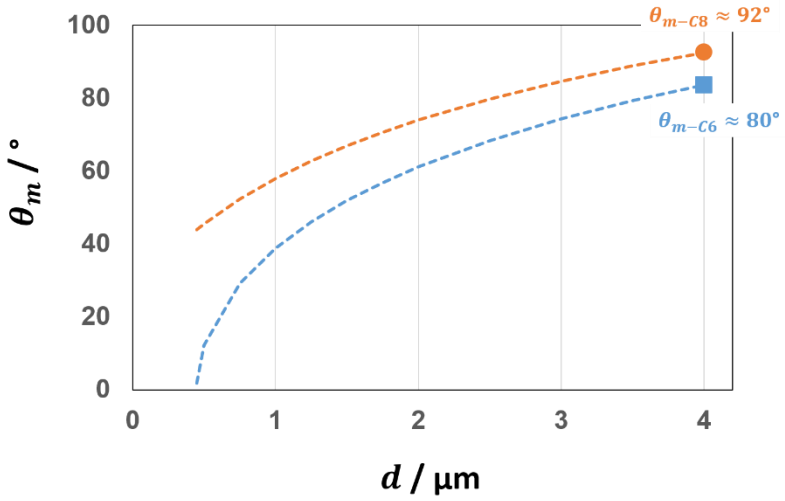

Figure 4-15. θ_m from equation (4.4) as a function of the inter-fibre spacing d_i. Our textile fibre radius $R_f \approx 4$ µm. The θ_m values corresponding to $d_i \approx 4$ µm are the predicted apparent contact angles for our PFAC6 and PFAC8 textiles.

4.3.6 Liquid wetting of textile interior

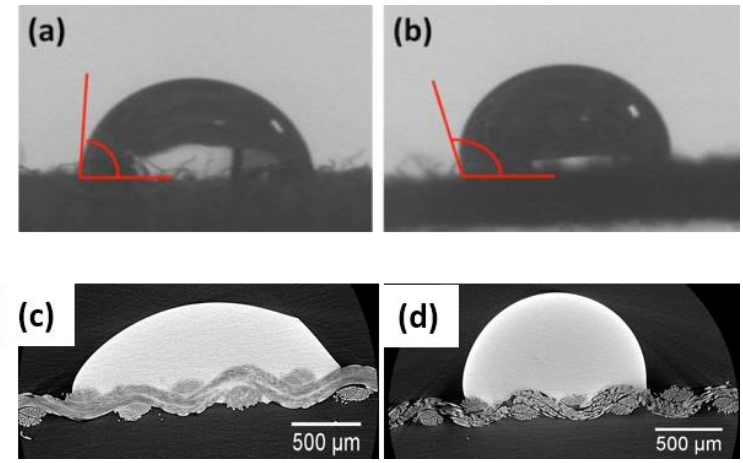

Figure 4-16. Droplet sitting on the PFAC6 (a) and PFAC8 (b) textile surfaces. (c) and (d) show liquid permeation situation in the textile thicknesses, corresponding to (a) and (b) respectively.

Because $\theta_{m-C6} < 90°$, when a silicone oil droplet is placed on the surface of a PFAC6 textile, a portion of the droplet should invade the interior of the textile. To provide experimental evidence, we placed oil droplets separately on a PFAC6 (figure 4-16(a)) and a PFAC8 (figure 4-16(b)) textile and showed the interior of the textiles in xz slices (figure 4-16(c) and (d)). In figure 4-16 (c) and (d), the oil is shown in bright, white colour and the air phase is shown in dark grey colour to aid the observation. For the horizontal yarn in figure 4-16(c), the inter-fibre interstices presented a similar colour as the oil phase, indicating the occurrence of the oil permeation in the interior of the horizontal yarn. In contrast, for the horizontal yarn in figure 4-16(d), the inter-fibre interstices presented a dark grey colour, indicating the absence of the oil.

4.4 Conclusions

We have examined by X-ray tomography and radiography imaging the time-dependent transport of ultra-high viscosity liquids in the transplanar (normal) direction following the deposition of a small droplet on the surface of a single-layer textile.

A key insight of our investigation is that the transverse liquid transport appears to proceed in stages, each stage being associated with a geometric feature of the fiber arrangement. The fast initial transport appears to be mainly associated to the fluid filling the large, inter-yarn pores. The late stages of penetration are associated to the slow impregnation of the interior of the yarns. In the intermediate stage where the liquid flows mostly through the region of contact between the yarns.

We have quantified the one-dimensional kinetics of liquid penetration by using X-ray radiography. The results show that a single power law does not capture all the data. The asymptotic transport rate is much smaller than that predicted by the Lucas-Washburn equation.

Models that consider single layer textiles as homogeneous and isotropic porous media have been applied to lateral, in-plane transport with some success[12, 151]. This success is likely due to the fact that in the lateral direction the asymptotic flow is to a first approximation independent of the microscopic geometry of the textile. In our case, the small thickness of the single layer textile can prevent an asymptotic flow behavior being established before the liquid reaches the back surface of the textile. This feature could explain the strong deviations from a power law behavior seen in figure 4-11C and 4-11D.

In addition, to aid the development of theoretical models, our results may have implications for the development of strategies to manipulate liquid transport in textiles. For example, the XCT images suggest that the initial liquid mass flux is governed by transport in the relatively large inter-yarn pores. Altering these features, for instance by utilising nano-particles to partially change the local surface roughness of the walls of the pores, could represent an approach to tailor the liquid transport rates in the transplanar direction.

When using the meta-stable Cassie-Baxter equation (equation 4.4) to predict the surface wettability of a textile, θ_Y should not be mistaken for the classical Young's contact angle. By attaching a micro-droplet to a textile fibre, we showed that the re-defined $\theta_{Y-Micro}$ is the angle of the vector of the liquid-vapour interfacial tension with respect to the vector of the liquid-solid interfacial tension. We placed liquid droplets on the surfaces of a PFAC6 and PFAC8

textiles separately. With the measurements of the re-defined $\theta_{Y-Micro}$, we could correctly predict the surface wettability of the PFAC6 and PFAC8 textiles, using equation (4.4).

5 High-speed imaging of droplet impact on a textile

5.1 Introduction

The impact of liquid droplets on solid surfaces is ubiquitous in nature, such as the raindrop impact on the surfaces of soil[162] and plants[64]. In industrial environments these impact dynamics are important in a wide range of applications, such as the design of functional surfaces for self-cleaning[54-55], ice repulsion[56-57], and the manufacturing of smart[58] and protective[1] clothing. In the past researchers have extensively studied droplet spreading and receding[59], bouncing and splashing[60-62] on smooth and rough solid surfaces and on complex and smart substrates[65]. Symmetric droplet splitting[63-64] and pancake bouncing[65] have been observed on solid surfaces with superhydrophobic ridges and micro-posts. More recently some authors have studied the impact of droplets on a sieve[106], and on rigid metallic meshes[38,110], concluding that the impact dynamics on the substrates depends on the impact speed and the substrate characteristics. However, the impact of droplets on textiles has received little attention. Previous studies have been confined to the qualitative comparison of blood stain patterns following the impact of blood drops on different textiles[13], and the estimation of the textiles' impact stresses[15]. Here we study the impact dynamics of liquid droplets on hydrophobic and hydrophilic nylon textiles. We first focus on the droplet spreading behaviour and next we determine the liquid penetration criteria in terms of the textile characteristics.

Various studies of the impact of droplets on porous substrates and meshes have been carried out in recent years focusing on the impact speed threshold for the droplet capture and penetration of a hole in a solid substrate[106], the droplet penetration speed in terms of the pore size of porous films[38], and the droplet contact time on metallic meshes[110]. In this chapter we study the radial spreading following the droplet impact on textiles and develop scaling arguments to obtain the penetration speed threshold in terms of the droplet diameters and textile geometry.

5.2 Material and methods

5.2.1 Fluid properties

In this chapter we study the impact of aqueous glycerol droplets on textiles. The working fluid is a solution of distilled water and pure glycerol (Sigma-Aldrich, assay of purity≥99.5%, UK) having a glycerol weight percentage of 56% with a measured fluid-vapour interfacial tension of $\sigma \approx 68.5 \pm 1.5$ mN/m and a dynamic viscosity $\mu \approx (6 \pm 1) \cdot 10^{-3}$ Pa·s at the room temperature $T \approx 23 \pm 3$ ℃.

The use of aqueous glycerol rather than pure water is for the prevention of anisotropic droplet impact. The isotropy of the impact is particularly important for high-speed imaging because only a set of 2-dimensional (2D) images can be obtained via this imaging technique. The impact dynamics interpreted from the 2D images can represent the dynamics of other dimensions only if the impact is isotropic. Droplets of pure water produced by our droplet generator often oscillate in random directions and the oscillation is a reason for the anisotropy of the impact. Whereas droplets of aqueous glycerol, whose dynamic viscosity is slightly higher than that of water, remain spherical prior to the impact. Under the assumption of non-chemical reaction between the droplet and the textile surface, we believe that the impact dynamics of the aqueous glycerol is universal for the impact of other non-wetting liquids with low viscosity.

5.2.2 Deposition of fluorinated coatings

Fluorinated coatings based on 1H,1H,2H,2H perfluorooctyl acrylate (PFAC6) and 1H,1H,2H,2H perfluorodecyl acrylate (PFAC8) are deposited on the surfaces of our nylon textiles via plasma treatment. The plasma treatment is a plasma-catalysed polymerisation process and the treatment procedure from Ref.[163] were used for the coating deposition. In brief, first of all the textiles are washed and dried thoroughly and placed in a plasma chamber. Tubes of PFAC8-monomer ($C_8F_{17}CH_2CH_2OCOCH=CH_2$) are connected to the chamber and subsequently the chamber is evacuated to a base pressure of about 1.33 Pa [1]. The monomer gas is released to the chamber at the base pressure and the plasma treatment is initiated and controlled by a pre-determined plasma

on-off cycle[1]. For the synthesis of PFAC6 and PFAC8, different numbers of the on-off cycle were used. In the final product pure PFAC6 or PFAC8 polymer should not be expected but a mixture of PFAC6 and PFAC8 should be. The PFAC6 (PFAC8) coating here refers to a coating containing PFAC6 (PFAC8) polymer at a dominant ratio. For the synthesis of PFAC6 (PFAC8) a relatively low (high) number of on-off circle was used.

5.2.3 High-speed shadowgraphy

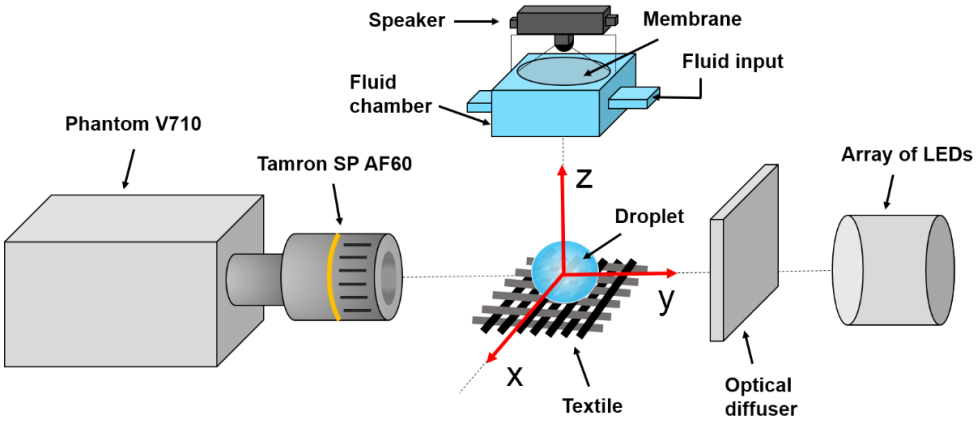

Figure 5-1. Schematic diagram of the high-speed imaging setup and the co-ordinate system used for the discussion of the results

After the plasma treatment the textiles were cut into 20×8 mm^2 sections. Each sample was fixed in the plane $z = 0$ with a Deben Microtest device (Microtest 200 N tensile stage, Deben, UK) as illustrated in figure 5-1. For the minimisation of the z-deformation, the sample was stretched with a force of 3.5 ± 0.1 N. Due to the high Young's modulus of the nylon textile (order of 1 GPa), we expect no alteration of pore size during the stretching.

A satellite-free millimetric droplet generator[164-165] was employed for the production of liquid droplets. As illustrated in figure 5-1 the droplet generator consists of a loudspeaker and a liquid chamber with a millimetre-sized nozzle at the bottom (nozzle diameter ≈ 2.0 ± 0.05 mm). The axis of symmetry of the nozzle coincided with that of the textile sample below. Through the loudspeaker fast and short single pulses generated by a pulse generator (8012B 50MHz pulse generator, UK) were sent to the fluid chamber for the generation of single droplets at the nozzle. A range of droplet velocities from

0.88 to 1.9 m/s can be achieved through the adjustment of the pulse width and amplitude. The droplet impact on the textile surface was recorded with a shadowgraphy system consisting of a high-speed camera (Phantom V710 with a Tamron SPAF60 macro lens), an optical diffuser and a high-intensity illumination (an array of LEDs), as illustrated in figure 5-1. The exposure was set to 15.62 μs and the frame rate to $6.4 \cdot 10^4$ fps. The inter-frame time interval was 0 μs. The recorded images were analysed with ImageJ and Matlab for the extraction of the impact velocity U_i and the droplet diameter D. In brief U_i was calculated from the examination of the z co-ordinates of the droplet geometric centre in a series of images. D was the averaged droplet diameter over 50 measurements in an image.

The position of the liquid meniscus at the nozzle is crucial to the achievement of a normal impact (z-impact). The meniscus position is adjusted through the vertical movement of the fluid tube of figure 5-2. The ideal meniscus position is achieved with the laser beam-calibrated planar alignment of the menisci A and B in figure 5-2.

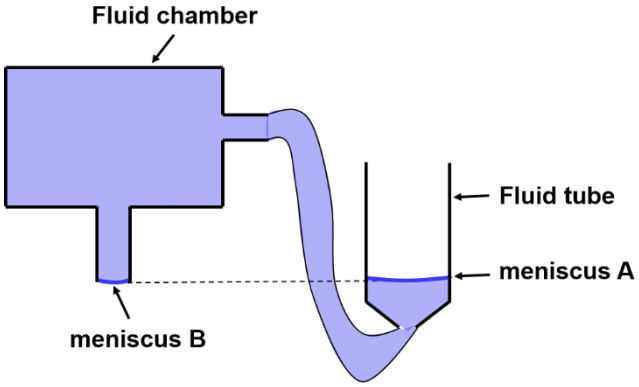

Figure 5-2. A detailed illustration of the fluid chamber and the fluid tube (fluid input in figure 5-1) showing the perfect meniscus position.

In the ideal meniscus position, the droplet generator occasionally ejects droplets at an angle $\Delta\theta \approx 0.05°$ with respect to the z axis[166] due to defects in the design of the droplet generator or disturbance from the environment. The angle may cause a droplet position shift of Δx_s at the moment of impact. In our experiments, given the nozzle-to-textile distance ~10 cm, $\Delta x_s = 10 \cdot 10^4 \cdot$

$\tan 0.05° \approx 87.3$ μm. This Δx_s is about 3 times of the measurement error and the impact with this shift was not analysed in this work.

5.3 Results and discussion

5.3.1 Textile geometric features

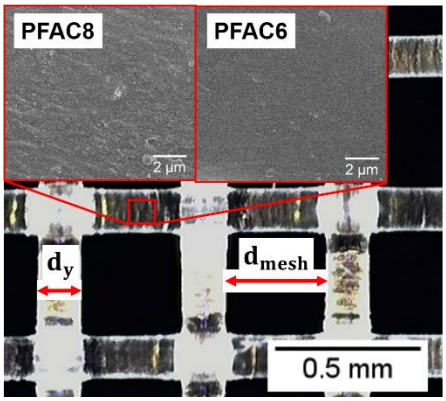

Nylon meshes (unit: μm)

No.	d_{mesh}	d_y	Δ	Φ
N-112	101.2	80.3	160.5	66.0%
N-180	168.3	74.3	148.5	49.9%
N-200	202.8	104.0	208.0	56.7%
N-300	301.5	95.1	190.1	42.4%

Figure 5-3. (Left) optical microscopy image showing the geometry of a nylon textile, the upper insets show SEM images showing the surface topography introduced by PFAC6 and PFAC8 coatings. The scale bars in the SEM images correspond to 2 μm. (Right) table of pore size (d_{mesh}), yarn diameter (d_y) and mesh thickness (Δ) and solid fraction ($\phi = \frac{d_y}{d_y + d_m}$) for all the textiles used in this study. The measurement error is ±1.5 μm. All parameters are measured directly from the optical images.

The nylon textiles (the optical image of figure 5-3) used in our experiments can represent many other textiles with the same 'woven' architecture. Horizontal yarns alternately pass below and above vertical yarns and form a mesh-like porous structure. The square black voids are referred to as 'textile pores' and the side length of a void, indicated by a red arrow, is referred to as the 'pore size' d_{mesh} throughout the chapter. The two SEM images show the PFAC6 and PFAC8 coated textile yarn surfaces, respectively. The relatively rough PFAC8 yarn surface provides a small contact angle hysteresis[125] and the effect of the small hysteresis on the impact dynamics will be discussed later on. The thicknesses of the coatings are reported to be on the submicron scale, therefore, no significant change of the textile geometry shall be expected from the coatings.

5.3.2 Dynamics of liquid lateral spreading

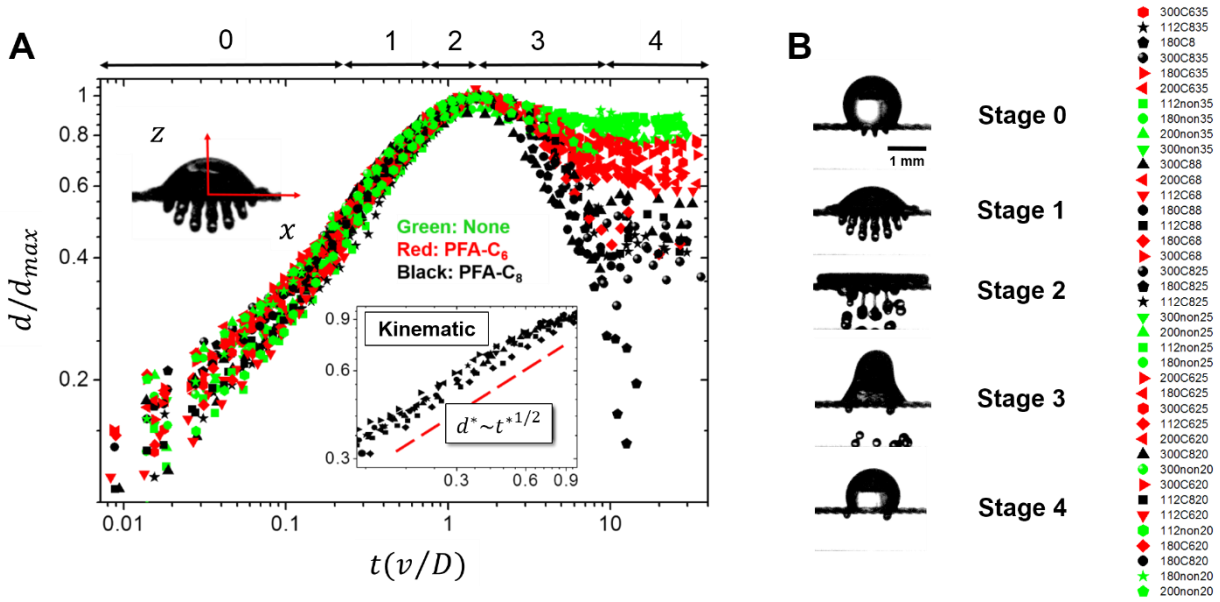

Figure 5-4. A: droplet spreading and receding diameters as a function of $t^* = t(U_i/D)$ for different We numbers and various textiles with pores ranging from 100-300 μm. The colours indicate different textile coatings: green for non-coated, red for PFAC6 coated, and black for PFAC8 coated textiles. The inset shows the scaling $d^*\sim t^{*1/2}$ characteristic of the kinematic stage. All data included. Measurement error ±30 μm. B: Typical droplet topology corresponding to each stages, the scale bar represents 1 mm.

For the interpretation of the liquid lateral spreading dynamics on the textile surface, the time evolution of the spreading diameter d is shown in figure 5-4A in the normalised form $d^* = \frac{d}{d_{max}}$, d_{max} is the maximum spreading diameter. The spreading time t is also in the normalised form $t^* = t(\frac{U_i}{D})$. With the simple relationship $d_{max}\sim D \cdot We^{\frac{1}{4}}$ [78], for an impact at a given We, our d^* has no difference to the well-known spread factor $\frac{d}{D}$ [167]. The good collapse of the data points for $d^* \leq 1$ shows a uniform dynamics of liquid spreading on textiles having varying pore sizes and surface wettability. From $d^* = 1$ the curve became three 'threads' and showed three receding dynamics on the basis of the surface wettability difference. The receding rate was determined by the energy dissipation of the order of $\sigma(\cos\theta_{rec} - \cos\theta_{adv})\frac{(1+\cos\theta_{adv})^2}{(1+\cos\theta_{rec})^2-(1+\cos\theta_{adv})^2}$

[168] and the subscripts 'adv' and 'rec' indicate the advancing and the receding contact angle. Since both PFAC6 and PFAC8 coatings have rather similar θ_{adv}, the PFAC8 coating would offer less energy dissipation due to the higher θ_{rec}. Consequently, the data for the PFAC8 textiles demonstrated a more rapid receding rate and a smaller equilibrium spreading diameter.

The lateral spreading can be divided into 5 stages (figure 5-4A) and each stage is represented by a characteristic droplet configuration shown in figure 5-4B. Stage 0 is termed 'penetration' whose characteristic impact picture is the formation of liquid filaments under the textile and the absence of droplet shape alteration. 'Penetration' is followed by 'kinematic' (stage 1). d^* in the kinematic stage varies linearly with $(t^*)^{\frac{1}{2}}$. The spreading is initiated by the formation of a liquid lamella at the droplet base and characterised by the fast expansion of the lamella and the flattening of the droplet volume above the lamella. In 'spreading' (stage 2), the spreading continues but the spreading kinetics conforms no longer to $d^* \sim (t^*)^{1/2}$. At $d^* \approx 1$ the droplet volume shape turns into a 'pancake'. Subsequently the receding (stage 3) of the 'pancake' commences under the effect of the surface tension and the receding dynamics is affected by the contact angle hysteresis[90]. The 'equilibrium' (stage 4) is characterised by the z-oscillation of the droplet and the formation of the equilibrium wetting configuration on large timescales.

5.3.3 .Liquid penetration dynamics for stage 0

Stage 1-4 were identified by previous related work of droplet impact on impenetrable substrates[167] whereas stage 0 is unique for impact on porous media. For the comparison of droplet shapes in $t^* < 0.3$, we present droplet impact on a flat impenetrable substrate and that on a textile in figure 5-5. Here no formation of liquid lamella was shown during the penetration stage in the case of textiles. Moreover, very little lateral distortion of the droplet shape could be seen during the penetration process.

Figure 5-5 could also provide some insights on the identity of the penetration driving pressure. It is known that droplet impact on impermeable solids[16, 66] and on some micro-textured substrates[111] results in a temporary liquid

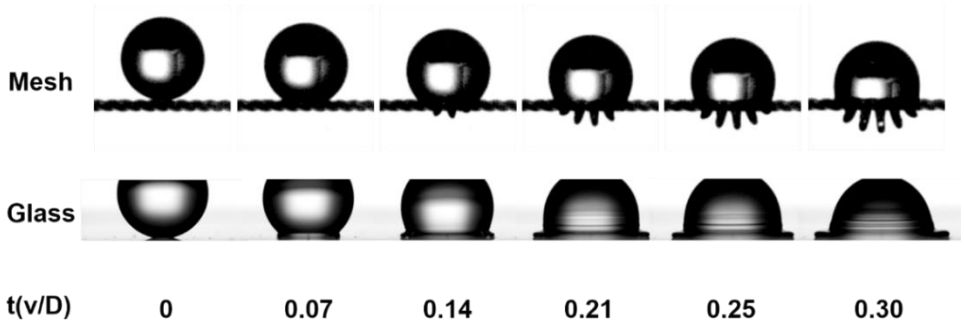

Figure 5-5. Image sequences comparing the impact of a droplet ($D \approx 1.56$ mm) on an N-300 textile at $We \approx 36$ and on a liquid-repellent glass slide at $We \approx 40$ for the illustration of the effect of substrate permeability on the droplet deformation. Both the glass substrate and the textile are coated with PFAC6.

compression at the droplet bottom and the compression generates a high pressure field $P(t)$ of the order[16] of $P(t) \sim \rho v^2 (\frac{D}{2vt})^{1/2}$. Because the impact force typically reaches the maximum[75] at $t_{max} \approx D/8v$, the peak pressure[16] due to the compression is of a magnitude of $P(t_{max}) \approx 2\rho v^2$. This peak pressure was often referred to as 'water hammer' pressure P_{WH} and had been considered as the driving pressure of the liquid penetration following the droplet impact on non-wettable microtextured surfaces[111] and microgrids[112]. Recently for the droplet impact on non-wettable copper meshes, P_{WH} was found to scale as $k\rho v^2$ with the scaling constant k having some dependence on the mesh pore size. Moreover, Ref.[111] proposed a two-stage mechanism for the early-stage penetration. The first stage is the generation of P_{WH} due to the temporary volume compression at the droplet bottom and the second stage is the release of P_{WH} via simultaneous lateral droplet spreading and vertical penetration through the pores. However, in our experiments we believe that the high porosity of the textile permitted almost immediate droplet penetration and consequently the build-up pressure should be much lower than the reported P_{WH}. We can show that the penetration was almost 'immediate' with the following simple estimation: in the mesh image sequence of figure 5-5, given $U_i \approx 1.78$ m/s and $D \approx 1.56$ mm, the time for the formation of primary liquid filaments under the textile (the 3rd image) was approximately $t \approx 0.12$ ms, the droplet travelling time across the textile thickness was approximately

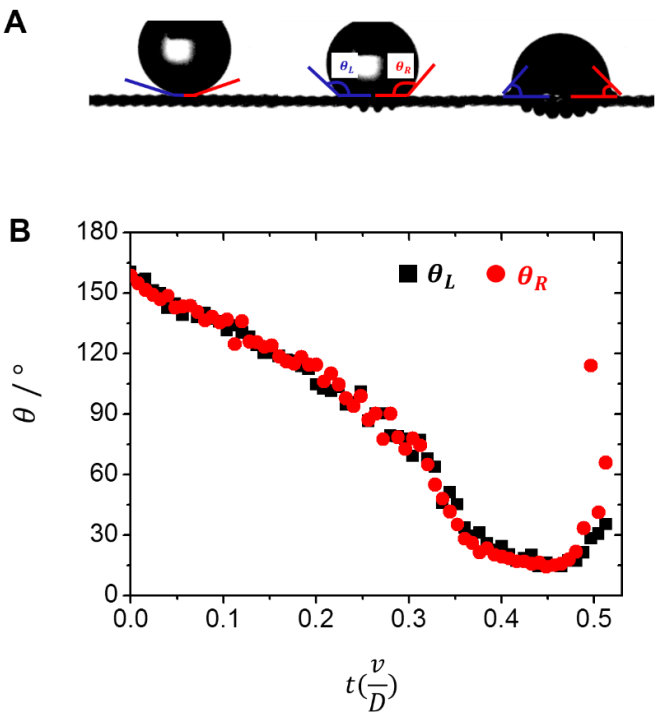

Figure 5-6. A. Images showing the progressive lateral deformation. θ_L and θ_R represent the left and the right contact angle with respect to the horizontal mesh surface, respectively. B: time evolution of θ_L and θ_R for PFAC6 N-200 mesh. Impact $We \approx 8.2$

0.11 ms. The good match of the two times implied the immediate penetration. Additionally, the formation of the liquid lamella is observed at a much later time. Therefore, we interpret that the water hammer pressure does not contribute to the droplet impact dynamics on textiles.

The formation of the lamella is typically accompanied by a sudden change of the microscopic contact angle, as illustrated in figure 5-6A. Taking the droplet impact on a PFAC6 N-200 textile at $We \approx 8.2$ as an example, the time evolution of the contact angle was presented in figure 5-6B for the determination of the lamella formation time. The good match between the left and the right contact angle shows the perfect symmetry of the impact. The lamella formation time determined from the $\theta - t$ curve is $t^* \approx 0.48$.

In the penetration stage $(0 < t^* < 0.2)$, for the droplet impact at $We > 20$ on textiles with pore sizes between 100 – 300 µm, the droplet penetrated the textile without alteration of the droplet shape. This feature is illustrated in the

insets of figure 5-7 where circular boundaries (red dashes) are super-imposed onto the planar projection of the droplet shape. The portion of the droplet that penetrated through the textile pores forms liquid filaments that extend out of the textile plane from the back surface, as seen in figure 5-7. We can model the surface of the droplet during the penetration stage as a sphere of a diameter D travelling at a velocity U_i in the negative z direction. The projection of such a sphere onto the xz plane is:

$$x^2 + (z - \frac{D}{2} + U_i t)^2 = \frac{D^2}{4} \tag{5.1}$$

According to this model, the spreading diameter d should be comparable to the length of the intersection of the xz projection with the plane $z = 0$:

$$d = 2\sqrt{DU_i t - (U_i t)^2} \tag{5.2}$$

the droplet height h should follow:

$$h = D - U_i t \tag{5.3}$$

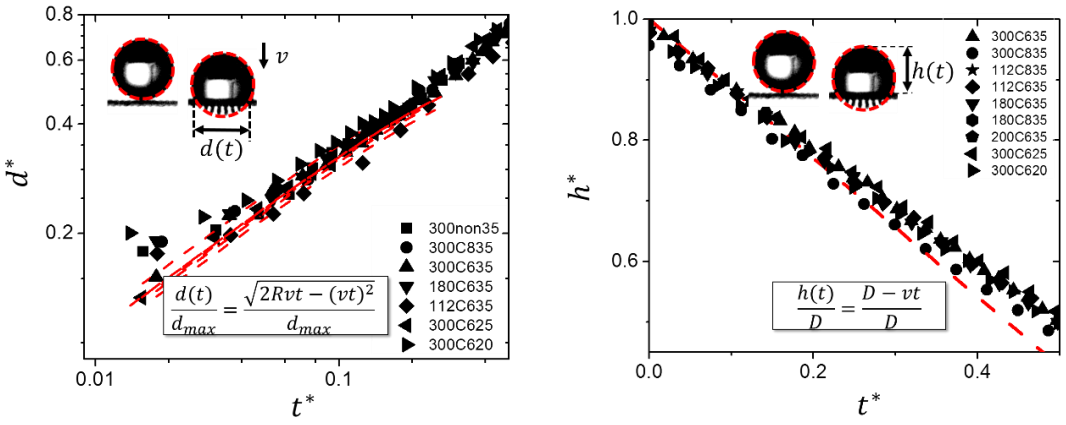

Figure 5-7. Droplet penetration at very early times. The results show the droplet penetrating the textile with no shape variations. Here, $d^* = \frac{d}{d_{max}}$ and $h^* = \frac{h}{D}$. The legend indicates the textile mesh size in micrometres, the type of coating, and the We number, e.g. 300C635 stands for mesh size 300 μm, PFAC6 coating, and $We \approx 35$. Penetration is not observed for $We < 20$. The dashed lines correspond to equation 5.2 (left) and equation 5.3 (right). Measurement error ±2 pixels.

The experimental data in the ranges of $0 < t^* < 0.2$ and $We > 20$ agreed well with the predictions from equation 5.2 and 5.3. Indeed, the presence of the textile pores permitted liquid flow through the pores lifting the compressibility constraint of an impenetrable boundary[62] and permitting the flow through the substrate without a visible change of the droplet shape.

We interpret that the droplet penetration was driven by inertia only with the estimation of the 'capillary time' t_c, because the surface tension effects only arise at t_c. For the penetration of a droplet of a low-viscosity liquid, by balancing inertia with capillarity[106] we obtain:

$$\frac{\rho d_{mesh}}{{t_c}^2} \sim \frac{\sigma}{{d_{mesh}}^2} \tag{5.4}$$

Which yields t_c:

$$t_c \sim \sqrt{\frac{\rho {d_{mesh}}^3}{\sigma}} \tag{5.5}$$

The normalised form of t_c is:

$$t^*_{capillary} = \left(\frac{\rho {d_{mesh}}^3}{\sigma}\right)^{1/2} \frac{U_i}{D} \tag{5.6}$$

In our experiments $t^*_{capillary}$ was in the range of 0.1 – 0.7 and the range coincided mostly with the timescale for the kinematic stage. Therefore, we believe that the penetration is only driven by inertia.

5.3.4 Effect of solid fraction on maximum spreading diameter d_{max}

Previously for the impact of droplets on superhydrophobic impenetrable substrates[78] and low porosity copper meshes[110], d_{max} was found to follow the power-law of $d_{max} = k_c \cdot D \cdot We^{1/4}$, where k_c is a scaling constant[78]. Here we show in figure 5-8 that for the impact on hydrophobic and hydrophilic textiles having a critical solid fraction of $\phi_c \approx 66\%$, d_{max} also followed $d_{max} = k_c \cdot D \cdot We^{1/4}$ with $k_c \approx 1$ (the blue solid line), defining solid fraction $\phi = \frac{d_{yarn}}{d_{yarn}+d_{mesh}}$ and d_{yarn} is the textile yarn diameter. Our ϕ_c was rather close to the reported $\phi_c \approx 70\%$ for superhydrophobic copper meshes[110]. For textiles with $\phi < \phi_c$

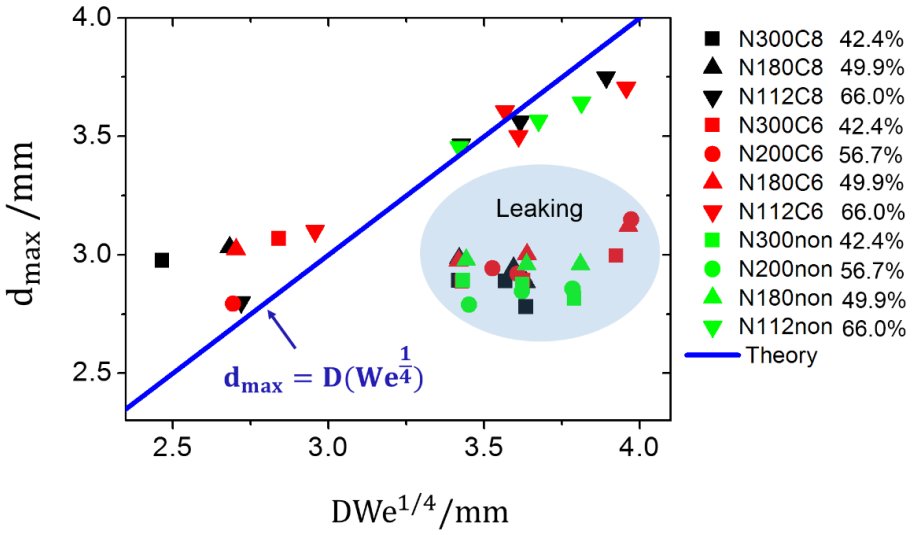

Figure 5-8. Maximum spreading diameter d_{max} as a function of the expected scaling $d_{max} = D \cdot We^{1/4}$. The blue-shaded region shows the cases where leaking (penetration) occurs. The green, red and black colours represent bare, PFAC6 and PFAC8 meshes and the various symbols indicate the textile pore sizes. Measurement error ±30 μm, every data point represents 20 repeats.

the measured d_{max} was smaller (up to 25% smaller) than the prediction of the power-law.

The disagreement between the measured d_{max} from the power-law prediction for the small ϕ textiles is caused by the severe liquid penetration. In each textile pore the penetrated liquid filament (figure 5-5) would be ruptured by the liquid surface tension into secondary droplets resulting in a volume loss of [106]:

$$V_0 \sim (d_{mesh})^2 \int_0^{t_c} U_i dt \tag{5.7}$$

Where t_c is from equation (5.5). If N is the number of pores covered by the impacting droplet, $N = \frac{A(1-\phi)}{(d_{mesh})^2}$ and A is the area that the droplet covers during the impact, the total volume loss $V_{loss} = NV_0$ is estimated as:

$$V_{loss} \sim U_i \sqrt{\frac{\rho (d_{mesh})^3}{\sigma}} (1-\phi) A \tag{5.8}$$

In equation (5.8) A is of the order of πD^2 and can be regarded as the same in all our experiments because of the strict control on D. For a textile having a small ϕ, according to $\phi = \frac{d_{yarn}}{d_{yarn}+d_{mesh}}$, the textile has a large d_{mesh}. Consequently, this textile would permit a great volume loss and there would be insufficient droplet volume on the textile surface to reach the predicted d_{max}.

5.3.5 Three regimes of liquid penetration

We identified three distinctive regimes of droplet penetration: no penetration (figure 5-9a), partial (figure 5-9b) and complete (figure 5-9c). The partial regime, also referred to as 'protrusion'[14], showed that a fraction of the droplet volume first passed through the mesh then mostly retracted back to the (upper) impact surface. In contrast, the complete regime showed that the penetrated droplet volume extended from the textile opposite surface and squirted liquid filaments that are subsequently ruptured into showering secondary droplets. In the 'no penetration' regime, no liquid volume passed through the textile at

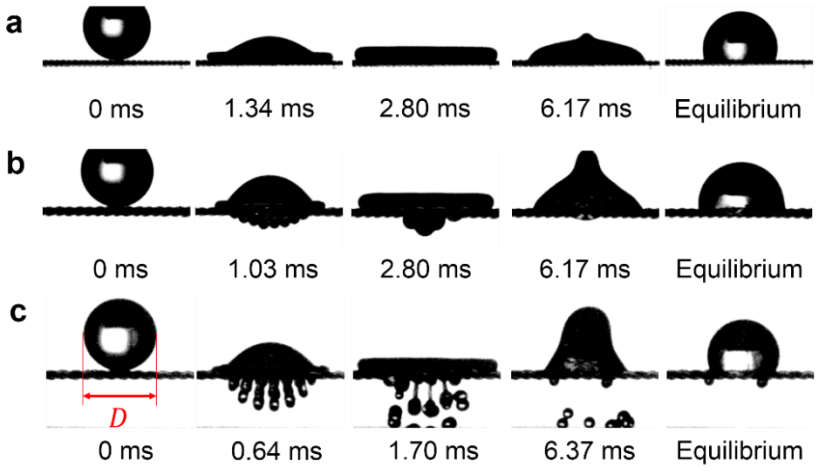

Figure 5-9. Penetration behaviour of droplet ($D \approx 1.56$ mm) for increasing We numbers. The sequence in a) shows no penetration for $We \approx 8.9$ and $d_{mesh} \approx 101$ μm. In b, for $We \approx 8.3$ and $d_{mesh} \approx 203$ μm, a portion of the droplet penetrates the textile but is driven back to the top surface. In c, for $We \approx 35.0$ and $d_{mesh} \approx 303$ μm, a fraction of the droplet permanently penetrates the textile, forming liquid filaments that break up into secondary droplets.

any time. The 'no penetration' regime demonstrated the best liquid repellency of the textile.

In the 'partial' regime, the retraction of the temporarily penetrated volume is determined by the textile coating. In figure 5-10 we compared the liquid

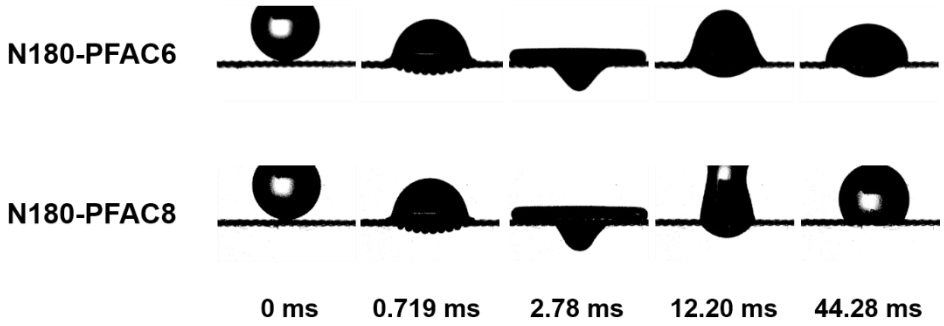

Figure 5-10. Image sequences showing the difference in the 'volume retraction' between PFAC6 and PFAC8 N180 meshes for $We \approx 8.4$.

retraction for the droplet impact on a PFAC6 and a PFAC8 textile. The retraction on the PFAC6 textile is incomplete, leaving a relatively large liquid volume on the back surface. The incomplete retraction was due to the high contact angle hysteresis of the PFAC6 coating.

Interestingly, at the equilibrium configuration of figure 5-9a and of 5-9c the contact angles were both 123 ± 2° whereas the penetration regimes were completely different. This observation confirmed that the evaluation of liquid repellency based only on the equilibrium contact angle[141] was inappropriate particularly for high velocity impact. The examination of the penetration regime should always be the first step for an appropriate evaluation of the liquid repellency.

Previous related work showed that in the 'complete' regime the liquid filaments were formed by several strings of secondary filaments ejected at different positions on the pore edge[106]. The secondary filaments typically twisted and entangled with one another due to the non-laminar liquid flow characteristic after the impact[106]. Unfortunately, our images in figure 5-9c cannot confirm this reported liquid filament formation due to the fact that the xz projections of multiple filaments super-imposed with one another and hindered the observation of the filament formation.

The rupture of the liquid filament was the fundamental difference between the 'partial' (figure 5-9b) and the 'complete' (figure 5-9c) regime. Researchers[14, 106] found that a long liquid cylinder broke at a critical cylinder aspect ratio $L_{0-critical} = \sqrt{2}\pi \approx 4.4$ based on Rayleigh instability. In our experiments the filaments corresponding to the central droplet-textile contact area typically having $4.5 \leq L_0 \leq 5.2$ would break. Whereas the filaments corresponding to the edge of the contact area ($L_0 \leq 2.0$) never broke.

5.3.6 Critical pore size d_{mesh} for droplet penetration

Through the $We - Re$ plot scientists have found that the viscous effects associated with the liquid flow through a single pore play a minor role in the

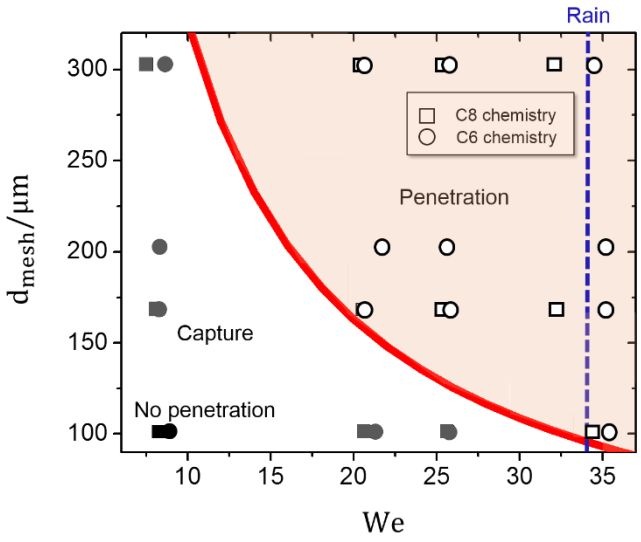

Figure 5-11. Penetration regimes for droplets impacting textiles. The solid line indicates the boundary between the penetration and no penetration regimes. Hollow symbols denote textile penetration. Grey symbols indicate capture, e.g. a portion of the droplet penetrates but is eventually drawn back to the impact surface. Black symbols indicate no penetration where neither temporary liquid penetration nor droplet footprint is observed on the back surface.

penetration resistance when the Reynolds number $Re = \frac{\rho U_i d_{mesh}}{2\mu} > 10$, μ is the dynamic viscosity[106]. In our experiments $\rho \approx 10^3$ kg/m^3, $\mu \approx 6 \cdot 10^{-3}$ Pa·s, the typical impact velocity is U_i~1 m/s and the characteristic pore size is

d_{mesh}~10^2 μm, therefore, we have the Reynolds number of the order of Re~10. This Re indicates that the viscous effects are relatively unimportant in the impact regimes studied here and could be neglected as a first approximation.

The capillary pressure exerted by a textile pore scales as $P_c \sim \frac{\sigma\Gamma}{A_{mesh}}$, where Γ and A_{mesh} are the perimeter and the area of the pore, respectively[14]. For square pores $\frac{\Gamma}{A_{mesh}}$ scales as $\frac{1}{d_{mesh}}$ and P_c is simplified to $P_c \sim \frac{\sigma}{d_{mesh}}$. Consequently, from the balance of dynamic pressure and capillary pressure we deduce:

$$\kappa\rho {U_i}^2 \approx \frac{\sigma}{d_{mesh}} \tag{5.9}$$

Where κ is an impact scaling factor determined by the textile geometry and occasionally by the surface wettability. Because $We = \frac{\rho {U_i}^2 D}{2\sigma}$, we obtain:

$$d_{mesh} \approx \frac{D}{2\kappa We} \tag{5.10}$$

at the onset of penetration.

Figure 5-11 shows our experimental results for the impact of droplets on textiles for $7 < We < 37$. The results in this figure are classified based on the impact outcome, e.g. penetration or no penetration (hollow or solid symbols). Figure 5-11 shows a clear separation of behaviours in terms of We and d_{mesh}. Equation (5.10) seems to describe the boundary between the penetration and no-penetration region well with $\kappa \approx 0.24$ and κ was determined when both D and d_{mesh} are using the standard units 'm'. Our results are consistent with the previous results[14,110] obtained for hydrophobic and superhydrophobic copper meshes. For example, Ryu et al.[14] have shown that the onset of impact penetration for both hydrophobic and superhydrophobic meshes with d_{mesh} >178 μm and 3.5 mm water droplets occurs for U_i~1 m/s ($We \approx 35$). Kumar et al.[110] observed penetration for meshes with $d_{mesh} \approx$ 140 and 280 μm penetration at $We \approx$ 35 and 204.

The design and the manufacturing of modern raincoats and umbrellas typically involve the utilisation of hydrophobic woven textiles for the aim of

good water droplet repellency with minimal reduction of the fabric breathability. Our results indicated the contrary to the popular belief: water droplet repellency cannot be achieved by the adjustment of the textile surface chemistry alone, because sufficiently rapid droplets could penetrate a textile regardless of its surface coatings. A useful example to discuss here is the raindrops. A raindrop of a size $d_{rain} \approx 1.6$ mm travelling at a speed of $U_{rain} \approx 1.77$ m/s [169] penetrates any hydrophobic textiles with pore sizes above 100 μm. To repel a faster or a larger raindrop than this example a smaller pore size will be required.

5.3.7 Effect of out-of-plane fibres on impact dynamics

Textiles made of pure cotton typically have high microscopic roughness due to the extension of many fibres out of the textile plane, as shown in figure 5-12A. The impact of droplets on such textile surfaces may not be completely symmetrical in the recorded images particularly during the receding process, as shown in figure 5-12B.

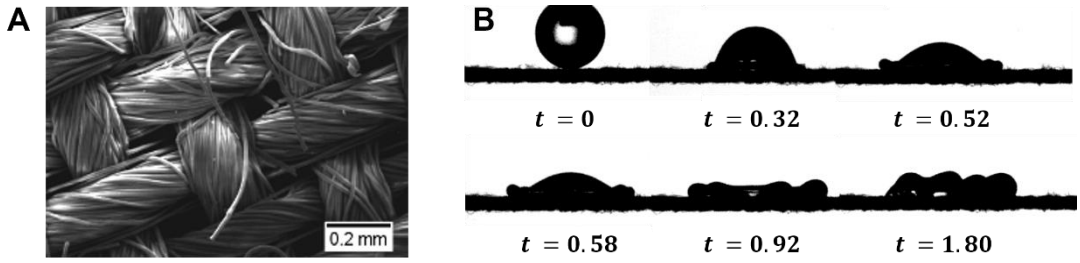

Figure 5-12. A. SEM image of a PFAC8 cotton textile. B. Image sequence of a droplet impacting the textile shown in A at $We \cong 11.5$. Droplet diameter $D \cong 1.56 \pm 0.12$ mm.

The asymmetry of the impact can be evidently seen if one compares the time evolution of the left and the right apparent contact angle. Our measurements of the contact angles were shown in figure 5-13. The data showed relatively bad collapse of the contact angles for $4 < t < 8$ ms. The spreading diameter d was measured in yz and xz views (see the co-ordinate system of figure 5-1) and the measurements were presented in figure 5-13A

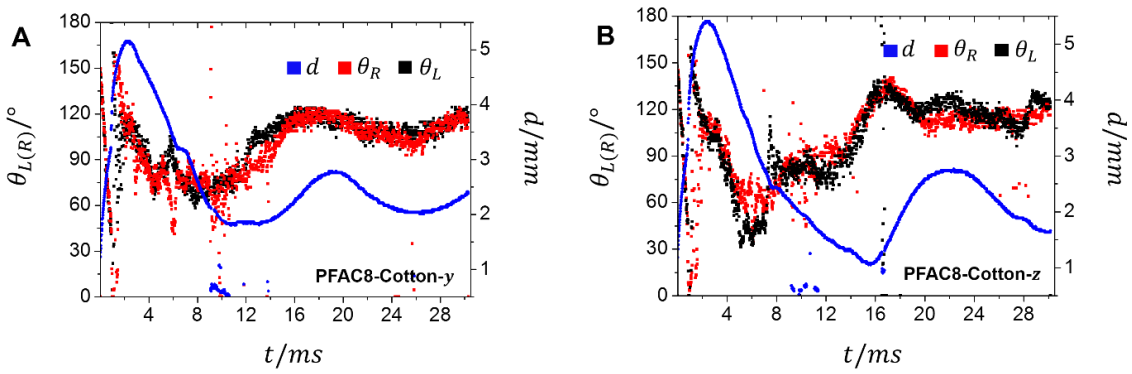

Figure 5-13. A: xy view of the left θ_L (black squares) and the right contact angle θ_R (red squares) as a function of time, and the spreading diameter d on the impact surface (blue square) as a function of time. B: Same as A for xz view. The textile is coated with PFAC8. The data points are averaged values over 20 repeats with measurement error no greater than 30 μm.

and B with blue symbols. The two blue curves showed different receding kinetics indicating that the impact is anisotropic. The impact anisotropy is possibly due to the anisotropic cotton textile pore shape (non-square shaped).

5.4 Conclusions

In this chapter, high-speed imaging was used to investigate the droplet impact dynamics on textiles having varying pore sizes and surface wettability characteristics. A key insight into the impact dynamics is the identification of the *penetration* stage, corresponding to $0 < t^* < 0.2$. During this stage, the droplet penetrates the textile through the textile pores and forms liquid filaments under the textile surface. Interestingly, in this stage, the droplet shape above the textile is not perturbed by the impact. Our findings are supported by previous experimental results on metallic meshes[14,110].

The maximum spreading diameter d_{max} has been found to conform to the well-known scaling $d_{max} = D(We^{1/4})$, which was initially developed for impermeable solids, for textiles with a solid fraction $\phi > 66\%$. This conclusion is in close agreement with the results by Kumar et al.[110] ($\phi > 70\%$) on superhydrophobic meshes.

We have shown three regimes of droplet impact penetration on non-wettable meshes, namely ‘no penetration’, ‘capture’ and ‘complete penetration’. Balancing the dynamic impact pressure ($\sim\rho v^2$) and the capillary pressure ($\sim\sigma/d_{mesh}$), the critical pore size has the form $d_{mesh} \sim D/We$. This simple model and our parametric experimental studies indicate that reducing the mesh size is an effective way to avoid liquid capture and penetration. This effect could be useful if the liquid contains contamination hazards.

6 Conclusions

In summary, for the transplanar spreading of a static droplet in a single-layer woven textile (chapter 4), we have provided experimental data for the description of the transplanar liquid movements in the interior of the textile. We disregarded the effects of gravity on the transplanar spreading by vertically placing the droplet-on-textile system during the tomography scans. The transplanar spreading is divided into the following stages, with each stage being associated with a particular geometric feature of the textile:

(1) As the first stage of the transplanar spreading, the liquid is transported by the relatively large inter-yarn pores of the textile. This stage is termed ‘pore penetration’. During the pore penetration, a fraction of the liquid also spreads into the textile yarns that are in direct contact with the liquid droplet.
(2) In the second stage, termed ‘contact region filling’, the liquid creeps into the ‘contact regions’ between the textile yarns. The transport of liquid in this stage mainly occurs in the direction parallel to the textile plane.
(3) In the third stage, termed ‘yarn saturation’, the liquid flows from the contact regions and the interior surfaces of the inter-yarn pores, and wicks in the interior of the yarns, along the yarn fibres.

To understand transplanar spreading dynamics, we studied the time evolution of the position of the advancing liquid front in the transplanar direction. The key findings are the following:

- The spreading kinetics cannot be described by a single power law. The asymptotic transplanar spreading rate is much smaller than the prediction of the Lucas-Washburn scaling.
- The high spreading rate in the early stage suggests that the initial liquid mass flux is governed by the spreading in the relatively large inter-yarn pores.
- Although models that are developed for the in-plane liquid spreading have been applied to the prediction of the in-plane spreading in textiles with some success, the assumption of the independence of the textile geometry for the large timescale in-plane liquid spreading is invalid for

the transplanar spreading. The small thickness of a textile prevents the establishment of the asymptotic flow before the liquid reaches the opposite surface of the textile.

In the chapter 5 of the droplet impact on a liquid-repellent textile we have provided experimental data particularly on the time evolution of the droplet spreading on the textile surface and the early stage droplet penetration through the textile pores. The droplet spreading can be divided into the following stages:

- Penetration stage: typically corresponding to $0 < t^* < 0.2$. The droplet penetrates the textile pores without any visible shape perturbation. Different from the droplet impact on an impermeable solid, no formation of the lateral liquid lamella at the bottom of the droplet could be observed in this stage.
- Kinematic stage (stage 1 of figure 5-4): The droplet diameter of the wetted region on the textile surface in this stage can be described by the scaling of $d \sim t^{1/2}$.
- Spreading stage (stage 2 of figure 5-4): the droplet spreading continues until the entire droplet volume becomes a flat ‘pancake’ with a visible rim on the edge.
- Receding stage (stage 3 of figure 5-4): the liquid ‘pancake’ on the textile surface recedes and the liquid volume returns to a spherical cap shaped droplet.
- Equilibrium (stage 4 of figure 5-4): the receded droplet oscillates in the direction normal to the textile plane before the droplet stabilises and shows the equilibrium wetting configuration.

We believe that these stages are universal for the description of the droplet movement on the plane of porous media having a mesh-like structure. Moreover, stage 1-4 have been previously identified for the droplet impact on smooth flat impermeable solids. The penetration stage 0 is unique for the textiles. The droplet shape in the penetration stage can be described by a simple ‘sphere model’. By comparing the impact in stage 0 on our liquid repellent textiles to that on a liquid repellent solid we have interpreted the

impact pressure to be the kinetic pressure of the order of $\rho {U_i}^2$. This pressure cannot be interpreted as the 'water hammer' pressure, because the pressure generated by the liquid compression is released quickly via the droplet penetration through the textile pores.

For a droplet impact at a sufficiently large We, the droplet penetration through the textile pores occurs simultaneously to the lateral spreading on the textile surface. The evolution of the droplet penetration is briefly summarised as follows:

- The initiation of the droplet penetration occurs in the penetration stage. A fraction of the droplet penetrates through the textile pores and forms liquid filaments that extend from the pores.
- The liquid filaments elongate and eventually rupture into secondary droplets at a critical filament aspect ratio of 4.8.

For a textile with a small solid fraction ϕ, the maximum spreading diameter d_{max} cannot be predicted by the scaling $d_{max} \sim DWe^{1/4}$ due to the severe droplet volume leaking upon the droplet penetration. For our textiles the critical ϕ for the good agreement between our measured d_{max} and the prediction of the scaling $d_{max} \sim DWe^{1/4}$ is about $\phi \approx 66\%$. This critical ϕ is in close agreement with the $\phi \approx 70\%$ from a previous paper[110].

By impacting droplets at different We on our textiles, we have identified a 'capture' and a 'penetration' regime for the droplet impact. The capture regime is divided into two impact outcomes that are 'no penetration' and 'partial penetration', based on the temporary droplet volume protrusion in the textile pores. In the penetration regime, droplets penetrate the textile pores and form secondary droplets under the textile. By the consideration of the balance between the impact pressure and the capillary resisting pressure, we have obtained the critical pore size of droplet penetration $d_{mesh} \sim \frac{D}{We}$ for the prediction of the impact regime of a given droplet. Our experimental data agreed well with the predictions by $d_{mesh} \sim \frac{D}{We}$. $d_{mesh} \sim \frac{D}{We}$ is crucial to the development of modern raincoats and umbrellas that require repellency to impacting droplets.

We have also studied the transplanar oil permeation in an oleophobic PFAC8 textile (chapter 3). We have re-produced the oil permeation by the creation of local structural 'defects' and by the increase of the droplet weight. Moreover, we have found a critical textile pore size d_m of the order $\sim\frac{\sigma}{P}$ for the oil permeation in our oleophobic textiles. We conclude that the oil permeation is purely driven by gravity.

In addition, for the correct prediction of the textile wettability through the meta-stable Cassie-Baxter (meta-CB) model[143, 146] for our PFAC6 and PFAC8 textiles, we have found that the θ_Y of the meta-CB model is not the classical Young's contact angle but the droplet contact angle $\theta_{Y-Micro}$ of the vector of the liquid-vapour interface with respect to the vector of the liquid-textile fibre interface. We provided $\theta_{Y-C6} \approx 50°$ for PFAC6 textiles and $\theta_{Y-C8} \approx 58°$ for PFAC8 textiles (chapter 4).

6.1 Future work

For the impact of droplets on textiles, our research here is only the first step towards the development of a complete theoretical model for the prediction of the critical pore size of droplet penetration. For example, the analysis on the derivation of the critical pore size here gives no information about the effect of the stiffness of the textile. But previous related work[103] through the examination of the droplet impact on silicone wafers with varying stiffness suggests that that the change of stiffness would lead to significant alteration in the droplet impact dynamics. Therefore, for the development of the complete model there is need to consider stiffness-related effects in the pressure balance. The stiffness control would probably require the application of a stretching force on the textiles. For the understanding of splashing or air-cushioning related effects, the textile porosity related effects such as liquid leaking may need to be considered in the classical Wagner's theory for the understanding on the generation of the ejecta sheet at the droplet bottom.

Another interesting problem is the impact of droplets on inclined textiles. Previous research[170] suggests that the capture of impacting droplets by inclined individual fibres increases dramatically with the tilting angle. It would be interesting to investigate the change of the critical pore size of droplet

penetration brought by the tilting of a textile. The results may be useful for the design of filters for the capturing of liquid and for the spray-coating on general fibrous materials.

7 Acknowledgement

For the financial support of this research, the author thanks the Material Research Institute (MRI) of Queen Mary University of London (QMUL) and the Defence Science Technology Laboratory (Dstl) of the U.K. This work is also partially supported by FLOWMAT EU funding grant N. 618335.

For the early-stage research related to the wetting of a textile, the author thanks Prof. Asa H. Barber of London South Bank University.

The author thanks the School of Engineering of University of Portsmouth for the grant of access to the Zeiss 520 Versa X-ray microscope. The author thanks Dr. Alexander P. Kao of University of Portsmouth and Dr. Rachna Parwani of Carl Zeiss in the U.S. for their valuable help in the X-ray tomography related experiments.

The author thanks Prof. Alfonso A. Castrejón-Pita of University of Oxford for his technical assistance in the design and the construction of the high-speed imaging system. The author thanks Mr. Miguel A. Quetzeri-Santiago for his assistance in the experiments of chapter 5.

8 References

1. Brewer, S. A.; Willis, C. R., Structure and oil repellency: textiles with liquid repellency to hexane. *Applied Surface Science* **2008,** *254* (20), 6450-6454.

2. Leng, B.; Shao, Z.; de With, G.; Ming, W., Superoleophobic cotton textiles. *Langmuir* **2009,** *25* (4), 2456-2460.

3. Advani, S. G.; Bruschke, M. V.; Parnas, R. S., Resin transfer molding flow phenomena in polymeric composites. *Composite materials series* **1994**, 465-465.

4. Abrate, S., Resin flow in fiber preforms. *Applied Mechanics Reviews* **2002,** *55* (6), 579-599.

5. Bartels, V., Physiological comfort of sportswear. In *Textiles in sport*, Elsevier: 2005; pp 177-203.

6. Gillespie, T., The spreading of low vapor pressure liquids in paper. *Journal of Colloid Science* **1958,** *13* (1), 32-50.

7. Kissa, E., Capillary sorption in fibrous assemblies. *Journal of colloid and interface science* **1981,** *83* (1), 265-272.

8. Pezron, I.; Bourgain, G.; Quéré, D., Imbibition of a fabric. *Journal of Colloid and Interface Science* **1995,** *173* (2), 319-327.

9. Patnaik, A.; Rengasamy, R.; Kothari, V.; Ghosh, A., Wetting and wicking in fibrous materials. *Textile Progress* **2006,** *38* (1), 1-105.

10. Miller, B.; Tyomkin, I., Spontaneous transplanar uptake of liquids by fabrics. *Textile Research Journal* **1984,** *54* (11), 706-712.

11. Starov, V.; Zhdanov, S.; Velarde, M., Spreading of liquid drops over thick porous layers: complete wetting case. *Langmuir* **2002,** *18* (25), 9744-9750.

12. Marmur, A., Drop penetration into a thin porous medium. *Journal of colloid and interface science* **1988,** *123* (1), 161-169.

13. Williams, E. M.; Dodds, M.; Taylor, M. C.; Li, J.; Michielsen, S., Impact dynamics of porcine drip bloodstains on fabrics. *Forensic science international* **2016,** *262*, 66-72.

14. Ryu, S.; Sen, P.; Nam, Y.; Lee, C., Water Penetration through a Superhydrophobic Mesh During a Drop Impact. *Physical review letters* **2017,** *118* (1), 014501.

15. Engel, O. G., Waterdrop collisions with solid surfaces. *Journal of Research of the National Bureau of Standards* **1955,** *54* (5), 281-298.

16. Eggers, J.; Fontelos, M. A.; Josserand, C.; Zaleski, S., Drop dynamics after impact on a solid wall: theory and simulations. *Physics of Fluids* **2010,** *22* (6), 062101.

17. Lesser, M. In *Analytic solutions of liquid-drop impact problems*, Proceedings of the Royal Society of London A: Mathematical, Physical and Engineering Sciences, The Royal Society: 1981; pp 289-308.

18. Xu, J.; Xie, J.; He, X.; Cheng, Y.; Liu, Q., Water drop impacts on a single-layer of mesh screen membrane: Effect of water hammer pressure and advancing contact angles. *Experimental Thermal and Fluid Science* **2017,** *82*, 83-93.

19. Heymann, F., High-Speed Impact between a Liquid Drop and a Solid Surface. *Journal of Applied Physics* **1969,** *40* (13), 5113-5122.

20. Bencsik, M.; Adriaensen, H.; Brewer, S. A.; McHale, G., Quantitative NMR monitoring of liquid ingress into repellent heterogeneous layered fabrics. *Journal of Magnetic Resonance* **2008,** *193* (1), 32-36.

21. Weder, M.; Brühwiler, P. A.; Laib, A., X-ray tomography measurements of the moisture distribution in multilayered clothing systems. *Textile research journal* **2006,** *76* (1), 18-26.

22. Alleborn, N.; Raszillier, H., Spreading and sorption of a droplet on a porous substrate. *Chemical Engineering Science* **2004,** *59* (10), 2071-2088.

23. Leng, B., Shao, Z., de With, G., & Ming, W. , Superoleophobic cotton textiles. *Langmuir* **2009,** *25* (4), 2456-2460.

24. Birrfelder, P.; Dorrestijn, M.; Roth, C.; Rossi, R. M., Effect of fiber count and knit structure on intra-and inter-yarn transport of liquid water. *Textile Research Journal* **2013,** *83* (14), 1477-1488.

25. Bartels, V. T., Physiological comfort of sportswear. *Textiles in sport* **2005**, 177-203.

26. Zhang, G.; Parwani, R.; Stone, C. A.; Barber, A. H.; Botto, L., X-ray imaging of transplanar liquid transport mechanisms in single layer textiles. *Langmuir* **2017**.

27. Bell, J. M.; Cameron, F., The flow of liquids through capillary spaces. *The Journal of Physical Chemistry* **1906,** *10* (8), 658-674.

28. Peek Jr, R.; McLean, D., Capillary penetration of fibrous materials. *Industrial & Engineering Chemistry Analytical Edition* **1934,** *6* (2), 85-90.

29. Alava, M.; Dubé, M.; Rost, M., Imbibition in disordered media. *Advances in Physics* **2004,** *53* (2), 83-175.

30. Gillespie, T., The capillary rise of a liquid in a vertical strip of filter paper. *Journal of Colloid Science* **1959,** *14* (2), 123-130.

31. Muskat, M.; Meres, M. W., The flow of heterogeneous fluids through porous media. *Physics* **1936,** *7* (9), 346-363.

32. Washburn, E. W., The dynamics of capillary flow. *Physical review* **1921,** *17* (3), 273.

33. Schoelkopf, J.; Gane, P.; Ridgway, C., A comparison of the various liquid interaction radii derived from experiment and network modelling of porous pigmented structures. *Colloids and Surfaces A: Physicochemical and Engineering Aspects* **2004,** *251* (1), 149-159.

34. Kumar, S. M.; Deshpande, A. P., Dynamics of drop spreading on fibrous porous media. *Colloids and Surfaces A: Physicochemical and Engineering Aspects* **2006,** *277* (1), 157-163.

35. Wiklund, H. S.; Uesaka, T., Microfluidics of imbibition in random porous media. *Physical Review E* **2013,** *87* (2), 023006.

36. Marmur, A., Penetration of a small drop into a capillary. *Journal of Colloid and Interface Science* **1988,** *122* (1), 209-219.

37. Sarkar, M.; Fan, J.; Qian, X., Transplanar water transport tester for fabrics. *Measurement Science and Technology* **2007,** *18* (5), 1465.

38. Rossi, R. M.; Stämpfli, R.; Psikuta, A.; Rechsteiner, I.; Brühwiler, P. A., Transplanar and in-plane wicking effects in sock materials under pressure. *Textile Research Journal* **2011,** *81* (15), 1549-1558.

39. Starov, V.; Kostvintsev, S.; Sobolev, V.; Velarde, M.; Zhdanov, S., Spreading of liquid drops over dry porous layers: complete wetting case. *Journal of Colloid and Interface Science* **2002,** *252* (2), 397-408.

40. Bayramli, E.; Powell, R., The normal (transverse) impregnation of liquids into axially oriented fiber bundles. *Journal of colloid and interface science* **1990,** *138* (2), 346-353.

41. Karppinen, T.; Kassamakov, I.; Aaltonen, J.; Pajari, H.; Hæggström, E., Measuring liquid penetration in the thickness direction of paper. *The European Physical Journal-Applied Physics* **2005,** *32* (1), 65-71.

42. Hyväluoma, J.; Raiskinmäki, P.; Jäsberg, A.; Koponen, A.; Kataja, M.; Timonen, J., Simulation of liquid penetration in paper. *Physical Review E* **2006,** *73* (3), 036705.

43. Bayramli, E., & Powell, R. L. , Impregnation dynamics of carbon fiber tows. *Journal of composite materials* **1992,** *26* (10), 1427-1442.

44. Starov, V.; Kosvintsev, S.; Sobolev, V.; Velarde, M.; Zhdanov, S., Spreading of liquid drops over saturated porous layers. *Journal of colloid and interface science* **2002,** *246* (2), 372-379.

45. Joanny, J.-F., Spreading of superfluid drops. *Journal de Physique* **1985,** *46* (5), 807-813.

46. Rideal, E. K., CVIII. On the flow of liquids under capillary pressure. *The London, Edinburgh, and Dublin Philosophical Magazine and Journal of Science* **1922,** *44* (264), 1152-1159.

47. Danino, D.; Marmur, A., Radial capillary penetration into paper: limited and unlimited liquid reservoirs. *Journal of colloid and interface science* **1994,** *166* (1), 245-250.

48. Marmur, A., Kinetics of penetration into uniform porous media: testing the equivalent-capillary concept. *Langmuir* **2003,** *19* (14), 5956-5959.

49. Scheidegger, A., *The physics of flow through porous media*. University Of Toronto Press: London: 1958.

50. Marmur, A., The radial capillary. *Journal of colloid and interface science* **1988,** *124* (1), 301-308.

51. Ashari, A.; Bucher, T.; Tafreshi, H. V.; Tahir, M.; Rahman, M., Modeling fluid spread in thin fibrous sheets: Effects of fiber orientation. *International Journal of Heat and Mass Transfer* **2010,** *53* (9), 1750-1758.

52. Wyckoff, R.; Botset, H., The Flow of Gas-Liquid Mixtures Through Unconsolidated Sands. *Physics* **1936,** *7* (9), 325-345.

53. Muskat, M. *The flow of homogeneous fluids through porous media*; 1946.

54. Liu, K.; Jiang, L., Bio-inspired self-cleaning surfaces. *Annual Review of Materials Research* **2012,** *42*, 231-263.

55. Blossey, R., Self-cleaning surfaces—virtual realities. *Nature materials* **2003,** *2* (5), 301-306.

56. Mishchenko, L.; Hatton, B.; Bahadur, V.; Taylor, J. A.; Krupenkin, T.; Aizenberg, J., Design of ice-free nanostructured surfaces based on repulsion of impacting water droplets. *ACS nano* **2010,** *4* (12), 7699-7707.

57. Meuler, A. J.; McKinley, G. H.; Cohen, R. E., Exploiting topographical texture to impart icephobicity. *ACS nano* **2010,** *4* (12), 7048-7052.

58. Cao, C.; Ge, M.; Huang, J.; Li, S.; Deng, S.; Zhang, S.; Chen, Z.; Zhang, K.; Al-Deyab, S. S.; Lai, Y., Robust fluorine-free superhydrophobic PDMS–ormosil@ fabrics for highly effective self-cleaning and efficient oil–water separation. *Journal of Materials Chemistry A* **2016,** *4* (31), 12179-12187.

59. Roisman, I. V.; Rioboo, R.; Tropea, C. In *Normal impact of a liquid drop on a dry surface: model for spreading and receding*, Proceedings of the Royal Society of London A: Mathematical, Physical and Engineering Sciences, The Royal Society: 2002; pp 1411-1430.

60. Rein, M., Phenomena of liquid drop impact on solid and liquid surfaces. *Fluid Dynamics Research* **1993,** *12* (2), 61-93.

61. Yarin, A. L., Drop impact dynamics: splashing, spreading, receding, bouncing…. *Annu. Rev. Fluid Mech.* **2006,** *38*, 159-192.

62. Rioboo, R., M. Marengo, and C. Tropea., Time evolution of liquid drop impact onto solid, dry surfaces. *Experiments in fluids* **2002,** *33* (1), 112-124.

63. Bird, J. C.; Dhiman, R.; Kwon, H.-M.; Varanasi, K. K., Reducing the contact time of a bouncing drop. *Nature* **2013,** *503* (7476), 385-388.

64. Liu, Y.; Andrew, M.; Li, J.; Yeomans, J. M.; Wang, Z., Symmetry breaking in drop bouncing on curved surfaces. *Nature communications* **2015,** *6*.

65. Liu, Y.; Moevius, L.; Xu, X.; Qian, T.; Yeomans, J. M.; Wang, Z., Pancake bouncing on superhydrophobic surfaces. *Nature physics* **2014,** *10* (7), 515-519.

66. Roux, D.; Cooper-White, J., Dynamics of water spreading on a glass surface. *Journal of colloid and interface science* **2004,** *277* (2), 424-436.

67. Cook, S. S., Erosion by water-hammer. *Proc. R. Soc. Lond. A* **1928,** *119* (783), 481-488.

68. Dear, J.; Field, J., High-speed photography of surface geometry effects in liquid/solid impact. *Journal of Applied Physics* **1988,** *63* (4), 1015-1021.

69. Skalak, R.; Feit, D., Impact on the Surface of a Compressible Fluid. *Journal of Engineering for Industry* **1966,** *88* (3), 325-331.

70. Ghidaoui, M. S., On the fundamental equations of water hammer. *Urban Water Journal* **2004,** *1* (2), 71-83.

71. Savic, P.; Boult, G. T., Heat Transfer and Fluid Mechanics Institute. *California Insti-tute of Technology* **1957**, 43-84.

72. Engel, O. G., Note on particle velocity in collisions between liquid drops and solids. *J. Res. Natl. Bur. Stand., Sect. A* **1960,** *64*, 497-498.

73. Ghadiri, H.; Payne, D., Raindrop impact stress. *European Journal of Soil Science* **1981,** *32* (1), 41-49.

74. Tsai, P.; Pacheco, S.; Pirat, C.; Lefferts, L.; Lohse, D., Drop impact upon micro-and nanostructured superhydrophobic surfaces. *Langmuir* **2009,** *25* (20), 12293-12298.

75. Soto, D.; De Lariviere, A. B.; Boutillon, X.; Clanet, C.; Quéré, D., The force of impacting rain. *Soft matter* **2014,** *10* (27), 4929-4934.

76. Chandra, S.; Avedisian, C., On the collision of a droplet with a solid surface. *Proc. R. Soc. Lond. A* **1991,** *432* (1884), 13-41.

77. Richard, D.; Clanet, C.; Quéré, D., Surface phenomena: Contact time of a bouncing drop. *Nature* **2002,** *417* (6891), 811-811.

78. Clanet, C.; Béguin, C.; Richard, D.; Quéré, D., Maximal deformation of an impacting drop. *Journal of Fluid Mechanics* **2004,** *517*, 199-208.

79. Pasandideh-Fard, M.; Qiao, Y.; Chandra, S.; Mostaghimi, J., Capillary effects during droplet impact on a solid surface. *Physics of fluids* **1996,** *8* (3), 650-659.

80. Mao, T.; Kuhn, D.; Tran, H., Spread and rebound of liquid droplets upon impact on flat surfaces. *AIChE Journal* **1997,** *43* (9), 2169-2179.

81. Antonini, C.; Amirfazli, A.; Marengo, M., Drop impact and wettability: From hydrophilic to superhydrophobic surfaces. *Physics of fluids* **2012,** *24* (10), 102104.

82. Scheller, B. L.; Bousfield, D. W., Newtonian drop impact with a solid surface. *AIChE Journal* **1995,** *41* (6), 1357-1367.

83. Renardy, Y.; Popinet, S.; Duchemin, L.; Renardy, M.; Zaleski, S.; Josserand, C.; Drumright-Clarke, M.; Richard, D.; Clanet, C.; Quéré, D.,

Pyramidal and toroidal water drops after impact on a solid surface. *Journal of Fluid Mechanics* **2003,** *484*, 69-83.

84. Marston, J.; Thoroddsen, S. T.; Ng, W.; Tan, R., Experimental study of liquid drop impact onto a powder surface. *Powder technology* **2010,** *203* (2), 223-236.

85. Nefzaoui, E.; Skurtys, O., Impact of a liquid drop on a granular medium: Inertia, viscosity and surface tension effects on the drop deformation. *Experimental Thermal and Fluid Science* **2012,** *41*, 43-50.

86. Marston, J.; Zhu, Y.; Vakarelski, I. U.; Thoroddsen, S. T., Deformed liquid marbles: Freezing drop oscillations with powders. *Powder technology* **2012,** *228*, 424-428.

87. Marston, J.; Sprittles, J. E.; Zhu, Y.; Li, E.; Vakarelski, I. U.; Thoroddsen, S. T., Drop spreading and penetration into pre-wetted powders. *Powder technology* **2013,** *239*, 128-136.

88. Yokoi, K.; Vadillo, D.; Hinch, J.; Hutchings, I., Numerical studies of the influence of the dynamic contact angle on a droplet impacting on a dry surface. *Physics of Fluids* **2009,** *21* (7), 072102.

89. Rioboo, R.; Tropea, C.; Marengo, M., Outcomes from a drop impact on solid surfaces. *Atomization and Sprays* **2001,** *11* (2).

90. Antonini, C.; Villa, F.; Bernagozzi, I.; Amirfazli, A.; Marengo, M., Drop rebound after impact: the role of the receding contact angle. *Langmuir* **2013,** *29* (52), 16045-16050.

91. Li, X.; Ma, X.; Lan, Z., Dynamic behavior of the water droplet impact on a textured hydrophobic/superhydrophobic surface: the effect of the remaining liquid film arising on the pillars' tops on the contact time. *Langmuir* **2010,** *26* (7), 4831-4838.

92. Bartolo, D.; Bouamrirene, F.; Verneuil, E.; Buguin, A.; Silberzan, P.; Moulinet, S., Bouncing or sticky droplets: Impalement transitions on superhydrophobic micropatterned surfaces. *EPL (Europhysics Letters)* **2006,** *74* (2), 299.

93. Gauthier, A.; Symon, S.; Clanet, C.; Quéré, D., Water impacting on superhydrophobic macrotextures. *Nature communications* **2015,** *6*.

94. Yarin, A.; Weiss, D., Impact of drops on solid surfaces: self-similar capillary waves, and splashing as a new type of kinematic discontinuity. *Journal of Fluid Mechanics* **1995,** *283*, 141-173.

95. Rioboo, R.; Bauthier, C.; Conti, J.; Voue, M.; De Coninck, J., Experimental investigation of splash and crown formation during single drop impact on wetted surfaces. *Experiments in fluids* **2003,** *35* (6), 648-652.

96. Sivakumar, D.; Tropea, C., Splashing impact of a spray onto a liquid film. *Physics of fluids* **2002,** *14* (12), L85-L88.

97. Cossali, G.; Marengo, M.; Coghe, A.; Zhdanov, S., The role of time in single drop splash on thin film. *Experiments in Fluids* **2004,** *36* (6), 888-900.

98. Thoroddsen, S. T.; Thoraval, M.-J.; Takehara, K.; Etoh, T., Droplet splashing by a slingshot mechanism. *Physical review letters* **2011,** *106* (3), 034501.

99. Bussmann, M.; Chandra, S.; Mostaghimi, J., Modeling the splash of a droplet impacting a solid surface. *Physics of fluids* **2000,** *12* (12), 3121-3132.

100. Xu, L., Liquid drop splashing on smooth, rough, and textured surfaces. *Physical Review E* **2007,** *75* (5), 056316.

101. Xu, L.; Zhang, W. W.; Nagel, S. R., Drop splashing on a dry smooth surface. *Physical review letters* **2005,** *94* (18), 184505.

102. Davies, C.; Khan, M.; Ghauri, A.; Ranaboldo, C., Blood and body fluid splashes during surgery–the need for eye protection and masks. *The Annals of The Royal College of Surgeons of England* **2007,** *89* (8), 770-772.

103. Howland, C. J.; Antkowiak, A.; Castrejón-Pita, J. R.; Howison, S. D.; Oliver, J. M.; Style, R. W.; Castrejón-Pita, A. A., It's Harder to Splash on Soft Solids. *Physical review letters* **2016,** *117* (18), 184502.

104. Song, M.; Ju, J.; Luo, S.; Han, Y.; Dong, Z.; Wang, Y.; Gu, Z.; Zhang, L.; Hao, R.; Jiang, L., Controlling liquid splash on superhydrophobic surfaces by a vesicle surfactant. *Science Advances* **2017,** *3* (3), e1602188.

105. Damak, M.; Mahmoudi, S. R.; Hyder, M. N.; Varanasi, K. K., Enhancing droplet deposition through in-situ precipitation. *Nature communications* **2016,** *7*.

106. Lorenceau, É.; Quéré, D., Drops impacting a sieve. *Journal of colloid and interface science* **2003,** *263* (1), 244-249.

107. Delbos, A.; Lorenceau, E.; Pitois, O., Forced impregnation of a capillary tube with drop impact. *Journal of colloid and interface science* **2010,** *341* (1), 171-177.

108. Bordoloi, A. D.; Longmire, E. K., Drop motion through a confining orifice. *Journal of Fluid Mechanics* **2014,** *759*, 520-545.

109. An, T.; Cho, S. J.; Choi, W.; Kim, J. H.; Lim, S. T.; Lim, G., Preparation of stable superhydrophobic mesh with a biomimetic hierarchical structure. *Soft Matter* **2011,** *7* (21), 9867-9870.

110. Kumar, A.; Tripathy, A.; Nam, Y.; Lee, C.; Sen, P., Effect of Geometrical Parameters on Rebound of Impacting Droplets on Leaky Superhydrophobic Meshes. *Soft Matter* **2018**.

111. Deng, T.; Varanasi, K. K.; Hsu, M.; Bhate, N.; Keimel, C.; Stein, J.; Blohm, M., Nonwetting of impinging droplets on textured surfaces. *Applied Physics Letters* **2009,** *94* (13), 133109.

112. Brunet, P.; Lapierre, F.; Zoueshtiagh, F.; Thomy, V.; Merlen, A., To grate a liquid into tiny droplets by its impact on a hydrophobic microgrid. *Applied Physics Letters* **2009,** *95* (25), 254102.

113. Cavazzini, M., Montanari, F., Pozzi, G., & Quici, S., Perfluorocarbon-soluble catalysts and reagents and the application of FBS (fluorous biphase system) to organic synthesis. *Journal of fluorine chemistry* **1999,** *94* (2), 183-193.

114. Horvath, I., & Rábai, J., Facile catalyst separation without water: fluorous biphase hydroformylation of olefins. *Science* **1994,** *266* (5182), 72-76.

115. Jäckel, C., Salwiczek, M., & Koksch, B., Fluorine in a native protein environment—how the spatial demand and polarity of fluoroalkyl groups affect protein folding. *Angewandte Chemie International Edition* **2006,** *45* (25), 4198-4203.

116. Zhang, Q., Wang, Q., Jiang, J., Zhan, X., & Chen, F., Microphase structure, crystallization behavior, and wettability properties of novel fluorinated copolymers poly (perfluoroalkyl acrylate-co-stearyl acrylate) containing short perfluorohexyl chains. *Langmuir* **2015,** *31* (16), 4752-4760.

117. Bellanger, H., Darmanin, T., & Guittard, F., Surface structuration (micro and/or nano) governed by the fluorinated tail lengths toward superoleophobic surfaces. *Langmuir* **2011,** *28* (1), 186-192.

118. Honda, K., Morita, M., Otsuka, H., & Takahara, A. , Molecular aggregation structure and surface properties of poly (fluoroalkyl acrylate) thin films. *Macromolecules* **2005,** *38* (13), 5699-5705.

119. Coulson, S. R., Woodward, I., Badyal, J. P. S., Brewer, S. A., & Willis, C. , Super-repellent composite fluoropolymer surfaces. *The Journal of Physical Chemistry B* **2000,** *104* (37), 8836-8840.

120. Coulson, S. R., Woodward, I. S., Badyal, J. P. S., Brewer, S. A., & Willis, C. , Plasmachemical functionalization of solid surfaces with low surface energy perfluorocarbon chains. *Langmuir* **2000,** *16* (15), 6287-6293.

121. Pittman, A. G., Sharp, D. L., & Ludwig, B. A., Polymers derived from fluoroketones. II. Wetting properties of fluoroalkyl acrylates and methacrylates. *Journal of Polymer Science Part A: Polymer Chemistry* **1968,** *6* (6), 1729-1740.

122. Katano, Y., Tomono, H., & Nakajima, T., Surface property of polymer films with fluoroalkyl side chains. *Macromolecules* **1994,** *27* (8), 2342-2344.

123. Owen, M. J., Low surface energy inorganic polymers. *Comments on Inorganic Chemistry* **1988,** *7* (4), 195-213.

124. Graham, P., Stone, M., Thorpe, A., Nevell, T. G., & Tsibouklis, J., Fluoropolymers with very low surface energy characteristics. *Journal of Fluorine Chemistry* **2000,** *104* (1), 29-36.

125. Honda, K.; Morita, M.; Otsuka, H.; Takahara, A., Molecular aggregation structure and surface properties of poly (fluoroalkyl acrylate) thin films. *Macromolecules* **2005,** *38* (13), 5699-5705.

126. Kissa, E., Repellent finishes. *Handbook of fiber science and technology* **1984,** *2* (Part B), 144-145.

127. Katsuragawa, T., Chiba, E., Okada, K., Tani, K., & Tomono, H., Surface structure analysis of polyacrylate thin films. *Japanese journal of applied physics* **1995,** *34* (2R), 649.

128. Pittman, A. G., & Ludwig, B. A., Effect of polymer crystallinity on the wetting properties of certain fluoroalkyl acrylates. *Journal of Polymer Science Part A: Polymer Chemistry* **1969,** *7* (11), 3053-3066.

129. Immergut, E. H., & Mark, H. F., Principles of plasticization. **1965**, 1–26.

130. Van Damme, H. S., Hogt, A. H., & Feijen, J., Surface mobility and structural transitions of poly (n-alkyl methacrylates) probed by dynamic contact angle measurements. *Journal of colloid and interface science* **1986,** *114* (1), 167-172.

131. Honda, K., Morita, M., Sakata, O., Sasaki, S., & Takahara, A., Effect of surface molecular aggregation state and surface molecular motion on wetting behavior of water on poly (fluoroalkyl methacrylate) thin films. *Macromolecules* **2009,** *43* (1), 454-460.

132. Stone, M., Nevell, T. G., & Tsibouklis, J., Surface energy characteristics of poly (perfluoroacrylate) film structures. *Materials Letters* **1998,** *37* (1), 102-105.

133. Bunn, C. W., & Howells, E. R., Structures of molecules and crystals of fluoro-carbons. *Nature* **1954,** *174* (4429), 549-551.

134. Bunn, C. W., The crystal structure of long-chain normal paraffin hydrocarbons. The “shape” of the< CH2 group. *Transactions of the Faraday Society* **1939,** *35*, 482-491.

135. Jiang, J., Zhang, G., Wang, Q., Zhang, Q., Zhan, X., & Chen, F, Novel fluorinated polymers containing short perfluorobutyl side chains and their super wetting performance on diverse substrates. *ACS applied materials & interfaces* **2016,** *8* (16), 10513-10523.

136. Ruan, T., Wang, Y., Wang, T., Zhang, Q., Ding, L., Liu, J., Wang, C., Qu, G. and Jiang, G., Presence and partitioning behavior of polyfluorinated iodine alkanes in environmental matrices around a fluorochemical manufacturing plant: another possible source for perfluorinated carboxylic acids? *Environmental science & technology* **2010,** *44* (15), 5755-5761.

137. Yoo, H., Kannan, K., Kim, S. K., Lee, K. T., Newsted, J. L., & Giesy, J. P. , Perfluoroalkyl acids in the egg yolk of birds from Lake Shihwa, Korea. *Environmental science & technology* **2008,** *42* (15), 5821-5827.

138. Kannan, K., Perfluoroalkyl and polyfluoroalkyl substances: current and future perspectives. *Environmental chemistry* **2011,** *8* (4), 333-338.

139. Wang, Z., Cousins, I. T., Scheringer, M., & Hungerbuehler, K. , Hazard assessment of fluorinated alternatives to long-chain perfluoroalkyl acids (PFAAs) and their precursors: status quo, ongoing challenges and possible solutions. *Environment international* **2015,** *75*, 172-179.

140. Conder, J. M., Hoke, R. A., Wolf, W. D., Russell, M. H., & Buck, R. C. , Are PFCAs bioaccumulative? A critical review and comparison with regulatory criteria and persistent lipophilic compounds. *Environmental science & technology* **2008,** *42* (4), 995-1003.

141. Tuteja, A.; Choi, W.; Ma, M.; Mabry, J. M.; Mazzella, S. A.; Rutledge, G. C.; McKinley, G. H.; Cohen, R. E., Designing superoleophobic surfaces. *Science* **2007,** *318* (5856), 1618-1622.

142. Kleingartner, J. A.; Srinivasan, S.; Truong, Q. T.; Sieber, M.; Cohen, R. E.; McKinley, G. H., Designing Robust Hierarchically Textured Oleophobic Fabrics. *Langmuir* **2015,** *31* (48), 13201-13213.

143. Lee, H. J.; Willis, C. R.; Stone, C. A., Modeling and preparation of a super-oleophobic non-woven fabric. *Journal of materials science* **2011,** *46* (11), 3907-3913.

144. Liu, Y.; Wang, Z., Superhydrophobic porous networks for enhanced droplet shedding. *Scientific reports* **2016,** *6*.

145. Aminayi, P.; Abidi, N., Ultra-oleophobic cotton fabric prepared using molecular and nanoparticle vapor deposition methods. *Surface and Coatings Technology* **2015,** *276*, 636-644.

146. Stachewicz, U.; Bailey, R. J.; Zhang, H.; Stone, C. A.; Willis, C. R.; Barber, A. H., Wetting hierarchy in oleophobic 3D electrospun nanofiber networks. *ACS applied materials & interfaces* **2015,** *7* (30), 16645-16652.

147. Borhan, A.; Rungta, K., On the radial spreading of liquids in thin porous substrates. *Journal of colloid and interface science* **1992,** *154* (1), 295-297.

148. Brewer, S. A., & Willis, C. R., Structure and oil repellency: textiles with liquid repellency to hexane. *Appl. Surf. Sci.* **2008,** *254* (20), 6450-6454.

149. Gillespie, T., The spreading of low vapor pressure liquids in paper. *J. Colloid Sci.* **1958,** *13* (1), 32-50.

150. Patnaik, A., Rengasamy, R. S., Kothari, V. K., & Ghosh, A., Wetting and wicking in fibrous materials. *Text. Prog.* **2006,** *38* (1), 1-105.

151. Kissa, E., Capillary sorption in fibrous assemblies. *J. Colloid Interface Sci.* **1981,** *83* (1), 265-272.

152. Danino, D., & Marmur, A., Radial capillary penetration into paper: limited and unlimited liquid reservoirs. *J. Colloid Interface Sci.* **1994,** *166* (1), 245-250.

153. Salminen, P. Studies of water transport in paper during short contact times. Åbo Akademi, 1988.

154. Rudolf, M., Boutelier, D., Rosenau, M., Schreurs, G., & Oncken, O., Rheological benchmark of silicone oils used for analog modeling of short-and long-term lithospheric deformation. *Tectonophysics* **2016,** *684*, 12-22.

155. Arganda-Carreras I, K. V., Rueden C, Eliceiri KW, Schindelin J, Cardona A, Seung HS, Trainable Weka Segmentation: a machine learning tool for microscopy pixel classification. *Bioinformatics* **2017**.

156. Courbin, L., Denieul, E., Dressaire, E., Roper, M., Ajdari, A., & Stone, H. A. , Imbibition by polygonal spreading on microdecorated surfaces. *Nat. Mater.* **2007,** *6* (9), 661-664.

157. Starov, V. M., Zhdanov, S. A., & Velarde, M. G., Spreading of liquid drops over thick porous layers: complete wetting case. *Langmuir* **2002,** *18* (25), 9744-9750.

158. Marmur, A., The radial capillary. *J. Colloid Interface Sci.* **1988,** *124* (1), 301-308.

159. Marmur, A., & Cohen, R. D., Characterization of porous media by the kinetics of liquid penetration: the vertical capillaries model. *J. Colloid Interface Sci.* **1997,** *189* (2), 299-304.

160. Staples, T. L., & Shaffer, D. G., Wicking flow in irregular capillaries. *Colloids and Surfaces A: Physicochemical and Engineering Aspects* **2002,** *204* (1), 239-250.

161. Cassie, A.; Baxter, S., Wettability of porous surfaces. *Transactions of the Faraday society* **1944,** *40*, 546-551.

162. Wischmeier, W. H.; Smith, D. D., Rainfall energy and its relationship to soil loss. *Eos, Transactions American Geophysical Union* **1958,** *39* (2), 285-291.

163. Coulson, S.; Woodward, I.; Badyal, J.; Brewer, S.; Willis, C., Super-repellent composite fluoropolymer surfaces. *The Journal of Physical Chemistry B* **2000,** *104* (37), 8836-8840.

164. Castrejón-Pita, J.; Martin, G.; Hoath, S.; Hutchings, I., A simple large-scale droplet generator for studies of inkjet printing. *Review of Scientific Instruments* **2008,** *79* (7), 075108.

165. Castrejón-Pita, J.; Morrison, N.; Harlen, O.; Martin, G.; Hutchings, I., Experiments and Lagrangian simulations on the formation of droplets in drop-on-demand mode. *Physical Review E* **2011,** *83* (3), 036306.

166. Castrejón-Pita, J. R.; Castrejón-García, R.; Hutchings, I. M., High speed shadowgraphy for the study of liquid drops. In *Fluid Dynamics in Physics, Engineering and Environmental Applications*, Springer: 2013; pp 121-137.

167. Rioboo, R.; Marengo, M.; Tropea, C., Time evolution of liquid drop impact onto solid, dry surfaces. *Experiments in fluids* **2002,** *33* (1), 112-124.

168. Chibowski, E., Surface free energy of a solid from contact angle hysteresis. *Advances in colloid and interface science* **2003,** *103* (2), 149-172.

169. Villermaux, E.; Bossa, B., Single-drop fragmentation determines size distribution of raindrops. *Nature Physics* **2009,** *5* (9), 697-702.

170. Piroird, K.; Clanet, C.; Lorenceau, É.; Quéré, D., Drops impacting inclined fibers. *Journal of colloid and interface science* **2009,** *334* (1), 70-74.